



저작자표시-비영리-변경금지 2.0 대한민국

이용자는 아래의 조건을 따르는 경우에 한하여 자유롭게

- 이 저작물을 복제, 배포, 전송, 전시, 공연 및 방송할 수 있습니다.

다음과 같은 조건을 따라야 합니다:



저작자표시. 귀하는 원저작자를 표시하여야 합니다.



비영리. 귀하는 이 저작물을 영리 목적으로 이용할 수 없습니다.



변경금지. 귀하는 이 저작물을 개작, 변형 또는 가공할 수 없습니다.

- 귀하는, 이 저작물의 재이용이나 배포의 경우, 이 저작물에 적용된 이용허락조건을 명확하게 나타내어야 합니다.
- 저작권자로부터 별도의 허가를 받으면 이러한 조건들은 적용되지 않습니다.

저작권법에 따른 이용자의 권리는 위의 내용에 의하여 영향을 받지 않습니다.

이것은 [이용허락규약\(Legal Code\)](#)을 이해하기 쉽게 요약한 것입니다.

[Disclaimer](#)

공학박사 학위논문

선박용 디젤엔진에서 생성된 수트 입자의 구조 특성
분석과 재생 에너지로의 활용에 관한 연구

Study on Nanostructures of Soot Particles Emitted from
Marine Diesel Engines and Application to Renewable Energy



2016년 12월

한국해양대학교 대학원

기관시스템공학과

이원주

본 논문을 이원주의 공학박사 학위논문으로 인준함.

위원장 윤 석 훈
위원 박 상 균
위원 정 석 호
위원 천 강 우
위원 최 재 혁



2016년 12월 19일

한국해양대학교 대학원

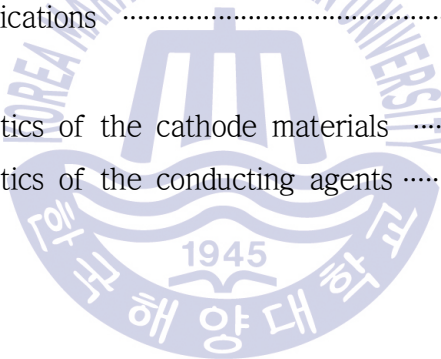
Table of Contents

List of Tables	iii
List of Figures	iv
Abstract	vii
1. Introduction	
1.1 Soot properties and characteristics	7
1.2 Soot nanostructure	14
1.3 Black carbon	19
1.4 Soot formation	22
1.5 Objective of the thesis	25
2. Experimental description	
2.1 Test engines	27
2.2 Fuel oil	32
2.3 Soot preparation	33
2.4 Structure analysis equipment	37
2.5 Manufacture of Li-ion battery	38
3. Characterization of carbonaceous particulate matter :	
Influence of sampling location and engine operation condition	
3.1 Introduction	46
3.2 Soot formation mechanism	49
3.3 Soot nanostructure	52

3.3.1 Influence of sampling location on nanostructure	52
3.3.2 Influence of engine speed on graphitization	56
3.4 Conclusion	61
4. Characterization of carbonaceous particulate matter :	
Influence of engine type and fuel quality	
4.1 Introduction	63
4.2 Soot nanostructure	66
4.3 Image processing techniques	72
4.3.1 Fringe analysis algorithm	72
4.3.2 Structural parameters for fringe analysis	76
4.3.3 Measuring data for fringe analysis	77
4.4 Conclusion	83
5. Application : Li-ion battery	
5.1 Introduction	85
5.2 Fabrication of Li-ion battery	87
5.3 Performance test result	93
5.4 Conclusion	100
6. Summary	
References	105

List of Tables

Table 1-1	MARPOL Annex VI NO _x Emission Limits	2
Table 1-2	MARPOL Annex VI Fuel Sulfur Limits	3
Table 1-3	Summary of primary particle (d_p) of soot	10
Table 2-1	Technical description of the T/S HANBADA	28
Table 2-2	Technical description of the 2-stroke engine	29
Table 2-3	Specifications of gas analyzer (Testo 350-XL)	30
Table 2-4	Technical description of the 4-stroke engine	30
Table 2-5	Fuel specifications	32
Table 5-1	Characteristics of the cathode materials	89
Table 5-2	Characteristics of the conducting agents	92



List of Figures

Chapter 1

Fig. 1-1 Distribution of diesel PM	8
Fig. 1-2 TEM image of diesel soot for 34,000x	9
Fig. 1-3 Schematic of radius of gyration measurement of soot agglomerate	12
Fig. 1-4 Schematic of graphitic carbon nanostructure	15
Fig. 1-5 Schematic of soot formation process	23

Chapter 2

Fig. 2-1 Picture of the 2-stroke diesel engine	29
Fig. 2-2 Picture of the 4-stroke diesel engine	31
Fig. 2-3 Pictures of sampling locations for soot from 2-stroke engine ..	34
Fig. 2-4 Schematics of sampling locations for soot	35
Fig. 2-5 Picture of the soot samples	36
Fig. 2-6 Picture of sampling the soot deposits	36
Fig. 2-7 Raman spectroscopy	37
Fig. 2-8 High resolution transmission electron microscopy (HRTEM)	37
Fig. 2-9 Manufacture of electrode plate and coin cell	39
Fig. 2-10 Doctor blade	40
Fig. 2-11 Vacuum oven	41
Fig. 2-12 Roll press	41
Fig. 2-13 Punched anodes	42
Fig. 2-14 Weighing the anodes	42
Fig. 2-15 Glove box charged with argon gas	43
Fig. 2-16 Assembly of a coin cell in the glove box	44

Fig. 2-17 Crimp machine	45
Fig. 2-18 Assembled coin cells	45

Chapter 3

Fig. 3-1 Conceptual diagrams for soot formation mechanism and molecular structures of carbonaceous materials	51
Fig. 3-2 HRTEM images of carbonaceous agglomerates collected at a) the TC exit and b) the ECO exit	53
Fig. 3-3 Measured exhaust gas temperature at the T/C exit as a function of a cursing engine speed	53
Fig. 3-4 Measured exhaust gas temperature as a function of the sampling location. a) T/C inlet, b) T/C exit, c) ECO exit, d) Funnel	54
Fig. 3-5 HRTEM images of individual spherical particles collected from A) ECO inlet, B) ECO exit, and C) chimney funnel	56
Fig. 3-6 Raman intensity plot for soots sampled at the engine speed of a) 120 rpm and b) 160 rpm	58
Fig. 3-7 Variations in the NO _x and exhaust gas temperature as a function of the engine speed	60

Chapter 4

Fig. 4-1 Raman intensity plot and G/D peak for diesel soot sampled from 2 & 4 stroke engines	67
Fig. 4-2 HRTEM images of diesel soot collected from a) the 2-stroke engine; b) the 4-stroke engine	69
Fig. 4-3 HRTEM images of diesel soot collected from a) the 2-stroke engine; b) the 4-stroke engine at higher magnifications	71
Fig. 4-4 Schematic of fringe reconnection process during post-processing	74

Fig. 4-5 Skeletonized fringe image of HRTEM image of collected soot	75
Fig. 4-6 Schematic of a box enclosing a fringe for tortuosity calculation	77
Fig. 4-7 Histograms of fringe length for soot collected from 2-stroke engine burned Bunker A	79
Fig. 4-8 Histograms of fringe length for soot collected from 4-stroke engine burned Bunker C	80
Fig. 4-9 Histograms of fringe tortuosity for soot collected from 2-stroke engine burned Bunker A	81
Fig. 4-10 Histograms of fringe tortuosity for soot collected from 4-stroke engine burned Bunker C	82

Chapter 5

Fig. 5-1 Current collector	92
Fig. 5-2 Electrical performance test equipment	93
Fig. 5-3 Charge-discharge curves for the cycled cells at different C rates	94
Fig. 5-4 Graphitization furnace	95
Fig. 5-5 Charge-discharge curves for the cycled cells using soot deposits annealed at 600°C	96
Fig. 5-6 Charge-discharge curves for the cycled cells using soot deposits annealed at 900°C	97
Fig. 5-7 Charge-discharge curve for the first cycle of the cell using raw soot deposits	98
Fig. 5-8 Charge-discharge curve for the first cycle of the cell using soot deposits annealed at 600°C	99
Fig. 5-9 Charge-discharge curve for the first cycle of the cell using soot deposits annealed at 900°C	99

<국문 초록>

선박용 디젤엔진에서 생성된 수트 입자의 구조 특성 분석과 재생 에너지로의 활용에 관한 연구

이 원 주

기관시스템공학과
한국해양대학교 대학원

초록

전 세계 무역의 80% 이상이 선박에 의해 이루어지고 있으며, 이로 인해 선박에서 배출되는 유해 배기배출물은 운송 분야 전체에서 발생하는 배기배출물 대비 상당히 큰 비중을 차지하고 있다. 이에 국제해사기구(IMO)에서는 선박으로부터 배출되는 유해 배기배출물(SOx, NOx, CO₂ 등)에 대하여 단계적이고 지속적인 규제를 시행하고 있으나, 지금까지의 규제는 기체상태의 유해물질만을 대상으로 하고 있다.

현재 IMO에서 규제하고 있지는 않지만, 선박의 디젤엔진에서 배출되는 입자상물질(Particulate Matter, PM)은 호흡기를 통해 인체에 유입되어 호흡기 질환을 유발하거나 폐암의 원인이 되기도 하는 등 인체에 매우 유해한 물질로 널리 알려져 있다. 또한, 최근에는 PM이 인체에 유해할 뿐만 아니라 기후변화 등 환경적으로도 그 유해성이 아주 큰 것으로 보고되고 있으며, 특히 PM 가운데서도 블랙카본(Black Carbon, BC)은 극지방의 온난화와 해빙을 촉진시키는 주요 원인물질로서 주목받고 있다. 이에 극지방의 블랙카본에 대한 추가 규제 논의가 국제사회에서 활발하게 진행되고 있다.

이와 같이 강화되는 배기배출물에 대한 국제 규제와 향후 예상되는 새로운 배출 규제에 선제적으로 대응하고, IMO의 정책에 신속하게 대응하기 위해서는 선박에서 배출되는 입자상물질에 대한 연구가 필수적이다.

하지만 실제 운항중인 선박을 대상으로 하는 실선실험은 상당히 제한적이며, 접근의 어려움이 있기 때문에 기존의 디젤엔진에서 배출되는 PM에 대한 연구는 주로 육상의 소형·고속 엔진을 대상으로 진행되어 왔으며, 사용 연료 또한 선박에서 주로 사용하는 잔사유가 아닌 고품질의 증류유를 대상으로 하였다.

본 연구에서는 실제 운항중인 선박에 탑재된 디젤엔진을 대상으로 선박에서 사용하는 다양한 잔사유를 연료로 하여 엔진의 배기가스 내 PM을 채취하였고, 채취한 PM의 특성을 파악하기 위해 다양한 방법의 구조 분석을 시도하였다. PM 내 수트(soot)는 대부분 탄소 성분으로 이루어져 있기 때문에 탄소의 분자 및 나노구조를 분석하는데 적합한 고분해능전자현미경(High Resolution Electron Transmission Microscope, HRTEM), 라만분광법(Raman Spectroscopy) 등의 분석 방법을 주로 이용하여 그 특성을 조사하였다.

본 연구의 첫 번째 실험에서는 한국해양대학교 실습선 한바다호에 승선하여 운항 중 주기관의 회전수와 배기관 내 PM 샘플링 위치에 따른 입자의 특성 변화를 확인하였다. 그 결과 과급기(Turbo Charger, T/C)에서 멀어질수록, 즉 에코노마이저(Economizer)를 통과하여 연돌에 가까워질수록 배기가스 온도 저하에 따른 미세 입자의 응집이 더 많이 일어나는 것을 확인할 수 있었다. 반면, T/C에 가까운 곳(배기가스 온도가 높은 곳)에서 채취한 샘플에서는 연돌 측(배기가스 온도가 낮은 곳) 샘플에 비해 더 graphitic 구조가 관찰되었으며, PM 내 BC의 성분도 더 많은 것으로 확인되었다.

두 번째 실험에서는 엔진의 행정과 사용 연료에 따른 PM의 구조 특성을 조사하기 위하여 선박용 2행정 디젤엔진과 4행정 디젤엔진을 대상으로 선박에서 주로 사용되는 병커 A, C를 연료로 하여 운전 중 배기가스 내 샘플을 채취한 후 분석을 시도하였다. 그 결과 배기가스 온도가 가장 낮게 형성되는 case a(2행정, 병커 A)와 배기가스 온도가 가장 높게 형성되는 case b(4행정, 병커 C)를 비교하였을 때, 수트의 구조가 가장 명확한 대비를 보였다. 배기가스 온도와 연료 내 황성분에 의한 영향으로 case b에서 샘플링한 수트의 초기입자 직경 크기가 case a에 비해 더 작은 것으로 확인되었고, 나노구조도 보다 graphitic 상태를 보였다. 전자현미경을 통해 얻어진 이미지를 이용한 입자의 구조 분석은 육안으로 이루어지기 때문에 그 결과가 정량적이지 못하다는 결점이 있다. 이에 이미지의 분석을 보다 정량적으로 명확히 하고 그 자료의 데이터베이스화를 위해 디지털 이미지 프로세싱 기법을 활용하여 추가 분석을 진행하였고, 나노구조의 주요 특징인 프린지의 길이와 곡률에 대한 분석을 시도하였다. 그 결과 case b의 이미지에서 프린지의 길이가 더 길고, 곡률은 더 적은 것으로 나타났다. 즉, 육안 분석과 동일하게 엔진의 종류와 사용 연료에 의해 배기가스 온도가 높게 형성된 곳에서 채취한 샘플이 더욱 graphitic 구조를 띠는 것으로 확인되었다.

세 번째 연구에서는 앞의 두 연구에서 확인된 바와 같이 디젤엔진 수트가 대부분 탄소로 구성되어 있고 그 입자가 graphitic 나노구조를 가지고 있음에 착안하여, 선박으로부터 버려지는 수트를 재활용하여 재생에너지의 자원으로 이용하는 연구를 시도하였다. 그 일환으로 리튬이온 배터리의 음극 활물질 대체 재료로 적용가능한지 여부에 대한 실험을 진행하기 위해 선박용 주기관의 배기관 내에 퇴적된 수트를 수거 후, CR2032 리튬이온 배터리 시제품을 제작하여 전기적 성능 테스트를 하였다. 그 결과 충·방전 성능이 상용 배터리에는 미치지 못하지만 어느 정도의 성능을 보였으며, 이는 충분히 음극 활물질로의 활용이 가능하다고 판단되었다. 나아가 전기적 충·방전 성능을 개선하기 위하여 채취한 수트를 질소 분위기 하에서 600°C, 900°C로 가열하여 불순물을 제거한 후, 다시 리튬이온 배터리를 제작하여 전기적 성능 테스트를 하였다. 그 결과 열처리를 하지 않은 배터리보다 600°C에서 900°C로 갈수록 배터리의 충·방전 성능이 개선되는 것이 확인되었다.

현재 국내에서 생산되는 리튬이온 배터리의 음극 활물질은 전량 수입에 의존하고 있으며, 주로 중국의 천연자원이나 일본의 가공물질을 수입하여 사용하고 있다. 또한 해운 선사에서는 주기관의 에코노마이저 혹은 소기매니폴드에서 발생하는 다량의 수트성 물질을 폐기하기 위하여 많은 비용을 지불하고 있는 실정이다. 따라서 비용을 들여 처리하는 유해 폐기물을 새로운 재생에너지의 자원으로 활용하는 시도는 아주 유익한 발상의 전환이며, 초고온 열처리 및 산처리 등의 방법으로 수트 내 불순물을 더 많이 제거하고 그 나노구조를 최적화하는 후속 연구들이 더해진다면, 본 연구 결과물의 성능을 극대화시키고 나아가 상용화도 가능할 것으로 보여진다.

KEY WORDS: Black Carbon, 블랙카본; Soot, 수트; Diesel Engine, 디젤엔진; Nanostructure, 나노구조; Li-ion Battery, 리튬이온 배터리

Chapter 1. Introduction

Presently, more than 80% of world trade is transported by ships (Fuglestvedt J. et al., 2009). Therefore emission of exhaust gases and particles from ocean going ships contribute significantly to the total emissions from the transportation sector (Eyring V. et al., 2010; Corbett J.J. et al., 1997; Eyring V. et al., 2005). Almost 70% of ship emissions occur within 400 km of coastlines leading to reduced air quality in coastal areas and harbors. In addition, pollutants originating from ships may be transported several hundred kilometers. In this way, shipping may contribute to air quality problems over land and may counteract national land-based control measures, nonetheless increasing coastal pollution (Eyring V. et al., 2010; Eyring V. et al., 2007; Schlager H., 2004). Since ship exhaust gases contribute to the worldwide pollution of air and sea, ships are facing an increasing number of rules and regulations as well as voluntary appeals from international, national and local legislators (Eyring V. et al., 2010).

Emissions from ships in international trade are regulated by the International Maritime Organization (IMO) under Annex VI of the International Convention for the Prevention of Pollution from Ships (MARPOL) 73/78 (IMO, 1998). The IMO regulates to reduce emissions from ships such as nitrogen oxide (NO_x) (IMO, 1997), sulfuric oxide (SO_x) (IMO, 2010a), carbon dioxide (CO₂), volatile organic compound (VOC) and has initiated a process to derive a regulation standard for PM emissions, recently. (Choi J.H., et al., 2016)

In case of NO_x, the IMO emission standards are commonly referred to as Tier I-III standards. The Tier I standards were defined in the 1997 version of Annex VI, while the Tier II/III standards were introduced by Annex VI amendments adopted in 2008. The Tier III controls apply only to the specified ships while operating in Emission Control Areas (ECA) established to limit NO_x

emissions, outside such areas the Tier II controls apply. A marine diesel engine that is installed on a ship constructed on or after 1 January 2016 and operating in the North American ECA and the United States Caribbean Sea ECA shall comply with the Tier III NO_x standards. NO_x emission limits are set for diesel engines depending on the engine maximum operating speed (n, rpm), as shown in **Table 1-1**.

Table 1-1 MARPOL Annex VI NO_x emission limits

Tier	Ship construction date on or after	Total weighted cycle emission limit (g/kWh) n = engine's rated speed (rpm)		
		n < 130	n = 130 - 1999	n ≥ 2000
I	1 January 2000	17.0	$45 \cdot n^{(-0.2)}$	9.7
II	1 January 2011	14.4	$44 \cdot n^{(-0.23)}$	7.7
III	1 January 2016	3.4	$9 \cdot n^{(-0.2)}$	2.0

Annex VI regulations include limits on sulfur content of fuel oil as a measurement to control SO_x emissions. At the initial stage of regulation, sulfur content of fuel oil was limited to 4.5% m/m. The currently existing most stringent IMO regulation limits the sulfur content 0.1% m/m from the beginning of 2015. These fuel oil sulphur limits are subject to a series of step changes over the years. Special fuel quality provisions exist for SO_x Emission Control Areas (SO_x ECA or SECA). The sulfur limits and implementation dates are listed in **Table 1-2**.

Table 1-2 MARPOL Annex VI fuel sulfur limits

Date	Sulfur limit in fuel (% m/m)	
	SOx ECA	Global
2000	1.5	4.5
2010.07	1.0	
2012.01		0.1
2015.01	0.5	
2020 ^s		
a - alternative date is 2025, to be decided by a review in 2018		

In addition, the IMO has also commissioned studies in the impacts of greenhouse gases from ships (IMO, 2009) and subsequently introduced carbon dioxide reduction measures in the form of a ship energy efficiency design index (EEDI) requiring continual improvements in ship efficiency. An energy efficiency design index (EEDI) has been adopted by the IMO (IMO, 2011a) and requires stepwise improvements to the energy efficiency of new build ships, starting at 10% reduction in CO₂ per tone-mile from 2015, increasing to 20% and 30% from 2020 and 2025, respectively.

Ships are significant sources of combustion-generated pollutants such as carbon monoxide (CO), sulfur oxides (SOx) and nitrogen oxides (NOx) and particulate matter (PM) emissions in many areas of the world (Corbett & Fischbeck, 1997). The high levels of SOx emissions from slow-speed marine diesel engines are primarily associated with high levels of sulfur in the heavy fuel oil (HFO), used in these engines. The fuel sulfur, during combustion, is oxidized into different oxides of sulfur, mainly SO₂ and SO₃, typically in ratio of 15:1. NOx are formed when fuel nitrogen and nitrogen in air react with oxygen at high temperatures in the burning fuel spray (MAN B&W, 2004;

Harshit A. et al., 2008). Particulate matters in the exhaust originate from a number of sources like agglomeration of very small particles of partly burned fuel, partly burned lubricating oil, ash content of fuel oil and cylinder lubricating oil, sulfates and water (Heywood, 1988; Harshit A. et al., 2008). There are many environmental issues that are associated with these pollutants. For example, SO₂ emitted into air is oxidized, producing SO₃ and it then reacts with water (either moisture in the air or in contact with rain water), resulting in acid rain:



It is well known that acid rain causes acidification of lakes and streams (with attendant diseases in fish and wildlife), corrosion of building materials, and damages to forest and soils, and water tables.

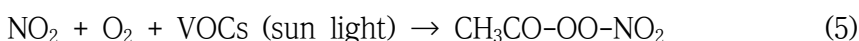
NO_x formed from combustion process can cause photochemical smog by reacting to sunlight (Ying et al., 2007). When NO₂ reacts with sunlight, an oxygen atom (O) splits from the NO₂ molecule through a photochemical reaction:



O atoms formed in Eqn. (3) can react with oxygen molecules (O₂) in the air to form ozone (O₃):



O_3 is known to cause breathing difficulties, headaches, fatigue and respiratory problems (Rubio et al., 2004). NO_2 , O_2 and VOCs react in the presence of sunlight to produce peroxyacetylnitrate ($\text{CH}_3\text{CO}-\text{OO}-\text{NO}_2$, also known as PAN):



The PAN ($\text{CH}_3\text{CO}-\text{OO}-\text{NO}_2$) in photochemical smog can significantly alter vision through irritation of the eye.

Most of combustion by-products also present harmful impacts to the human body. For example, the presence of CO in the blood stream prevents the hemoglobin from carrying O_2 from the lungs to the cells, which causes dizziness, headaches and visual aberrations (Mochizuki & Forster, 1962) and leads to fatality. Also, it is reported that exposure to high concentration of SO_2 can cause breathing difficulties and obstructs airways, especially for individuals with lung disease as well as emphysema. Compared to CO and SO_2 , the direct health implication of NO_x is not serious in itself, however, NO_x contributes to the formation of photochemical smog.

Combustion processes have also been recognized as one of major sources of small ($2.5 \mu\text{m} \sim 10 \mu\text{m}$) carbonaceous particles that have tremendous impacts to environmental and health considerations. Carbonaceous particles (such as soot and smoke) emitted to environment are transported great distances through the prevailing air currents. During the transport, the particles absorb solar radiation and radiation from earth, then re-radiates

back to the earth, contributing to the overall global warming (Jacobson, 2001). Also, numerous epidemiological studies have revealed that combustion-related carbonaceous particle matters have a negative impact on human health such as heart attacks, strokes, cardiovascular diseases (Peters et al., 2001), lung cancer (Pope et al., 2002).



1.1 Soot properties and characteristics

The IMO has moved to address the health and climate impact of the emissions from the combustion of low-quality residual fuels within the commercial shipping industry. Residual fuels, the fraction of crude oil remaining after the refining process, can contain high levels of sulfur, heavy metals (e.g. vanadium, nickel), ash (non-combustible inorganic material) and high molecular weight aromatic hydrocarbons (Lack & Corbett, 2012). Each of these impurities (except perhaps for heavy metals) is known to create slower and delayed combustion, potentially leading to soot formation (ABS, 2001). The term ‘soot’ is commonly used for black, mostly solid carbonaceous particulate matter created through incomplete combustion of carbon-based fuels (CIMAC, 2012; Bond, T. et al., 2004). Ships emit more soot per unit of fuel consumed than other fossil fuel combustion sources due to the quality of fuel used (Lack & Corbett, 2012).

Some previous studies suggest that, at similar mass concentrations, nanometer sized particles are more toxic than micron sized particles (Pöschl U, 2003; Kittelson, 1998). While most of the mass of diesel soot particles arises from the fine particles with diameters of 0.1–1 μm , the largest number of particles is in the nanometer size range, 10–100 nm in diameter as shown in **Fig. 1-1**. Concerns have also been raised for particles in this ultrafine size range because particles of such size can be toxic even when larger particles of the same material are non-toxic (Braun et al., 2005).

The burning of hydrocarbon fuels can lead to the production of carbonaceous materials, commonly referred to as soot. Soot particles possess carbon, hydrogen and trace elements that form both amorphous and graphitic structures (Palmer & Cullis, 1965). The soot formation process and the mechanisms for the variations in the physical, chemical, and fractal properties

are very complex. Many investigations have attempted to describe the soot formation process using semiempirical (Moss et al., 1988; Syed et al., 1990) and detailed chemical kinetic mechanisms (Frenklach and Wang, 1991) as described in the review by Kennedy (1997).

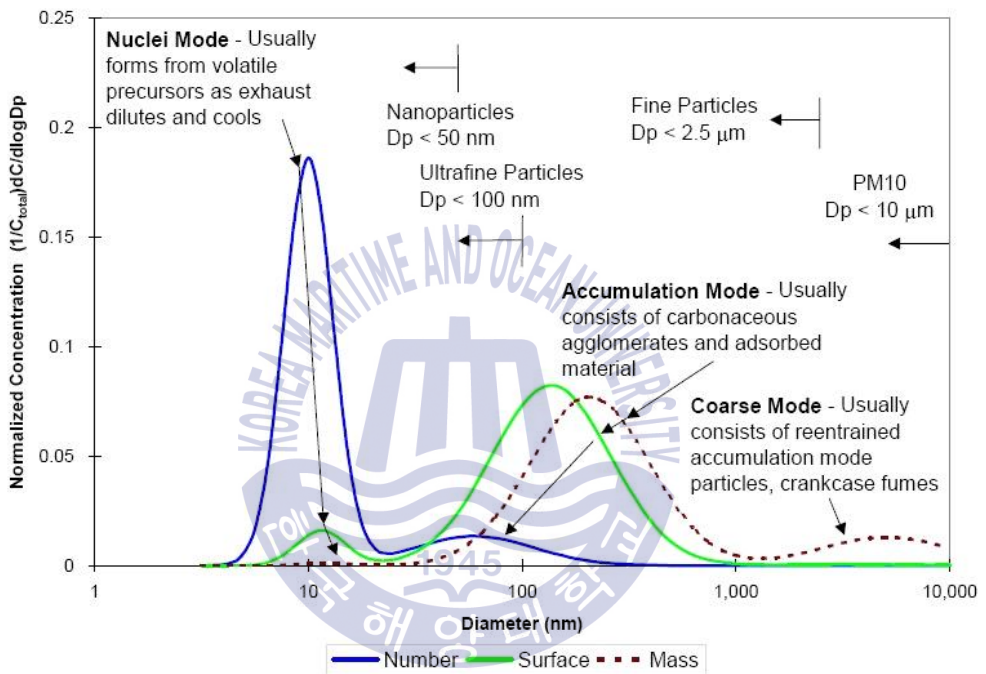


Fig. 1-1 Distribution of diesel PM

Fig. 1-2 displays a transmission electron micrograph (TEM) of a diesel soot agglomerate obtained at a magnification of 34,000x. The figure clearly delineates the distinct circular primary particles that form the agglomerates. Experimental measurements of the soot primary particle from TEM (or scanning electron micrograph, SEM) typically display a monodisperse size distribution with narrow standard deviations about the average values (Zhu, 2002).

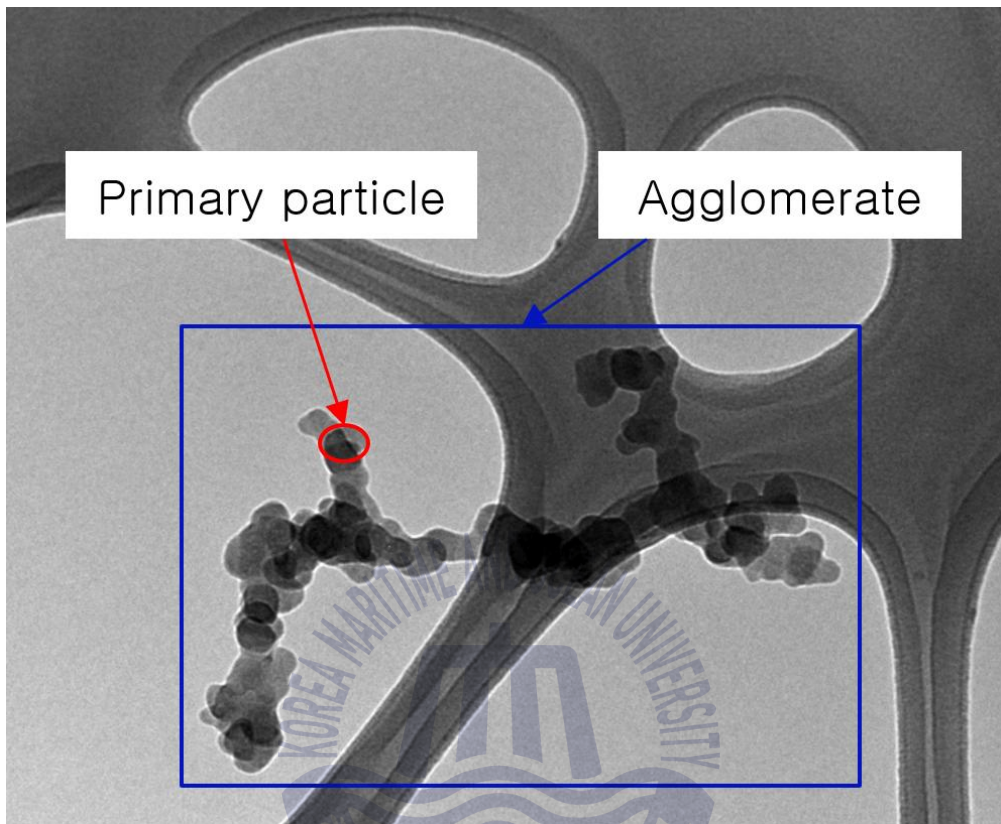


Fig. 1-2 TEM image of diesel soot for 34,000x

The average values of primary particle diameters have been measured previously for a variety of fuels burned under a range of combustion conditions involving premixed flames (Zhu et al., 2000) and diffusion flames (Mulholland & Choi, 1998; Zhu et al., 2002; Williams et al., 2007). The dimensions of the primary particle for soot varies with different fuel types (H/C ratio), different soot sample positions (height above the burner representing differences in the time-temperature history experienced by the soot particles), and different combustion conditions of premixed, diffusion, laminar, and turbulent flames (Dalzell & Sarofim, 1969; Dobbins & Megaridis, 1987; Charalampopoulos & Chang, 1991; Koylu & Faeth, 1992; Zhu et al.,

2000; Koylu et al., 1995; Jensen et al., 2007). **Table 1-3** displays the measured values of the primary particles and the conditions of measurements from previous investigations.

Table 1-3 Summary of primary particle (d_p) of soot

Investigation	d_p (nm)	Flame conditions	Type of fuel
Dalzell and Sarofim, 1969	5 - 80	Laminar diffusion flames	Propane (C_3H_8)
Dobbins and Megaridis, 1987	10 - 40	Coannular diffusion flame	Ethene (C_2H_4)
Charalampopoulos and Chang, 1991	8 - 29	Premixed flames	Propane (C_3H_8)
Koylu and Faeth, 1992; Koylu et al., 1995	47	Turbulent diffusion flames	Acetylene (C_2H_2)
	50		Benzene (C_6H_6)
	32		Ethylene (C_2H_4)
	30		Propane (C_3H_8)
	41		Propylene (C_3H_6)
Zhu et al., 2000; Zhu et al., 2002	37	Laminar diffusion flames	Ethylene (C_2H_4)
	51		Acetylene (C_2H_2)
Jensen et al., 2007	57 - 74	Pool fires	JP-8
William et al., 2007	41	Coannular diffusion flames	Kerosene
	36		Ethene (C_2H_4)
	20		Methane (CH_4)

As displayed in **Fig. 1-2**, soot agglomerates are composed of individual soot primary particles that are arranged to form mass fractal objects (Koylu & Faeth, 1992; Koylu et al., 1995). Soot agglomerates collected from flames can contain from a few primary particles to 1000' s of primary particles. The size of agglomerate is also commonly measured through image processing analysis of TEM or SEM images.

The soot agglomerate dimensions are commonly quantified using the definition of the radius of gyration, R_g . The radius of gyration of agglomerate is defined as:

$$R_g = \sqrt{\frac{1}{N_p} \sum_{i=1}^{N_p} r_i^2} \quad (6)$$

where r_i is the distance between the center of an individual primary particle and the centroid of the associated aggregate, and N_p is the number of primary particles comprising the agglomerate. A graphical description of the soot agglomerate, r_i and R_g is displayed in **Fig. 1-3**.

The radius of gyration is an important parameter of soot that provides insights regarding the agglomeration process and the number of particles comprising the agglomerate. The R_g measurements of soot also vary widely depending on the fuel type (initial H/C ratio), different sampling location of the soot (defined by height above the burner surface which also denotes variation in the residence time) and different burning conditions (Koylu & Faeth, 1992; Koylu et al., 1995; Charalampopoulos & Chang, 1991).

Soot agglomerates form mass fractal objects that are defined by the primary particle dimension, agglomerate dimension, and fractal dimensions. Using fractal geometry analysis, the number of primary particles comprising the agglomerate, N_p , the radius of gyration, and fractal dimensions are related by

the following equation (Koylu et al., 1995):

$$N_p = K_f \left(\frac{R_g}{d_p} \right)^{D_f} \quad (7)$$

where, K_f is the prefactor term, D_f is the fractal dimension, R_g is the radius of gyration, and d_p is the primary particle diameter.

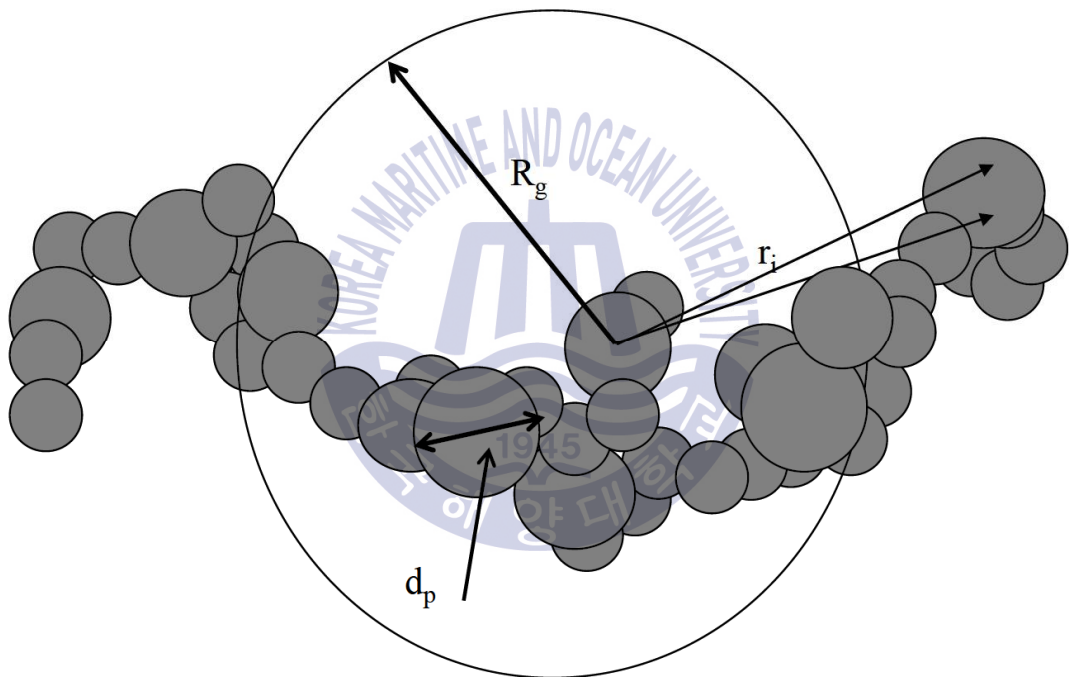


Fig. 1-3 Schematic of radius of gyration measurement of soot agglomerate

The structure of the soot agglomerate can be divided into two broader categories of particle-cluster agglomeration in which individual particles collide with existing agglomerates. In the cluster-cluster agglomeration mechanism, the reactions do not involve individual particles but rather existing agglomerates colliding to form larger clusters. For both the particle-cluster

and cluster-cluster mechanisms, the shape and structure of the agglomerates are determined by the fractal dimension and the regime in which the agglomeration that occurs. For all cases, higher values of fractal dimension produce more compact structure as opposed to the wispy, chain-like structure observed at the lower values of the fractal dimension.

Furthermore, the particle-cluster agglomeration produces structures that are more compact since the individual particles (which have smaller cross-sectional areas and sizes compared to clusters of primary particles) can be transported towards the center of the cluster without sticking to the outer edges of the cluster.



1.2 Soot nanostructure

It is well known that carbonaceous materials such as graphite, soot, coal, coke and char possess similar structural characteristics in terms of the prevalence of carbon in its molecular composition.

The soot reactivity is directly related to its structure and composition. Properties such as surface area, particle size and crystallinity affect the reactivity of the soot particles. The soot nanostructure depends upon its formation conditions, like fuel identity, residence time and temperature. An understanding of these dependences is fundamental to control the physical properties of the soot and therefore, its chemical reactivity (Vander & Tomasek, 2004; Grieco et al., 2000).

In laboratory studies using a high-temperature furnace, the combustion of different fuels has produced considerably different soot nanostructures (Wornat et al., 1995). These differences in soot nanostructure were shown to be mainly dependent upon the fuel composition, the combustion process, and the combustion temperature (Vander & Tomasek, 2004).

The details of soot structure at the nanolevel are normally gleaned from images recorded using a high-resolution transmission electron microscope (HRTEM), a high-magnification instrument with spatial resolution better than 0.2 nm. Sample examinations by HRTEM can furnish information on atom arrangements, surface topography and texture, particle morphology, material crystallinity, and composition.

Within carbonaceous materials, each carbon atom is tightly bonded to three neighbors and is hexagonally arranged within a basal plane (a-b direction) forming a single graphene layer as shown in **Fig. 1-4**. The size of each graphene layer is equal to that of the carbon lamella (which will be also

referred to as fringes in this study). The graphitic structure in carbonaceous materials typically known as “turbostratic structure” represents the group of graphene layer stacked with respect to each other along the c-axis. Graphite consists of planar graphene layers with a stacking length (i.e., interlayer space) of 0.35 nm along the c-axis.

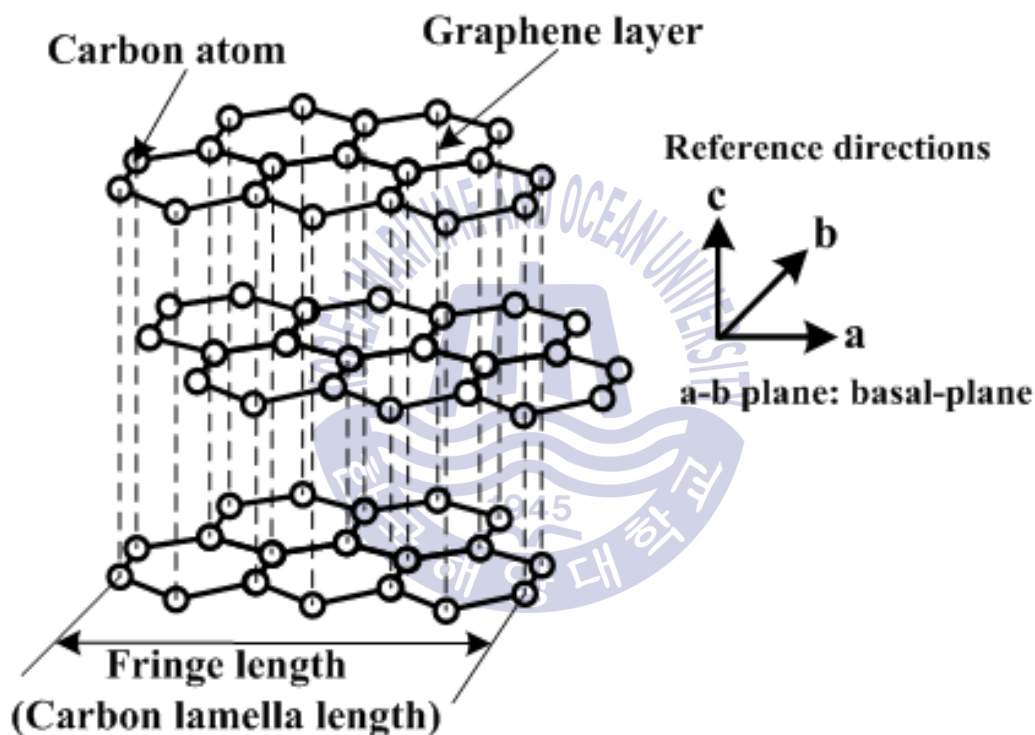


Fig. 1-4 Schematic of graphitic carbon nanostructure

For flame-generated particulates, namely soot, the characteristics of the carbon lamellas have been referred to as the soot nanostructure due to its properties that are observed in the nanoscale. Categorization of the physical dimensions of the soot will include the measurement of the mean value of the diameter of the primary particles that constitute the soot aggregate with

sizes up to several hundred nanometres, built up from primary particles with sizes of 5–50 nm, approximately (Barone et al., 2003; Wenzel et al., 2003). Particle size is one important structural parameter of soot that is often assessed with microscopy or scattering techniques.

The soot particles appear to be encapsulated aggregates of highly defective carbon “onions”, presenting a graphitic structure. These onion-like structures are made from parallel graphene sheets arranged with their basal planes perpendicular to the radii of the structures. Several researchers (Ishiguro et al., 1997; Stasio, 2001) even distinguish clearly two parts: an inner core, composed of several fine particles of 3–4 nm in diameter, and an outer shell, composed of microcrystallites with periodic orientation of carbon sheets, or a so-called graphitic structure.

In order to analyse the physical properties of the soot and relate them further to its reactivity, different techniques have been widely used, mainly scattering and microscopic techniques.

Raman spectroscopy, diffraction techniques, and high resolution transmission electron microscopy (HRTEM) are current techniques used to investigate the soot nanostructure and morphology (Shaddix et al., 2005; Braun et al., 2004). Raman spectroscopy is an appropriate tool for the investigation of carbon compounds, since their Raman spectra have been found to respond to changes in the microscopic structure of the carbon materials (Sadezky et al., 2005; Chen et al., 2006). An analysis of the spectra allows the inference of internal physical characteristics of the samples such as the degree of the structural disorder (Escribano et al., 2001).

Raman spectroscopy provides qualitative information regarding the amorphous versus graphitic content of carbon based on the spectral variation of the scattering intensity from the sample. For carbon-based material, there

are two prominent scattering peaks, defined by the D peak and G peak. The G peak (1580 ~ 1600 cm⁻¹) is related to the carbon-carbon stretching vibrations while the D peak (1350 cm⁻¹) is attributed to the poly-aromatic ring vibrations (Popovitcheva et al., 2000). As the graphite becomes disordered within the carbon layers, the G peak broadens. When the level of disorder further increases, a new peak called the D peak arises. The analysis of the peak intensity ratio, I_D/I_G , also enables the prediction of the graphene layer dimension of the nanostructure using the following empirical correlation:

$$\frac{I_D}{I_G} = C \frac{1}{L_a} \quad (8)$$

where I_D is the intensity of D peak, I_G is the intensity of G peak, C is an empirical constant that is approximately 4.4 nm, and L_a is the in-plane carbon layer dimension. While the graphene layer dimension from Raman spectroscopy provides useful information, there is other soot nanostructure information that is required for a comprehensive analysis. Important carbon nanostructure properties such as overall degree of graphitization and mean carbon lamella length cannot be analyzed using Raman Spectroscopy.

There are other techniques based on diffraction analysis such as X-ray diffraction (XRD) and electron beam diffraction (ED) that have been used as effective instruments for measuring carbon lamella structures. Even though diffraction methods provide reliable information for characterization of the carbon nanostructure, particularly the distance between stacked carbon lamellas, their uses are still limited. For example, ED is sensitive to variations in the crystal structure such as small degrees of short range ordering in the carbon material. Therefore, ED availability is limited to the examination of

localized sample analysis. In contrast, XRD provides an overall measure of carbon nanostructure. X-ray diffraction is a non-destructive and well-established technique with good reproducibility. X-ray scattering techniques have been widely used for the study of size and structure of molecules and clusters (Zhu et al., 2004; Ossler & Larsson, 2004).

The nanostructure and growth processes of soot particles in a diesel engine can be explained as follows on the basis of the TEM results. Several layers made up of network structures of carbon atoms are piled up concentrically in a turbostratic state. These carbon networks seem to have a bending nanostructure namely, curvature of the carbon lamella, that cannot be measured using either Raman spectroscopy or conventional diffraction methods. Curvature of carbon lamella is a very important characteristic of carbon nanostructure that can distinguish the presence of five-member carbon rings on the basal plane as opposed to the more conventional six-member rings. These curvatures can be clearly identified from HRTEM images of carbonaceous materials. In addition to the curvature, other quantities such as carbon lamella length and orientation can also be measured from the HRTEM images. For these reasons, the analysis of HRTEM images has become a preferred method for characterizing the nanostructure for carbonaceous materials for it enables the measurement of the fringe spacing, lamella curvature, length, and orientation.

It is generally accepted that the curvature of the carbon lamella (thus, the presence of five-member carbon rings) is higher for amorphous carbon compared to graphitic carbon. The primary reason for the higher curvature for amorphous carbon is related to the introduction of sp^3 hybridization to sp^2 carbon framework. In a previous study by Vander Wal and Tomasek (2004), it was reported that the carbon lamella curvature and length can be correlated with changes in the temperature and time history.

1.3 Black carbon

The climate of the Arctic region is known to be warming at almost twice the rate of the rest of the world (IPCC, 2007; ACIA, 2004). The mechanisms of this warming, and in consequence Arctic sea ice and snow loss, are closely linked to surface air temperatures, ocean circulation and radiative fluxes (Serreze et al., 2007). The majority of influence on the radiative forcing in the Arctic is from external emissions of greenhouse gases and particulate matter (Shindell & Faluvegi, 2009; ACIA, 2004) with possibly half of Arctic temperature rise linked to BC. The Arctic environment is particularly sensitive to BC both in the atmosphere and when deposited on snow and ice (Quinn et al., 2008). Investigation by NASA using satellite data and computer simulations demonstrate that increases in the melting of snow and ice at the Arctic are attributed to BC deposited on snow and ice surface BC deposited on snow and ice surfaces darkens the normally highly-reflective surfaces, thereby lowering the albedo (which is defined as the ratio of reflected to incident radiation intensities). As a result, the snow and ice surface absorb more heat compared to the uncoated reflective surface, leading to increased temperatures and a higher rate of melting. For example, an albedo change of 1.5% at the Arctic can produce a thinning of the ice layer by approximately one meter (Hansen & Nazarenko, 2004).

BC dispersed into the atmosphere absorbs solar irradiation which increases the temperature of the soot aerosol and re-emits radiation towards the earth, resulting in the heating of the earth's surface. These results also suggest that the influence of soot particles on climate is strongly dependant upon their optical properties such as absorptive and scattering properties.

Recent work shows that also ship BC emissions from outside of the Arctic can contribute to Arctic warming (IMO, 2010b). As sea ice extent declines the

possibility of more Arctic shipping traffic increases as resource exploration/extraction and full Arctic ship transits become possible. Ships, therefore, may represent an increasing local source of Arctic pollution (Corbett et al., 2010). In addition to emissions from local ship traffic, BC emissions from ships as far South as 40° N may impact the Arctic climate (IMO, 2010b). In addition to the climate impacts, BC (as an aerosol emission) contributes to adverse health effects, premature mortality and visibility reduction (Park et al., 2003; Corbett et al., 2007)

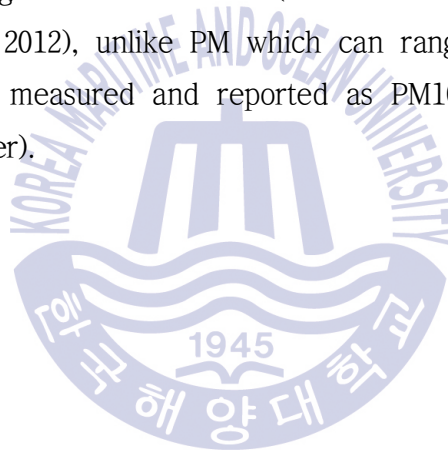
Only a small fraction of the carbon in a fuel is transformed to black carbon, with the remainder being emitted as CO₂ or a variety of other products of incomplete combustion. Black carbon remains in the atmosphere for about a week (Ogren et al., 1984; Parungo et al., 1994; Muller, 1984), while CO₂ lingers for several decades. However, because BC is such a potent warmer, the immediate warming impacts are much greater than those of CO₂. And it absorbs incoming and snow-reflected radiation (Law & Stohl, 2007) and accelerates snow and ice melting when deposited to those surfaces (Flanner et al., 2007).

With increasing understanding of the climatic importance of BC, particularly in the Arctic (McConnell et al., 2007), and the potential for an increase of direct emissions of BC into the Arctic (Granier et al., 2006; Stroeve et al., 2007) it is essential to better understand BC emissions from shipping. Discussions have started up at IMO about the need and potential for restricting BC emission in the Arctic region caused by international shipping. In recent years efforts to investigate the definition, measurement and impact of BC emissions from shipping have been initiated by the IMO (IMO, 2011b).

Since soot is comprised of mostly carbon, it is generally accepted as carbonaceous Particulate matter (PM) in combustion research communities. And soot is normally divided into two primary components 'elemental' or

‘black’ carbon (EC or BC) and ‘organic’ carbon (OC), which are defined using thermal and optical standard procedures (Lloyd & Cackette, 2001; Chow et al., 2001). However, despite extensive research, there is considerable uncertainty over the molecular structure and microstructure of the OC and EC components of most forms of soot (Fung et al., 2002; Lighty et al., 2000).

BC is a component of PM mass, the contribution of which is dependent on the combustion source. For example, BC from biomass burning comprises 2 ~ 5% of total PM mass where BC from engines burning ultra-low sulphur diesel can range from 65% ~ 75% of PM mass (Burtscher, 2005). BC is also formed within a diameter range of 20 ~ 250nm (Schwarz et al., 2008; Kondo et al., 2011; Sedlacek et al., 2012), unlike PM which can range up to many 1000’s of nm and commonly measured and reported as PM₁₀ (<10 μm diameter) or PM_{2.5} (<2.5 μm diameter).



1.4 Soot formation

A detailed analysis of the nanostructure of soot particles must be preceded by an examination of soot formation processes that lead to the different structural properties. The essential chemical mechanism and underlying physics of soot formation are still elusive and many questions persist with regard to the details of soot formation, growth, and oxidation. The various stages of the soot formation process are thought to be system dependent. The conditions under which soot is formed vary widely and depend upon several factors, including pressure, temperature, fuel type, combustor geometry, and extent of premixing (Arana et al., 2004). Soot formation process includes complex chemical and physical pathways that are still not fully understood. Although several theories (Haynes & Wagner, 1981) have been proposed to explain this process, the dominant theory at present supported by numerous experimental and numerical studies is that soot particles are formed via polycyclic aromatic hydrocarbons (PAH). **Fig. 1-5** displays the reaction pathway leading to soot formation sequentially through (1) formation of aromatic rings and their growth (2) soot particle inception, (3) soot surface growth by growth species such as C_2H_2 (4) coalescent coagulation to form larger particles, and finally (5) agglomeration of the primary particles to form chain-like aggregates (Bockhorn, 1994). Regardless of the type of flames and the initial fuels involved, the hydrocarbon fuel undergoes either pure or oxidative pyrolysis that produces a large amount of pyrolysis products such as small hydrocarbon radicals and aliphatics, such as CH_4 and C_2H_2 . This leads to the first critical step for the soot formation process: the formation of aromatic ring from such aliphatics. The first aromatic ring can be formed as a result of C_2H_2 attack on the $n-C_4H_3$ radical or the $n-C_4H_5$ radical (Frenklach & Wang, 1991)



Reaction (9) represents the pathway for the higher temperature reaction while reaction (10) plays the role for the lower temperature reaction. Benzene can be converted to a phenyl radical by H-abstraction or vice versa.

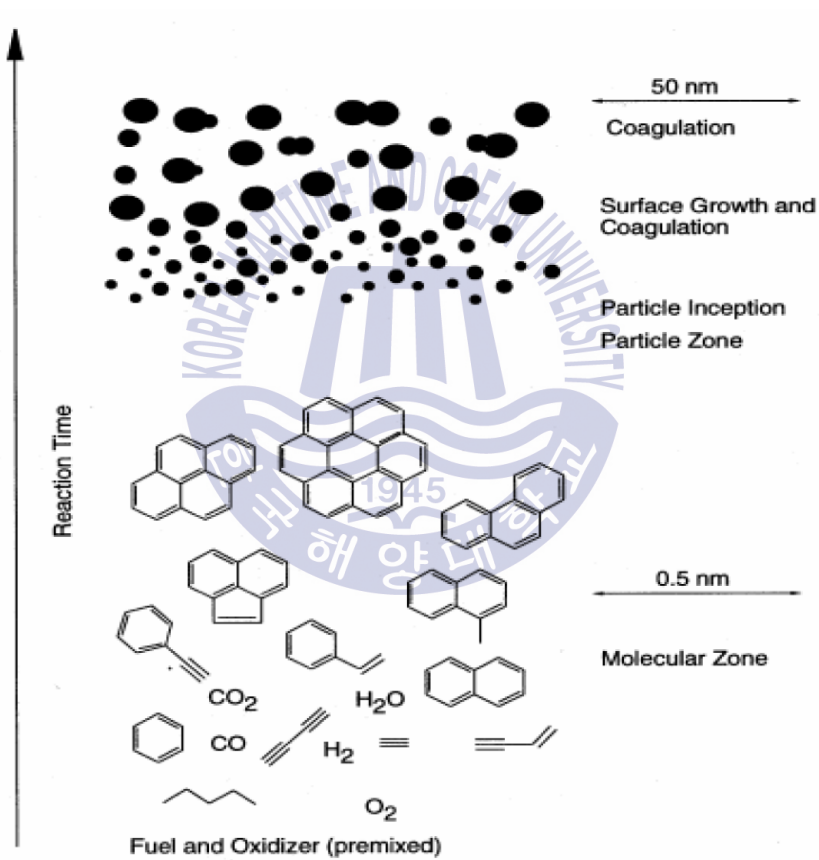


Fig. 1-5 Schematic of soot formation process (Bockhorn,1994)

The growth of aromatics (which will lead to larger PAHs) can occur through a H-abstraction-C₂H₂-addition, known as HACA, and polymerization process

(Frenklach, 2002). The HACA concept was first introduced by Frenklach and Wang (1991).

Compared to the mass of the soot particles achieved during the soot inception period, a significant mass growth of soot particles is obtained through the surface growth process followed by soot inception (Prado et al., 1981). The HACA reaction sequence can be extended to describe the surface growth process. The soot surface growth is assumed to be due to chemical reactions through the HACA mechanism that take place on the surface of soot particles (Frenklach, 2002). On the surface of soot particles covered with C-H bonds, the abstraction of H atoms activates the surface sites, forming surface radicals. Therefore, the active surfaces react more with incoming gaseous hydrocarbon species and thus the surface growth process propagates.

Soot inception and surface growth stages have a great importance in interpreting the nanostructure of soot since it represents the greatest mass growth of particles takes place at these stages. For example, if low temperature-enabled pyrolysis reaction has been dominated at these stages, the reaction pathway for PAH growth would be preferred because the fragmentation of chemical bonds is inhibited (Frenklach, 2002; Vander Wal & Tomasek, 2004). This will result in large PAHs as a result of collision with different gaseous species, forming the amorphous nanostructures in the inner core of soot particles. In contrast, high temperature reactions follow an alternative pathway in which PAH decomposes into smaller species such as C_2H_2 at these stages (Frenklach, 2002; Vander Wal & Tomasek, 2004). Furthermore, higher temperatures will activate more surface sites due to removal of activation energy barriers, enabling more HACA reactions (which eventually result in the carbon mass growth at the surface site). This will lead to prevalence of more graphitic nanostructures at the inner core of soot particles.

1.5 Objectives of the thesis

It is well known that particulate matters emitted from a marine diesel engine contribute significantly to emissions from the transportation sector. To effectively respond to the upcoming environmental regulation by IMO, a series of experimental campaigns to characterize carbonaceous PMs from the ship have been carried out. The present work is anticipated to provide a useful set of information for characterizing carbonaceous PMs emitted from marine diesel engine, because studies on particle emissions collected from ships are quite rare.

Soot was sampled in the training ship T/S HANBADA at various engine conditions (different rpm & sampling location). The nanostructure of the soot was examined using high resolution transmission electron microscopy and Raman spectroscopy to investigate the influence of the engine speed and sampling location on soot characteristics. These experiment results obtained from the analysis are described in Chapter 3.

Experiments were also performed using different diesel engines (2 & 4 stroke) and burning different fuels (Bunker A ~ C) to measure optical properties of the soot. Similarly, the analysis of the physical, fractal and nanostructure properties of diesel soot were performed using Raman spectroscopy, high resolution transmission electron microscopy and a custom software that was developed to analyze the fringe patterns, the tortuosity and the fringe lengths. These properties have provided important assessment of the degree of graphitization of the soot for fuel dependence and engine type. These experiments and analyses are described in Chapter 4.

Most of the soot generated from marine diesel engine are emitted to the atmosphere or thrown away. For that reason, the possibility of utilizing the soot for industrial application as a point of recycling was investigated, which

resulting it as an available material for Li-ion batteries. In addition, Li-ion batteries were manufactured using the soot deposits collected from a diesel engine and their electrical characteristic and performance were analyzed. These experimental results are described in Chapter 5.

This study reveals that the first accurate analysis of nanostructure characteristics of diesel soot emitted from 2-stroke and 4-stroke marine diesel engines fueled with various residual fuels. Also, the result presents the possibility of utilizing the soot for an active material of renewable energy such as a Li-ion battery.



Chapter 2. Experimental description

2.1 Test engines

For the soot sampling, a series of experimental campaigns were performed on-board the training vessel T/S HANBADA, operated by the Korea Maritime and Ocean University. The technical description for the vessel is summarized in **Table 2-1**. The T/S HANBADA is the largest training ship in Asia and she has a 2-stroke marine diesel engine: MAN Diesel & Turbo (MDT) 6L42MC/ME. The specification for the engine is summarized in **Table 2-2**. This engine system has the PMI system and Cocos system which are able to monitor and diagnose the engine conditions and performance automatically. The concentration of the NO_x, CO, and CO₂ in the engine exhaust gas is measured using gas analyzer manufactured by Testo. The specification for the gas analyzer is summarized in **Table 2-3**.

The soot sample of the 4-stroke diesel engine was collected from the engine test facility equipped with MDT 4-stroke marine diesel engine. The specification for the engine is summarized in **Table 2-4**. The engine load was controlled using a dynamometer. And the MIP 3000 indicator, a combustion pressure measurement system, was installed on the engine cylinder to analyze the engine performance and the combustion characteristics.

Table 2-1 Technical description of the T/S HANBADA

Items	Description
Builder	STX Shipbuilding Co., Ltd.
Length Overall	117.02 m
Breath	17.80 m
Maximum Speed	19.0 knots
Service Speed	17.5 knots
Engine Model	MAN B&W 6L42MC/ME
MCR	8,130 BHP × 176 RPM
NCR	6,910.5 BHP × 166.7 RPM
Gross Tonnage	6,686 ton
Image	

Table 2-2 Technical description of the 2-stroke engine

Equipment	Items	Specification
2-stroke diesel engine	Manufacturer	MAN Diesel & Turbo
	Model	6L42MC/ME
	MCR	5979 kW x 176 rpm
	Bore x Stroke	420 x 1360



Fig. 2-1 Picture of the 2-stroke diesel engine

Table 2-3 Specifications of gas analyzer (Testo 350-XL)

Parameter	Measuring range
CO	0 ~ 3000 ppm
NO	0 ~ 3000 ppm
NO ₂	0 ~ 500 ppm
CO ₂	0 ~ 40 Vol. %

Table 2-4 Technical description of the 4-stroke engine

Equipment	Items	Specification
4-stroke diesel engine	Manufacturer	MAN diesel & turbo
	Model	1945 5L23/30H
	MCR	650 kW x 720 rpm
	Bore x Stroke	225 x 300



Fig. 2-2 Picture of the 4-stroke diesel engine



2.2 Fuel oil

Three different types of fuel were used in this study: Bunker A, B and C. Details on fuel used are summarized in **Table 2-5**.

Table 2-5 Fuel specifications

Parameters	Unit	Bunker A	Bunker B	Bunker C
Specific gravity @15/4°C	-	0.8862	0.9382	0.9895
Viscosity Kin. @50°C	mm ² /s	4.288	25.86	357.4
Flash point	°C	73.0	81.0	85.5
Sulfur content	Weight %	0.24	1.76	3.2
Water sediment	Volume %	0.1	0.3	0.1

2.3 Soot preparation

Since there was no power transmission in the marine propulsion diesel engine installed on this vessel, the engine control was achieved solely by increasing or decreasing the engine speed measured by revolutions per minute (RPM). During all voyages, the 2-stroke engine burned Bunker A and B, and cruising engine speed changed from 120 rpm to 160 rpm for sampling experiments.

The soots produced from the 2-stroke diesel engine were sampled during (1) the 3rd week of March voyage to Mokpo, (2) the 3rd week of April voyage to Yeosu, (3) the 3rd week of May voyage to Jeju and (4) the 3rd week of June voyage to Philippine. As shown in **Fig. 2-3, 2-4**, there were four different sampling locations in the vessel, 1) after the turbocharger(TC) 2) before the economizer(ECO), 3) after the economizer and 4) before the funnel of the chimney. The soots produced from the 4-stroke diesel engine burning Bunker B and C were sampled from the funnel pipe.

At each of sampling locations, a sampling probe was installed and connected to a dilution chamber. The flow containing soot was then introduced to the chamber (diluted with nitrogen) due to the effects of negative pressure caused by a vacuum pump. In the dilution chamber, soots were sampled using TEM grid for 1~5 minutes for HRTEM analysis. In addition, soots for Raman spectra analysis were collected on a glass fiber filter installed in front of the vacuum pump (that eventually draws the PM samples into the glass fiber filter), as shown in **Fig. 2-5**.

For manufacturing Li-ion batteries, soot deposits were collected from the probes inserted in the exhaust pipe of the main engine of T/S HANBADA as shown in **Fig. 2-6**.



Fig. 2-3 Pictures of sampling locations for soot from 2-stroke engine

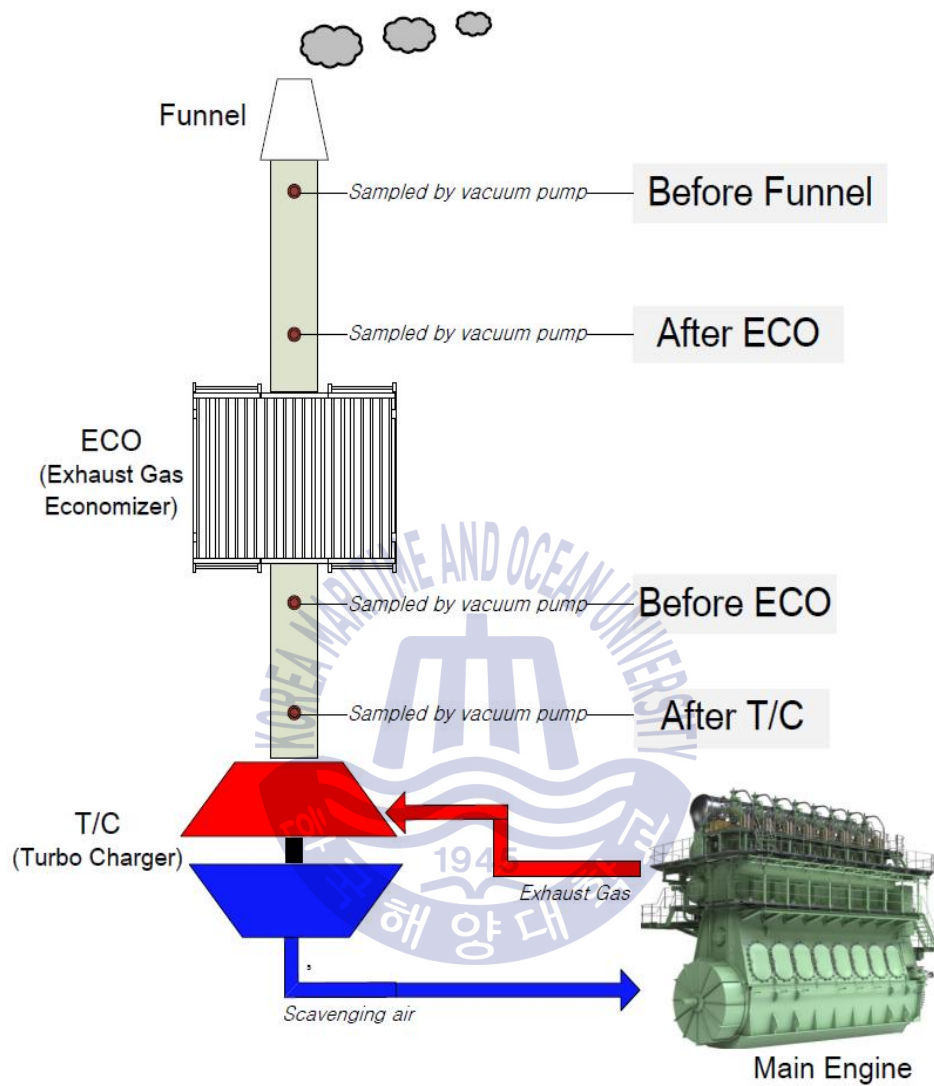


Fig. 2-4 Schematics of sampling locations for soot



Fig. 2-5 Picture of the soot samples collected from the engines



Fig. 2-6 Picture of sampling the soot deposits

2.4 Structure analysis equipment

The soot samples and soot deposits were analyzed using Raman spectroscopy and High resolution transmission electron microscopy (HRTEM) as shown in Fig. 2-7, 2-8.



Fig. 2-7 Raman spectroscopy



Fig. 2-8 High resolution transmission electron microscopy (HRTEM)

2.5 Manufacture of Li-ion battery

Coin cells are widely used in research laboratories to test new battery materials; even for the research and development that target large-scale and high-power applications, small coin cells are often used to test the capacities and rate capabilities of new materials in the initial stage.

Coin cells are manufactured and assembled as shown in **Fig. 2-9**. The electrolytes are formed from pastes of active material powders, binders, and solvents and are fed to coating machines to be spread on current collector foils, such as copper for the anode side.

Mixture of polyvinylidene fluoride (PVDF) binder in N-methyl-2-pyrrolidone (NMP) is prepared and a metal foil of the current collector (typically, copper for the anode) is spreaded on to a glass plate. Then, apply the slurry on to the metal foil using a stainless steel spatula and spread the slurry uniformly on to the track using a doctor blade adjusted height of 100 μm as shown in **Fig. 2-10**. Dry the coating in air or vacuum at 70 $^{\circ}\text{C}$ for about 24 hours (which should be adjusted dependent on the material and binder used) as shown in **Fig. 2-11**. Place the coated metal foil between two steel plates (and two weighing papers to protect the coating) and press under a load of ~3000 lb using a hydraulic press as shown in **Fig. 2-12**. Punch the dried coated metal foil into discs of 8 mm in diameter (preferably inside a glovebox) as shown in **Fig 2-13**. Weigh the anodes and wrap them before transferring into the glove box as shown in **Fig 2-14**. Punch the uncoated metal foil of the same material into discs of 8 mm in diameter and weigh these discs.

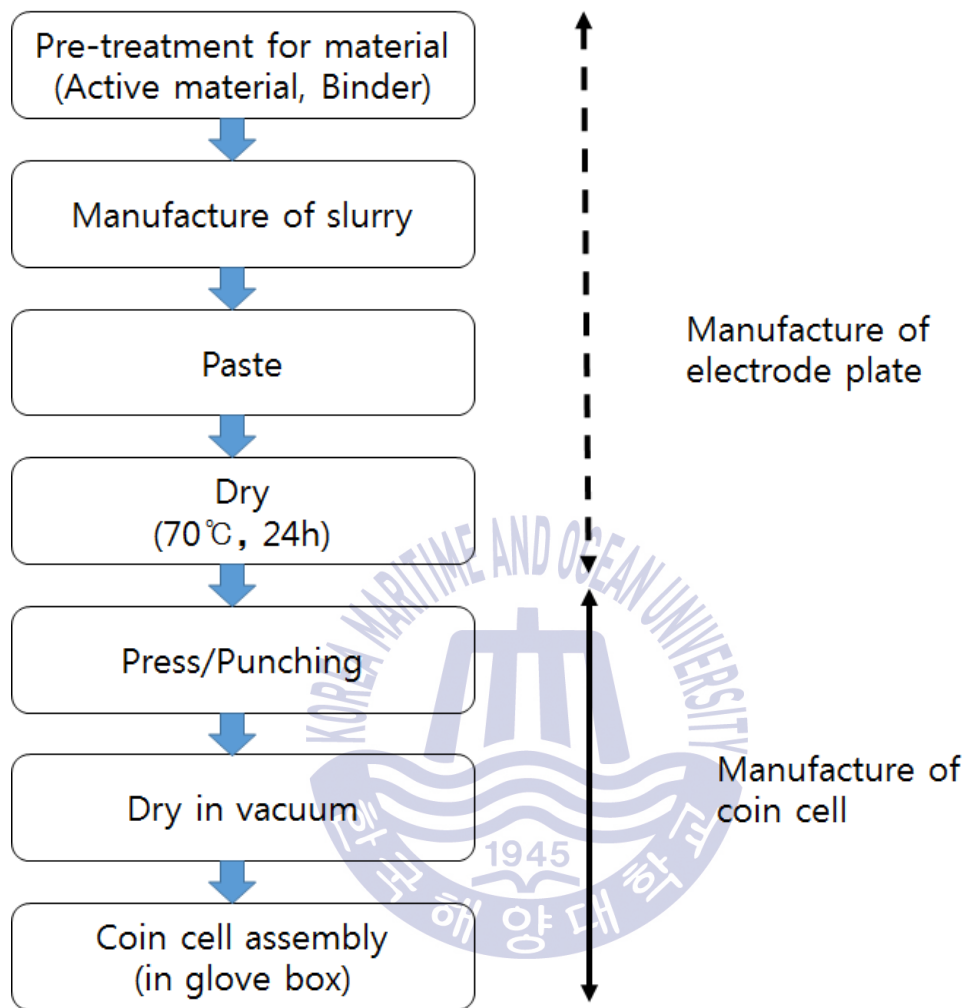


Fig. 2-9 Manufacture of electrode plate and coin cell

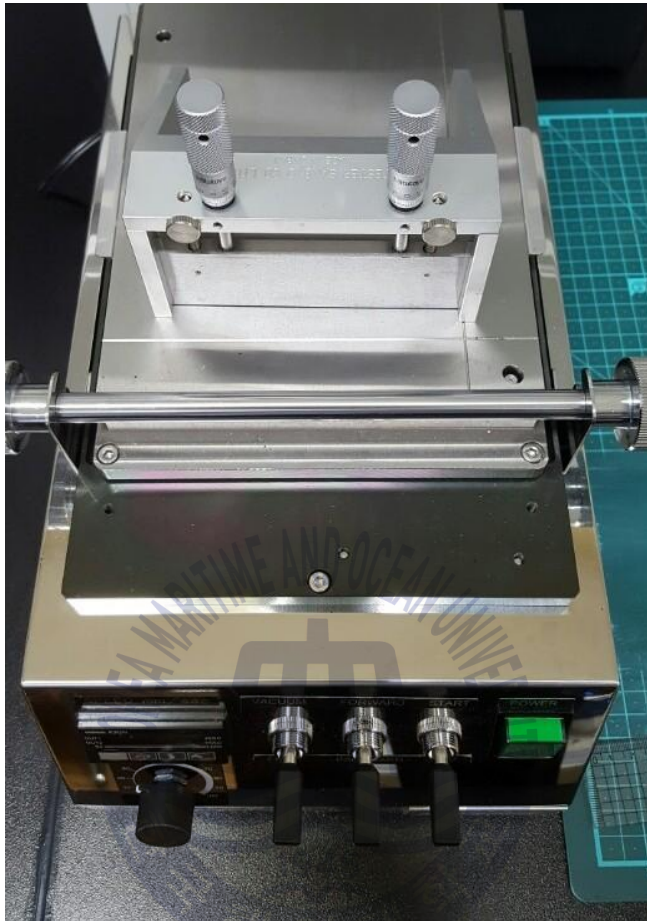


Fig. 2-10 Doctor blade



Fig. 2-11 Vacuum oven



Fig. 2-12 Roll press



Fig. 2-13 Punched anodes



Fig. 2-14 Weighing the anodes

For the assembly of coin cell, coin cell cases (CR2032), springs and spacers, separators and working electrodes are transferred into the glove box (after flushing the exchanger five times with argon). Then the coin cells are assembled in the glove box as shown in Fig. 2-15, 2-16. Two drops of the electrolyte are added on to the cell cup and the working electrode is placed on it. Another three drops of the electrolyte are added and two separators with two drops of electrolyte are placed between them. Two more drops of the electrolyte are added before placing the lithium counter electrode on it and two stainless steel spacers and a spring are placed on the lithium disc. The cell is closed using the cell cap and crimped 3-4 times using the compact crimping machine as shown in Fig. 2-17. Clean the excess electrolyte leaking from the sides of the cell using a paper napkin. The cell is ready for testing and can be taken out of the glove box as shown in Fig. 2-18.



Fig. 2-15 Glove box charged with argon gas



Fig. 2-16 Assembly of a coin cell in the glove box

Chapter 3. Characterization of carbonaceous particulate matter:

Influence of sampling location and engine operation condition

3.1 Introduction

Since soot is comprised of mostly carbon, it is generally accepted as carbonaceous particulate matter (PM) in combustion research communities. However, due to its complicated nature in chemical compositions, the classification of soot differs depending on the intention of the practitioners. In many environmental practices, soot (or carbonaceous PM) is fractionated into black carbon (BC) or organic carbon (OC). Once soot is sampled, the sample is heated to a high temperature (typically ranging from 500 to 550 °C) for a sufficiently long time to evaporate the volatiles (Watson et al., 2005). The residual carbonaceous matter is often called elemental carbon (EC). In the current BC/OC inventory, the measured EC is treated as BC and the other sooty material that was evaporated is treated as OC. However, it is important to note that the BC/OC inventory measured in this manner usually do not involve any direct optical measurement of carbonaceous particulate matter. BC as a part of carbonaceous particulate matter is typically emitted through the incomplete combustion process and considered to be an important short-lived climate forcing (SLCF) substance. BC released to atmosphere absorbs the light and radiates it back to the surrounding atmosphere and thus affects the global climate through the following effects (Garderet & Emmett, 2009; Ramanathan & Carmichael, 2008):

(1) Direct effect: BC absorbs the light from the sun as well as from the surface of earth and radiates it back to the atmosphere, warming the surrounding atmosphere as well as the planet.

(2) Indirect effect: The absorption of sunlight by low clouds increases the

stability of atmosphere below the clouds and reduces the vertical mixing of moisture to the cold base, consequently thinning the clouds to increase the solar energy input reaching the earth surface.

(3) Dark (or dirty) cloud effect: The reduced albedo of darker clouds causes additional warming.

(4) Snow/ice albedo effect: Soot deposition increases melting of ice masses, and the resulting meltwater has a significantly higher heat retention capability than the snow/ice.

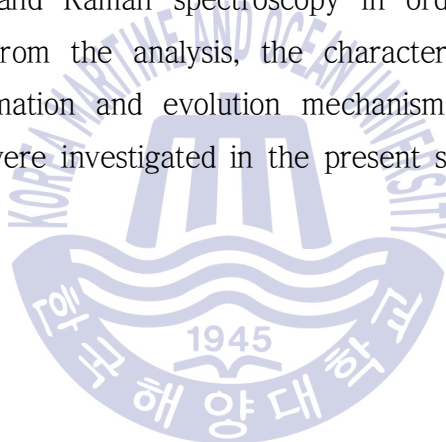
As described above, a consensus for the clear cut definition of BC does not exist and the underlying physical assumptions for different research works are not consistent either. This leaves a great uncertainty in interpreting the results of studies on the BC-related climate forcing to yield conclusive BC climate impact analysis results. Moreover, there is no quantitative physical data set that enables us to directly correlate the current BC/OC inventory to the radiation forcing by carbonaceous PMs released to the atmosphere.

There have been a lot of discussions to regulate BC emissions particularly in the marine and shipping sector, as they are of particular concern for climate change (Lack & Corbett, 2012; Corbett et al., 2010). For example, the International Maritime Organization (IMO) which is the international governing body in the international shipping sector recently took its first action toward addressing the impacts of BC emissions from marine shipping activities on the Arctic. In particular, BC emissions north of the 40th parallel are attributed to marine shipping activities (which are assumed to be a significant source contributor in the Arctic). In recent studies (Arctic council, 2011; USEPA, 2012), BC emissions north of the 40th have been highlighted and believed to affect snow melt in the Arctic as well as total BC-related forcing in the Northern Hemisphere. However, the IMO does not yet have a mechanism to

regulate BC emissions due to the absence of a clear definition of BC.

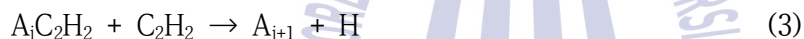
The present study aims to characterize soots collected from marine diesel engines to help the Korean shipbuilding industry to effectively cope with the upcoming regulation for BC emissions. To this end, BC is fractionated from soots, based on the molecular structure and soot formation mechanism. The BC as part of soots was assumed to dominantly constitute the graphite-like flat molecular structure.

The soot samples collected from a 2-stroke marine diesel engine burned Bunker B were then analyzed by a high resolution transmission electron microscopy (HRTEM) and Raman spectroscopy in order to investigate their molecular structure. From the analysis, the characteristics of the molecular structure as well formation and evolution mechanism of soot emitted from marine diesel engine were investigated in the present study.



3.2 Soot formation mechanism

Although soots are usually fractionated into BC or OC in current practices, no unique scientific guideline to define BC or OC exists as discussed. In the present study, the formation of soot was interpreted based on the soot formation mechanism in order to effectively fractionate soot. In that mechanism, the hydrogen abstraction and carbon addition (HACA) concept that was first introduced by Frenklach and Wang (1991) plays an important role in following reactions:



where A_i is the aromatic molecule with i peri-condensed rings and A_{i-} is a radical. Three major steps in the HACA mechanism for sequential molecular growth include H atom abstraction, Eq. (1) followed by gaseous C_2H_2 addition to the radical site, Eq. (2) (which results in molecular growth, and cyclization of PAH). Obviously, C_2H_2 is not the only species which promotes the growth of aromatic rings. High-order aromatic rings can be produced by replicating the HACA reaction. For this reaction process, two aromatic rings are combined, forming biphenyl through a polymerization process. The molecular growth of aromatic rings then continues via C_2H_2 addition, resulting in larger PAHs.

When the molecular weight of PAH reaches a critical range, the transition of gas-phase species to solid particles (i.e., particle inception) occurs. It is known that this transition takes place at a molecular weight of 300 ~ 700 amu. PAHs with this molecular weight physically begin to condense into

tar-like particles (Frenklach & Wang, 1991; Frenklach, 2002). Alternatively, the PAH monomers begin to coagulate with each other through collisions and thus form PAH dimers. PAH dimers again collide with other PAH molecules, forming PAH trimers and so on. Consequently, these PAH clusters carbonize into solid particles as they increase in molecular weight as illustrated in **Fig. 3-1**. When high temperature-enabled pyrolysis reaction is dominated at these stages, PAHs decompose into smaller species such as C_2H_2 (Frenklach, 2002; Bockhorn & Schafer, 1994). Furthermore, higher temperatures will activate more surface sites due to removal of activation energy barriers, enabling more HACA reactions (which eventually result in the carbon mass growth at the surface site). This will lead to prevalence of more graphitic nanostructures, producing graphene-like flat carbon structure with SP^2 bond (that has carbon structures similar to EC). In contrast, the reaction pathway for PAH growth is preferred due to inhibitions of the fragmentation of chemical bonds when low temperature-enabled pyrolysis reaction is dominant (Frenklach, 2002; Bockhorn & Schafer, 1994). This will result in large PAHs (as a result of collision with different gaseous species) and form PAH condensates, eventually resulting in amorphous molecular structures with more SP^3 bond similar to OC (Vander Wal & Tomasek, 2004).

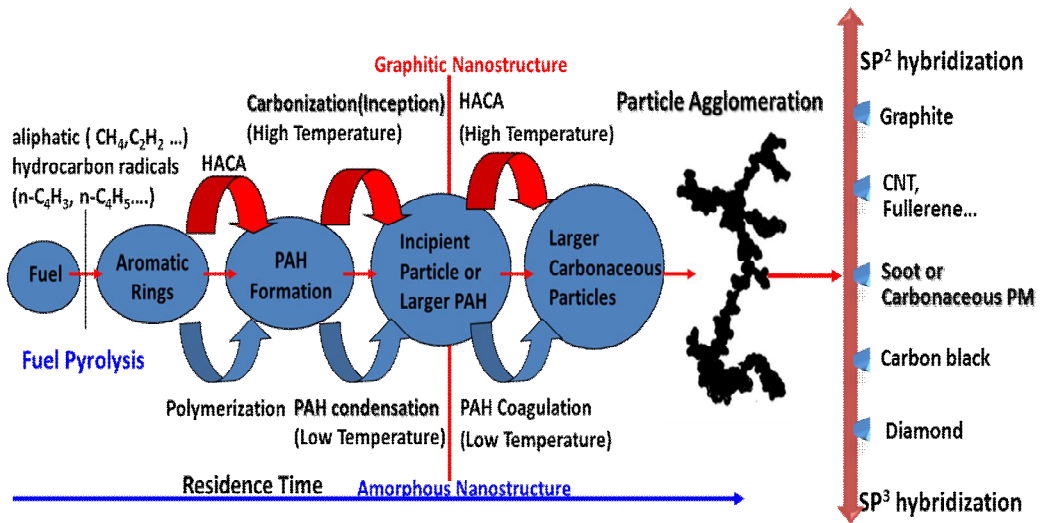


Fig. 3-1 Conceptual diagrams for soot formation mechanism and molecular structures of carbonaceous materials



3.3 Soot nanostructure

3.3.1 Influence of sampling location on nanostructure

When carbonaceous particles become mature (i.e., when the graphitization process is decreased due to the reduction in the number of active sites on the particles for surface mass growth), those particles begin simply to stick to each other producing chain-like agglomerates that contain 30–1800 individual spherical particles (Haynes & Wagner, 1981). These stages are classified as coalescent growth and agglomeration, respectively.

Soots sampled were first analyzed by HRTEM to investigate the characteristics of the molecular structure. **Fig. 3-2** displays HRTEM images of soot obtained at low magnifications of 800 X. Soots were collected from the sampling locations a) (T/C exit) and b) (ECO exit) for a cruising engine speed of 120 rpm, respectively. Chain-like wispy agglomerates consisting of a number of individual spherical particles are clearly seen in the figure. In addition, it is observed that tar-like condensates in a spherical shape (marked with triangular symbols) form and stick to each of agglomerates. Interestingly, tar-like condensates sampled at the ECO exit were larger and more than those collected at the TC exit.

Mean exhaust gas temperature ranged from 275 to 333°C depending on the cruising engine speeds and operating modes (see **Fig. 3-3**). And exhaust gas temperature measured at the T/C exit was around 300°C, while that at the ECO exit was as low as 220°C (see **Fig. 3-4**). Because of such a low temperature between the T/C and ECO exits, higher order of PAHs can be easily condensed to form OC layers on the agglomerates so that more pronounced amorphous morphological characteristics of agglomerates are anticipated as moving the sampling point downstream (i.e. toward the ECO exit).

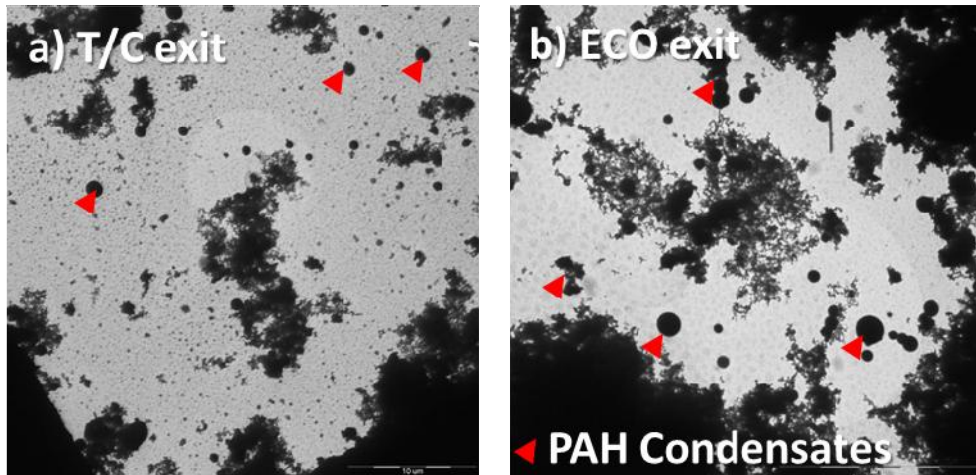


Fig. 3-2 HRTEM images of carbonaceous agglomerates collected at a) the TC exit and b) the ECO exit

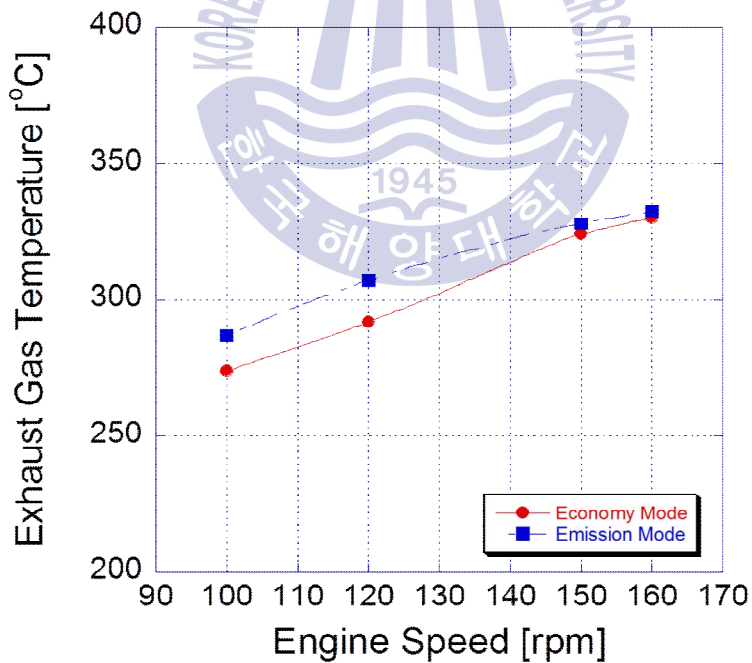


Fig. 3-3 Measured exhaust gas temperature at the T/C exit as a function of a cursing engine speed

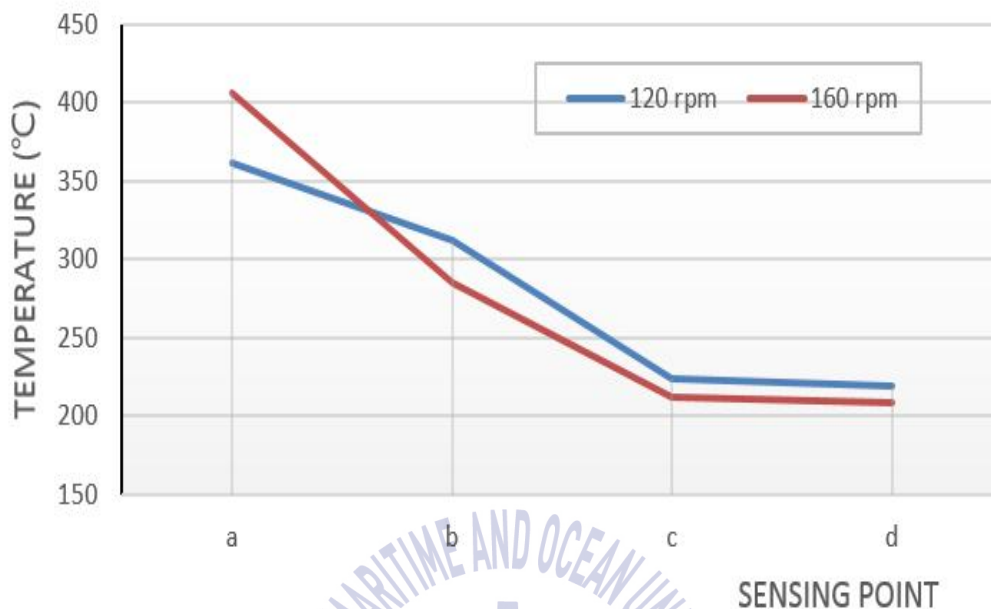
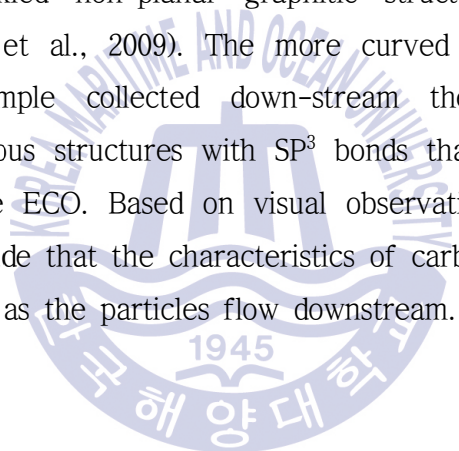


Fig. 3-4 Measured exhaust gas temperature as a function of the sampling location. a) T/C inlet, b) T/C exit, c) ECO exit, d) Funnel.

To further examine the morphological evolution in the exhaust gas stream, soots collected at three different sampling locations A (T/C exit), B (ECO exit), and C (chimney funnel) were imaged at higher magnifications. **Fig. 3-5** shows a series of HRTEM images of soot sampled at different locations. The upper images in the figure are magnified 34,000 times while the lower images are magnified 145,000 times. A clear qualitative distinction between the samples at the exit of the T/C and ECO can be observed from the upper and lower HRTEM images. In the upper images, as the sampling location moves downstream, the distinctive contrast between individual spherical particles becomes weaker, indicating that the particles tend to scatter more light to be less contrasting. It would be conjectured that the radiative properties of collected particles tend to evolve from black-body's character to

gray-body' s character as the sampling location moves downstream. It can be attributed to dominated PAH formation and condensation (relative to the decomposition of PAH) at lower temperatures leading to disordered graphitic structure, i.e., amorphous structure.

The formation of amorphous structure as a sign of OC formation at the edge of particles can be more clearly seen from the lower HRTEM images magnified at 145,000X. It is generally accepted that the amorphous structure is related to non-planar graphitic structures. The presence of carbon bonds with SP³ hybridization on the carbon basal plane strains the structures, there by resulting in wrinkled non-planar graphitic structures (Vander Wal & Tomasek, 2004; Park et al., 2009). The more curved graphitic structure as observed in the sample collected down-stream therefore indicates the abundance of amorphous structures with SP³ bonds that formed through the cooling process in the ECO. Based on visual observations from the HRTEM images one can conclude that the characteristics of carbonaceous PMs become closer to those of OC as the particles flow downstream.



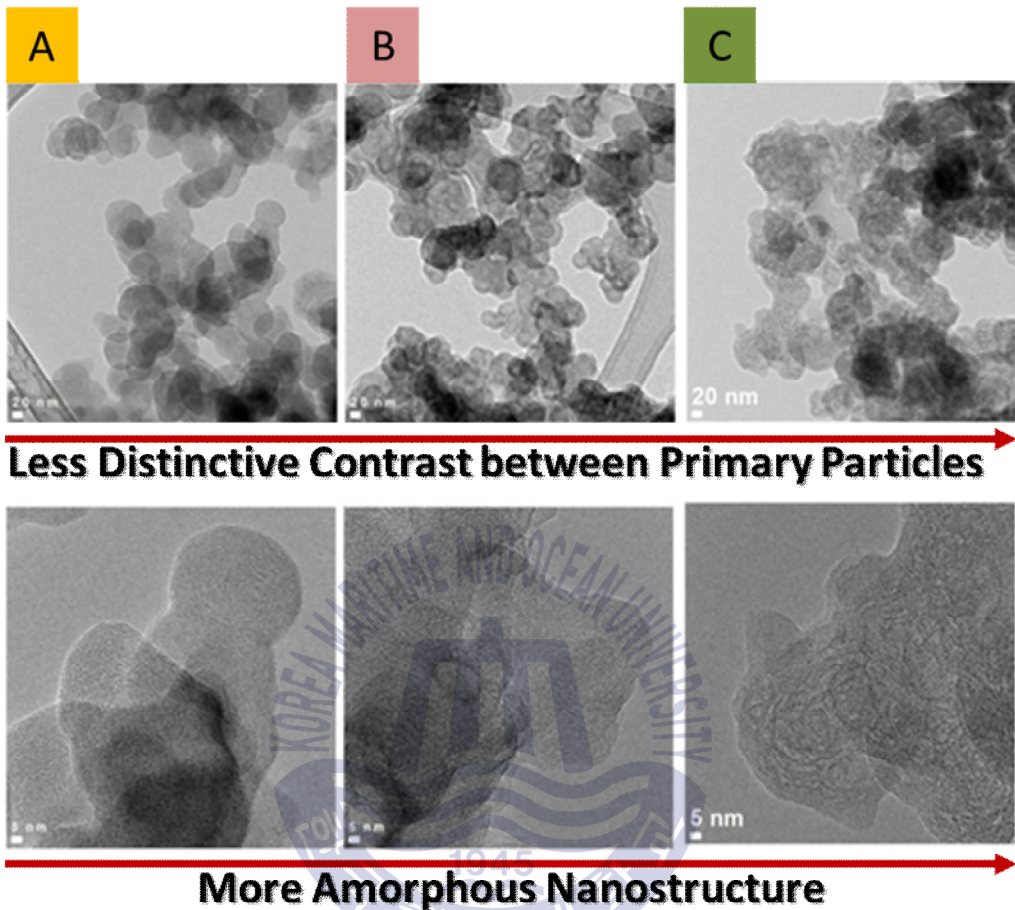
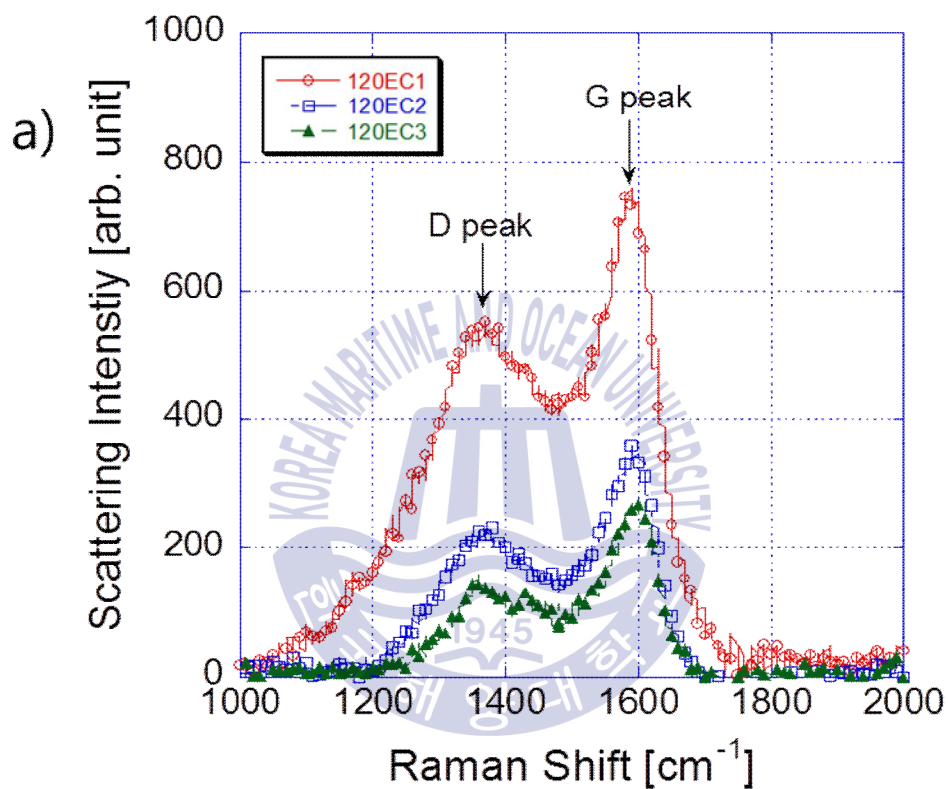


Fig. 3-5 HRTEM images of individual spherical particles collected from A) T/C exit, B) ECO exit, and C) chimney funnel

3.3.2 Influence of engine speed on graphitization

To quantitatively investigate the influence of engine speeds on the BC/OC ratio in sampled soots, the Raman scattering intensities are measured for the samples collected on the glass fiber filter at the engine speed of 120rpm and 160 rpm, respectively. All soot samples used for Raman intensity measurements were collected at the ECO exit. The scattering intensities were

then measured for multiple samples. Fig. 3-6 displays the measured Raman intensity spectra for samples collected at two different engine speeds.



	120EC1	120EC2	120EC4
D peak	568.1	257.2	179.1
G peak	790.3	392.3	279.0
G/D peak	1.39	1.53	1.56
G/D peak avg.		1.49	

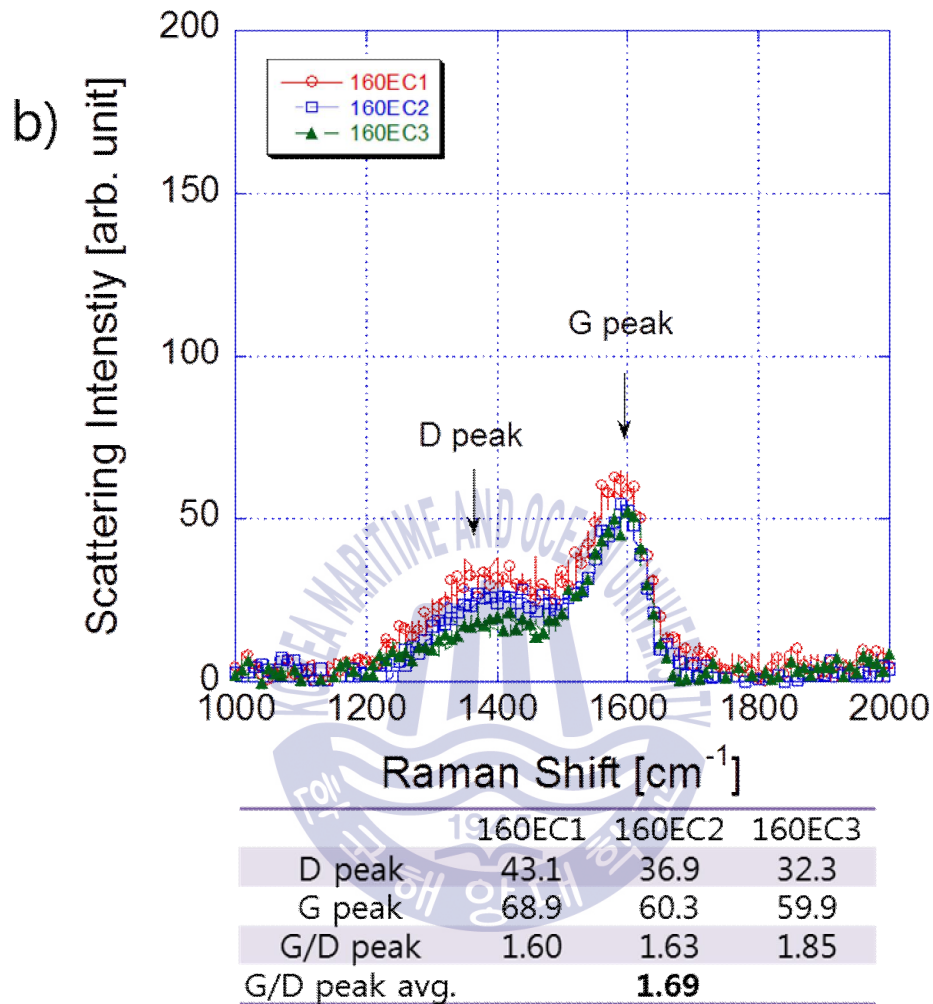


Fig. 3-6 Raman intensity plot for soots sampled at the engine speed of a) 120 rpm and b) 160 rpm

As shown in the figure, two distinct (D and G) peaks are observed for both cases which indicate the presence of graphitic and amorphous structures. In the figure, the D peak (1350 cm^{-1}) represents disorder in the structure while the G peak ($1580 \sim 1600\text{ cm}^{-1}$) represents graphitic elements within the carbon structure (Ferrari & Robertson, 2004). In the present study, it is

postulated that BC has a graphitic morphological structure with SP^2 bond, while OC has an amorphous morphological structure with SP^3 bond. Therefore, the ratio of G peak to D peak intensity would represent a measure of BC/OC ratio in the collected soots. The average G/D peak intensity ratio for the samples collected at 120 rpm is 1.49 while that for samples collected at 160 rpm is increased to 1.69 (which indicates higher degree of graphitization compared to samples collected at 120 rpm). A higher RPM can produce stronger combustion intensity, leading to higher combustion temperature. However, the combustion temperature in operation was not measured in the present study since modifications to install the additional sensors for the measurements were permitted to a minimum level during voyages.

Nevertheless, as shown in **Fig. 3-7**, increases in the NO_x emissions and exhaust gas temperature clearly supports more intensified combustion achieved by higher combustion temperatures and pressures in comparison with 120 rpm. Because of more efficient combustion, the ratio of BC to OC can increase as seen from the increased fraction of SP^2 bonds to SP^3 bonds in Raman spectra analysis provided in **Fig. 3-6**. Higher temperatures and pressures activate more surface sites due to removal of activation energy barriers, enabling more HACA reactions which eventually result in the carbon mass growth at the surface site. This will lead to prevalence of more graphitic structures enhancing the ratio of BC to OC.

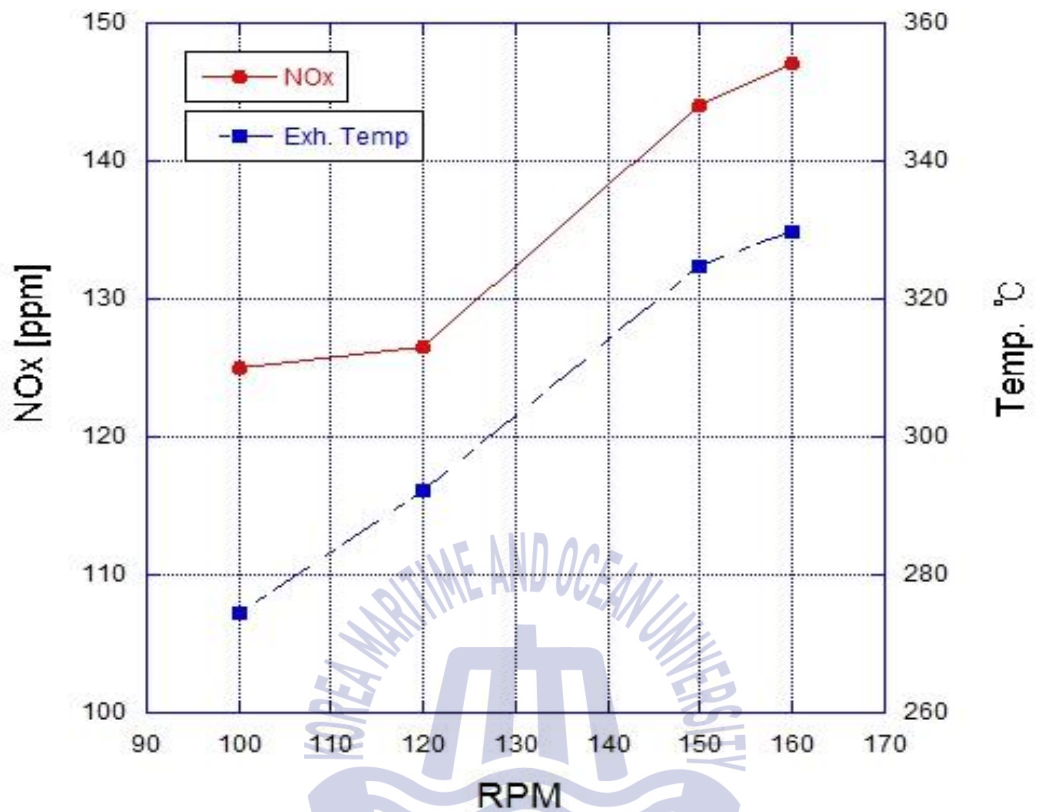


Fig. 3-7 Variations in the NOx and exhaust gas temperature as a function of the engine speed

3.4 Conclusion

Since no unique scientific definition for BC exists, the underlying physical assumptions for climate model to estimate the airborne PM and BC impacts differ by every climate model. The consequent BC radiation forcing, therefore, varies in a wide range as a result of absence of a clear physical definition of BC. Although there is an issue of continuing debates in the airborne BC atmospheric warming effects, the IMO initiated a process to derive a regulation standard for PM and BC emissions, recently. The present study is a part of efforts to characterize the soot emitted from the marine diesel engines. The soot was sampled from the main propulsion engine (2-stroke diesel engine) burned Bunker B during four training voyages of T/S HANBADA and then analyzed using the Raman spectroscopy and HRTEM. Followings are the main findings obtained from the experimental campaign:

(1) Higher order of PAHs in the exhaust gas can be condensed as they transport downstream, forming tar-like condensates. More tar-like condensates are observed as moving the sampling point downstream (i.e. toward the ECO exit). This result implies that amorphous morphological characteristics of agglomerates can be pronounced, increasing the OC ratio in soots collected downstream.

(2) The HRTEM images exhibit a distinct qualitative change before and after the economizer in that wrinkled non-planar graphitic structures are found more frequently after the economizer. This difference in the HRTEM images indicates that the BC particles are mainly formed by the HACA mechanism during the combustion process while the OC particles are formed by PAH condensation and coagulation due to the cooling of the exhaust gas cooling in the economizer.

(3) The Raman spectroscopic analysis revealed that the ratio of BC to OC

in collected soots increases with increasing the cruising engine speed from 120 rpm to 160 rpm. At the cruising engine speed of 160 rpm, combustion is more efficient, so that the BC/OC ratio as well as NO_x emission increases mainly due to higher temperatures and pressures.



Chapter 4. Characterization of carbonaceous particulate matter: Influence of engine type and fuel quality

4.1 Introduction

For marine diesel engines only gaseous emissions are limited yet, but in view of legislation to come it is important to characterize particle emissions from those engines (Kasper et al., 2007).

For many decades, many studies on particle emissions were conducted, which focus on particle emissions from on land vehicles; yet studies on particle emissions from ships are very limited. The differences between on land and marine diesel engines are quite significant. They are operated with highly different fuels. Engines operated on land use refined, high-quality fuels, while marine diesel engines are operated with bunker fuels containing high amounts of sulfur (Kasper et al., 2007). Furthermore, the study of the influence of ship's fuel quality on particle emissions is rare or there have been relatively few studies performed (Lack & Corbett, 2012). Recently, it has been observed that better quality fuels (i.e., processed distillates versus residual blends) reduce particulate sulfate and organic particles from unburned lubricating oil and fuel (Lack et al., 2009; Lack et al., 2011). Lack et al., (2009) studied the effect of fuel sulfur on particle size of diesel soot from ship, which showed that high sulfur containing fuels produce smaller particles than low sulfur containing fuels. Fuel formulation also affects soot emissions and soot characteristics. Many researchers have found that various oxygenated diesel fuel additives, such as methyl esters, lead to reductions in particle emissions (Choi & Reitz, 1999; Miyamoto et al., 1998; Lapuerta et al., 2005). Vander Wal & Tomasek (2003) showed that the soot samples generated by benzene, ethanol and acetylene have different structural order and reactivity. Benzene-derived soot is found to have a more amorphous structure and is

more reactive than acetylene-derived soot. Douce et al. showed that fuel type has an impact on soot yield and sphere size using a shock tube (Douce et al., 2000).

On the other hand, there are two kinds of diesel engines in the ocean going vessel normally, 2-stroke engine and 4-stroke engine. Large bore low speed 2-stroke marine diesel engines dominate as prime movers and medium speed 4-stroke marine diesel engines play a role in electric power generation for the cargo ships, because of their high efficiency, reliability, excellent fuel economy, torque, and low operating costs (Mun et al., 2016; Sharma et al., 2012). However, emissions from diesel engines contain fine particles produced high temperature pyrolysis or combustion. Carbonaceous diesel particulate matter (PM), also known as soot, is primarily composed of carbon. Soot formation is a complex phenomenon, which is strongly dependent on the combustion characteristics such as a result of fuel spray development, air/fuel ratio and compression ratio decided by engine type.

The impacts of the combustion process on PM emissions and properties have been studied by several researchers. Chan and Cheng (2007) showed that soot emissions were affected by engine operating conditions and fuel injection timing using a numerical model for diesel engine combustion. Smaller soot particles are observed at higher engine speed because of the shorter residence time. Zhu et al., (2005) found that the degree of order of soot nanostructure increases when engine load and exhaust temperature increase. In addition, because of particle oxidation at high in-cylinder temperatures, a decrease in soot particle size is observed with an increase of the exhaust temperature. Braun et al., (2005) studied difference of diesel soot characteristics between idle soot and load soot. They concluded that load soot had a higher degree of crystallinity and smaller primary particles than idle soot. The microstructure and oxidation behavior of exhaust soot from a heavy

duty (HD) diesel engine were investigated by Su et al., (2004).

Detailed knowledge about size, shape, and structure of diesel soot is important to understand the impact of the particles on the human body and be able to carry out more meaningful source assignments. From an engineering point of view, such information may also be useful for understanding the interaction of diesel soot particles with the engine and pollution abatement devices (Ciambelli et al., 2002).

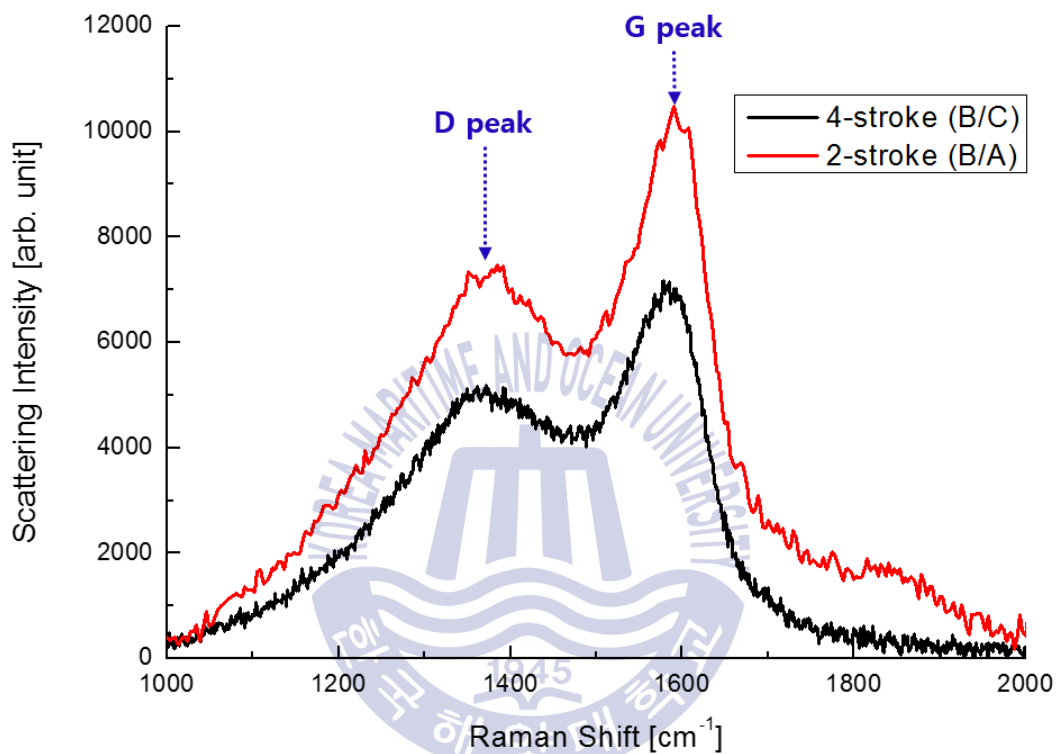
This study presents some results from the tail pipe emissions of the diesel soot from a 2-stroke main engine and a 4-stroke generator engine under fixed load using two different fuels (Bunker A and C). The morphologic and molecular structure of soot particles from ship was characterized using Raman spectroscopy and HRTEM (Braun et al., 2005). Although the analysis of HRTEM image can provide the useful interpretations of soot nanostructure, they are strongly dependent upon visual observations that preclude quantitative measures or comparisons. For more accurate and non-subjective interpretations (Shaddix et al., 2005), the digital analysis of soot nanostructure was conducted using image process techniques in this work.

4.2 Soot nanostructure

The present study focuses on the influence of engine type and fuel quality on diesel soot properties. Soot property analyses were performed using Raman spectroscopy and HRTEM. The applied magnification was set at 32,000 times for cluster of spherules, and 620,000 times for nanostructure analysis. For a more quantitative interpretation, soot nanostructure imaged using HRTEM were analyzed by fringe analysis technique measuring the structural characteristics of carbon lamellas such as the length and degree of curvature. The fringe analysis based upon computer-aided image processing techniques has been used to interpret the nanostructure of combustion generated soot. The fringe analysis permits us to estimate the fringe length and the curvature of the fringe.

The disordered graphitic structure in diesel soot observed in HRTEM images was further characterized using Raman spectroscopy. Based on the degree of graphitization in the carbon soot, different structural characteristics of soot can be distinguished. The D and G peaks of amorphous carbon can be fit to assess the degree of disorder or graphitization present. Raman spectra of diesel soot typically shows two overlapping peaks. The graphitic G peak of the graphite-like structures of the soot occurs at around 1580~1600 cm^{-1} and the D peak for the disordered structures occurs at around 1350 cm^{-1} . The height-ratio of the two peaks G/D decreases with order for amorphous and disordered carbons and increases with increasing order for graphitic carbons. **Fig. 4-1** displays the measured Raman intensity spectra and G/D peak for samples collected from two different engines. As shown in the figures, two distinct peaks are observed for both cases which indicates the presence of graphitic and amorphous structures. The G/D peak intensity ratio for the sample collected from the 2-stroke engine is 1.337 while that for sample

collected from the 4-stroke engine is increased to 1.395 (which means higher degree of graphitization compared to samples from the 2-stroke engine).



	2-stroke Bunker A	4-stroke Bunker C
G peak	11164.84	6888.796
D peak	8347.03	4938.15
G/D	1.337	1.395

Fig. 4-1 Raman intensity plot and G/D peak for diesel soot sampled from 2 & 4 stroke engines

Diesel soot particles sampled from each engine burned different fuels were analyzed by HRTEM to investigate the characteristics of the molecular structures. **Fig. 4-2** displays HRTEM images of diesel soot obtained at low magnifications. Agglomerates of a number of individual spherical primary particles can be clearly seen in both two cases. Soot particles are irregular clusters with different size and densities. The size of the spherical primary particles in soot of the 4-stroke engine is smaller than that of the 2-stroke engine. A noticeable reduction in primary particle size may originate from increasing of exhaust gas temperature (Zhu et al., 2005). Exhaust temperature of the 4-stroke engine is higher than that of the 2-stroke engine due to the overlap period between scavenging stroke and exhaust stroke during combustion (Woodyard, 2004). And combustion pressure and mean effective pressure of 4-stroke engine is higher than that of the 2-stroke engine, which make exhaust temperature of the 4-stroke increase. Additionally using heavy fuel oil (Bunker C) increases exhaust temperature, compared to the use of light oil (MAN, 2008). Also, the reduction of the primary particle size supports the result that fuels with high contents of sulfur produce more small particles than fuels that contain low sulfur contents (Lack et al., 2009).

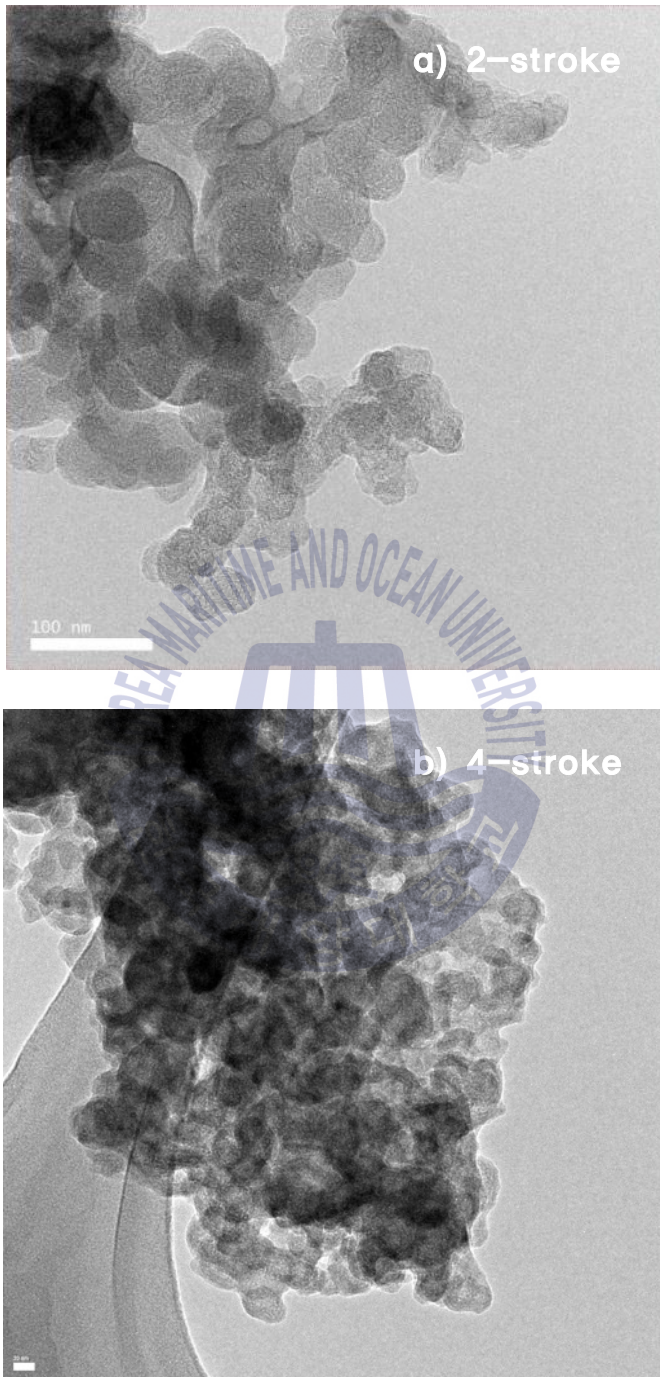


Fig. 4-2 HRTEM images of diesel soot collected from a) the 2-stroke engine;
b) the 4-stroke engine

To further investigate the morphological difference, samples were imaged at higher magnifications. **Fig. 4-3** shows that a qualitative distinction between the samples, 2-stroke and 4-stroke engine, can be observed from the HRTEM image. As shown in the figures, both cases produced significantly different soot nanostructures from each other due to relatively different temperatures. The HRTEM image of the soot sample collected from 4-stroke engine burned bunker C has a higher degree of order which is characterized by extended carbon lamellas with a little observable curvature. The soot sample collected from the 2-stroke engine burned Bunker A, however, shows signs of having a disordered configuration.



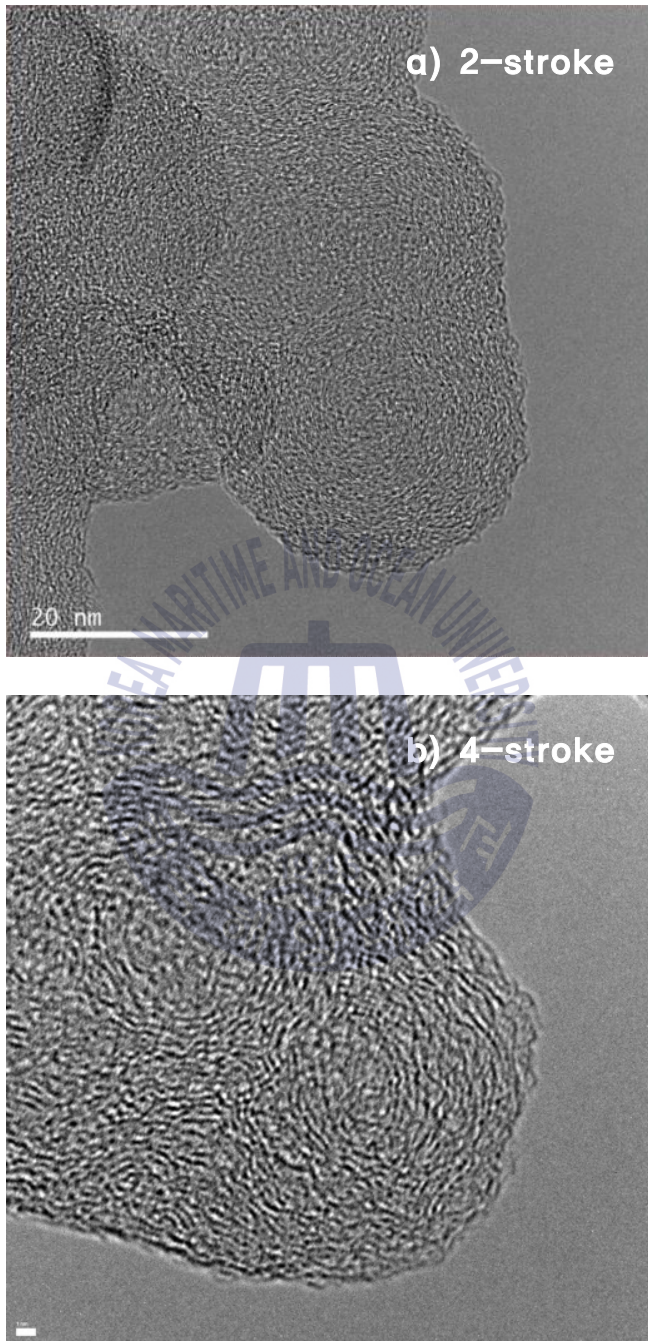


Fig. 4-3 HRTEM images of diesel soot collected from a) the 2-stroke engine; b) the 4-stroke engine at higher magnifications

4.3 Image processing techniques

4.3.1 Fringe analysis algorithm

For a more quantitative interpretation, soot nanostructure has been alternatively analyzed by measuring the structural characteristics of carbon lamellas such as the length and degree of curvature (Palotas et al., 1996; Shim et al., 2000; Goel et al., 2002; Vander & Tomasek, 2004). Since the carbon lamellas appear as fringes in the HRTEM images, a fringe analysis based upon computer-aided image processing techniques has been used as a powerful tool to interpret the nanostructure of combustion generated soot (Shim et al, 2000; Vander & Mueller, 2006). A major challenge for the fringe analysis is related to the conversion of complex carbon lamella structures into a set of distinguishable fringes. Previous studies (Shim et al., 2000) shed light on the detailed image processing techniques for the fringe analysis that provide reproducible and identifiable fringe structure. In this study, a fringe analysis algorithm which operates using Matrox Inspector 8.1® macro script was developed using the model of Shim et al., (2000) and Vander Wal et al., (2004).

To transform the complex internal carbon lamella structures of soot into a set of distinct fringe structures, the fringe analysis algorithm includes the following major steps: (1) pre-processing (2) extracting the carbon fringes (3) skeletonization of extracted fringes and (4) post-processing. The pre-processing procedure includes the correction of uneven background illumination (that is common in the HRTEM imaging) and spatial filtering for noise reduction. The correction of uneven illumination in background across the HRTEM images was performed by offsetting the background and then the spatial filter was applied to reduce the image noises.

The identification of meaningful fringes is one of the critical steps for the fringe analysis. For the fringe identification process, an edge-enhanced filter was first used to accentuate the fringe features. Accentuated fringes are then extracted by setting an appropriate threshold value that gives the maximum number of identified fringes (Palotas et al., 1996). For an 8-bit image (the resolution used for all HRTEM imaging in this study), the threshold value is varied from 0 (i.e., black) to 255 (i.e., white). In this study, the threshold value that produces the maximum number of identified fringes was found to range from 121 to 135 in most cases. Based upon the image processing techniques discussed above, binary fringe images are extracted from the selected region of interest (ROD) in the HRTEM image of soot sampled from 2-stroke engine burned Bunker A and 4-stroke engine burned Bunker C.

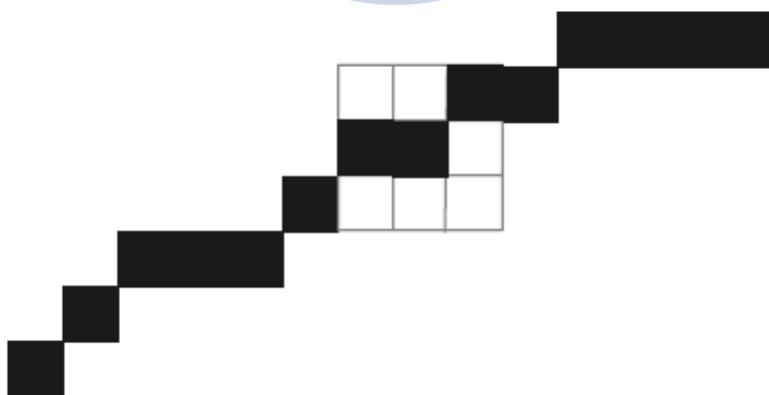
Extracted fringes are further processed by performing a “thinning” operation on the periphery of each fringe until they are reduced to one-pixel in width – a process also known as skeletonization of extracted fringes. During the thinning operation, a 3×3 pixel neighborhood mapping was applied to inspect the neighboring pixels for fringe connectivity. In general, each pixel has a 4 or 8 connected lattice in the 3×3 pixel neighborhood mapping. A 4-connected lattice method considers adjacent pixels along the vertical and horizontal axes as in contact. An 8-connected lattice method considers pixels along the horizontal, vertical and diagonal axes as in contact. In this study, the 8-connected lattice method was applied so that skeletonized fringes with diagonally adjacent pixels were considered as a continuous structure.

Skeletonized fringes may be bisected as a result of filtering and thresholding processes. Therefore, the fringe analysis algorithm includes the post-processing procedure to recover the artificially bisected fringes. The neighborhoods of each fringe end (within the $N \times N$ pixel specified by user-defined parameters) are first scanned (See **Fig. 4-4a**). Two ends of each

fringe whose orientation angle (within $\pm 30^\circ$) is similar are then reconnected and thereafter considered as one fringe (See Fig. 4-4b). Finally, all fringes that are less than 0.25 nm were removed since this dimension is the size of a single aromatic ring and therefore cannot be construed as a fringe (Galvez et al., 2002). The skeletonized fringe image (after the post-processing treatment) for the extracted fringe image is displayed in Fig. 4-5a. Fig. 4-5b displays the reproduced skeletonized fringe image in which fringes in contact with the ROI boundary are eliminated.

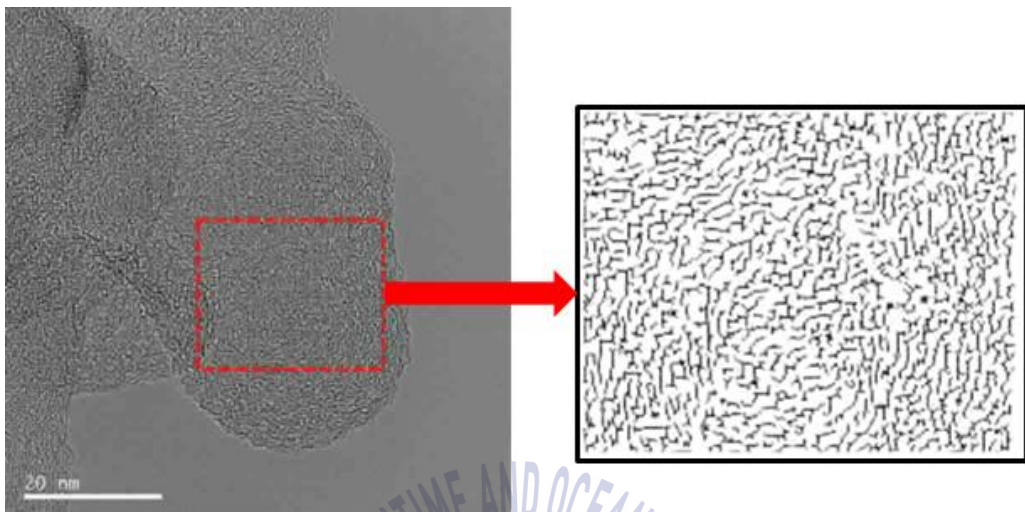


(a) Before post-processing treatment

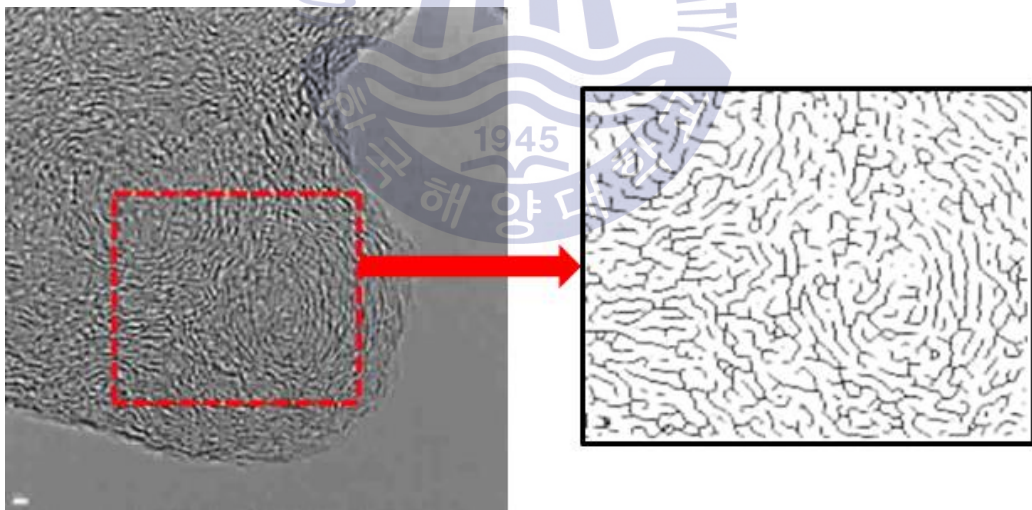


(b) After post-processing treatment

Fig. 4-4 Schematic of fringe reconnection process during post-processing



a) 2-stroke engine burned Bunker A



b) 4-stroke engine burned Bunker C

Fig. 4-5 Skeletonized fringe image of HRTEM image of collected soot

4.3.2 Structural parameters for fringe analysis

In this study, the structural characteristics of a fringe are represented in terms of the fringe length and tortuosity. Fringe length, L_f , was basically calculated by counting the total number of pixels which consists of each skeletonized fringe. For fringes having a diagonally connected lattice, the fringe length was considered as the diagonal length of the square with dimension of 1 pixel by 1 pixel, $\sqrt{2}$. Finally, the fringe length calculated in pixels was converted into the length in nm by using the scale factor, nm/pixel (that is obtained from the scale bar in the HRTEM image).

Tortuosity, f_T , is a parameter that defines the degree of curvature of each skeletonized fringe. In this study, tortuosity is defined as (Shim et al., 2000):

$$f_T = \frac{L_f}{\sqrt{X^2 + Y^2}} \quad (1)$$

where L_f is the length of a fringe within a rectangular box (that encompasses the individual fringe), X is the height of the box, and Y is the width of the box (See **Fig. 4-6**). Tortuosity with a value of one represents a straight fringe.

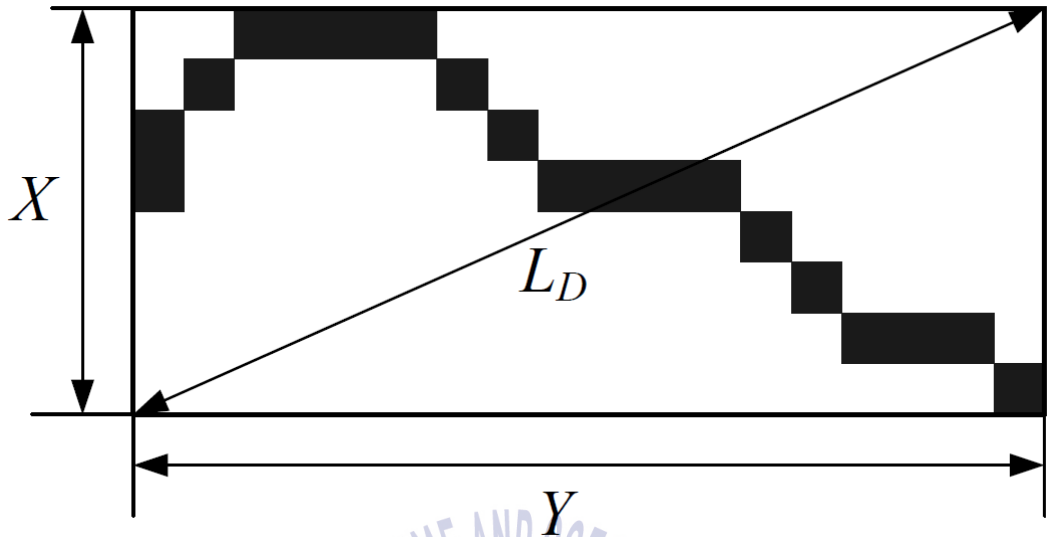


Fig. 4-6 Schematic of a box enclosing a fringe for tortuosity calculation

4.3.3 Measuring data for fringe analysis

As displayed in the figures, soot collected from the experiment in 4-stroke engine burned Bunker C includes longer and more distinct carbon lamellas compared to the experiment in 2-stroke engine burned Bunker A. For soot collected from the 2-stroke engine burned Bunker A, a large number of shorter and disconnected fringes are observed.

To quantitatively clarify the nanostructure of soot from the 2-stroke and 4-stroke engines, the fringe length and tortuosity were measured using digital image process techniques and displayed in Fig. 4-7, 4-8, 4-9, 4-10 with histograms.

The histogram of calculated fringe length for skeletonized fringes displayed in Fig. 4-7, 4-8 clearly supports the visual interpretation that the 4-stroke experiments produce the longer fringes compared to the other case. As shown in the figures, the experiments of the 4-stroke engine burned Bunker C

produce extended fringe length distribution in which most of fringes are greater than 1 *nm* in length whereas the experiments of the 2-stroke engine burned Bunker A produce extended fringe length distribution above 1 *nm* is less than below 1 *nm* - the majority of the fringe length for the 2-stroke engine case is between 0.25 *nm* and 1 *nm*.

Fig. 4-9, 4-10 display the histograms of calculated fringe tortuosity for skeletonized fringes shown in **Fig. 4-5**. The differences in tortuosity between skeletonized fringe images for soot derived from 2-stroke and 4-stroke engine cases are clearly seen. The results indicate that the case of 4-stroke engine burned Bunker C produces straight fringes (tortuosity = 1) compared to that for the case of 2-stroke engine burned Bunker A.



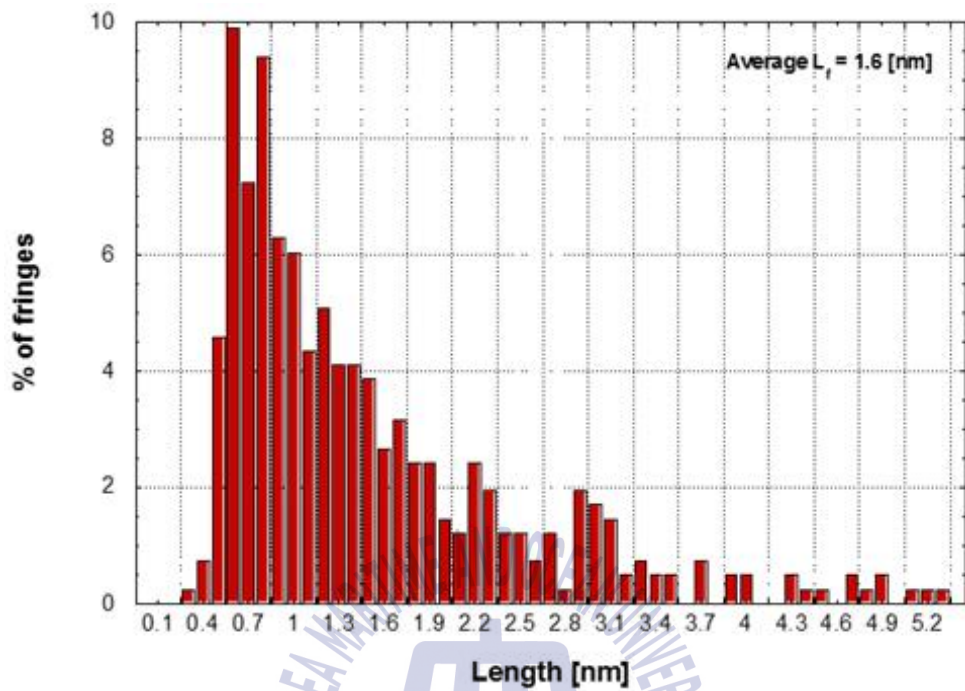
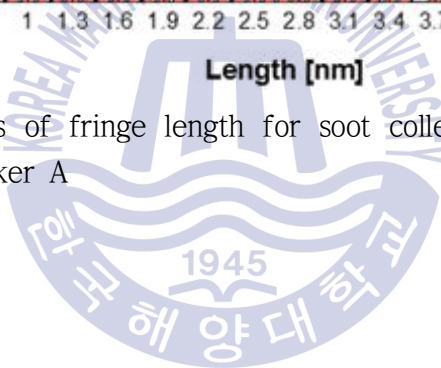


Fig. 4-7 Histograms of fringe length for soot collected from 2-stroke engine burned Bunker A



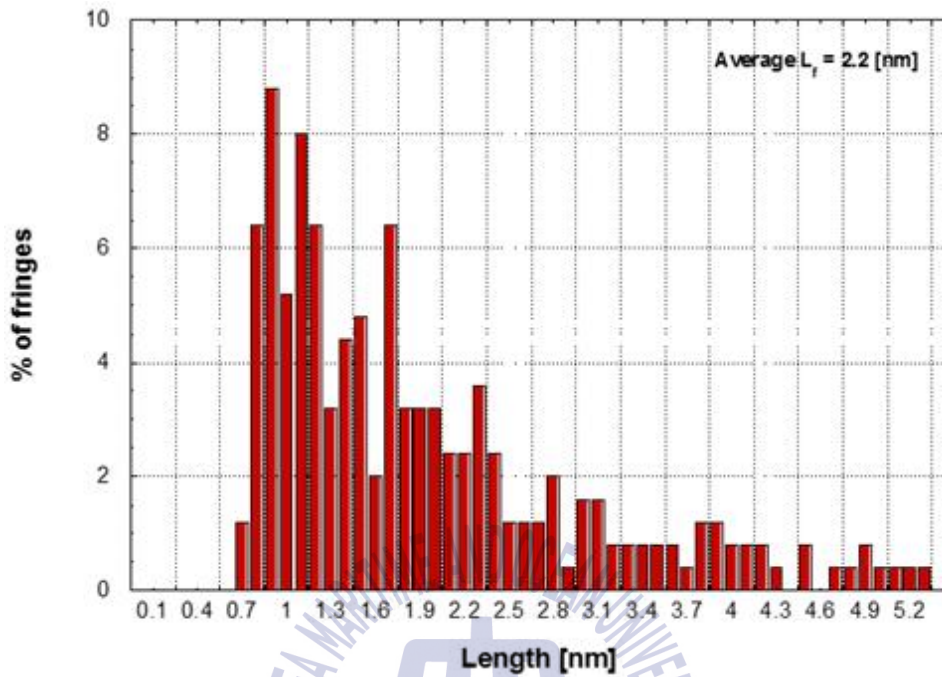


Fig. 4-8 Histograms of fringe length for soot collected from 4-stroke engine burned Bunker C



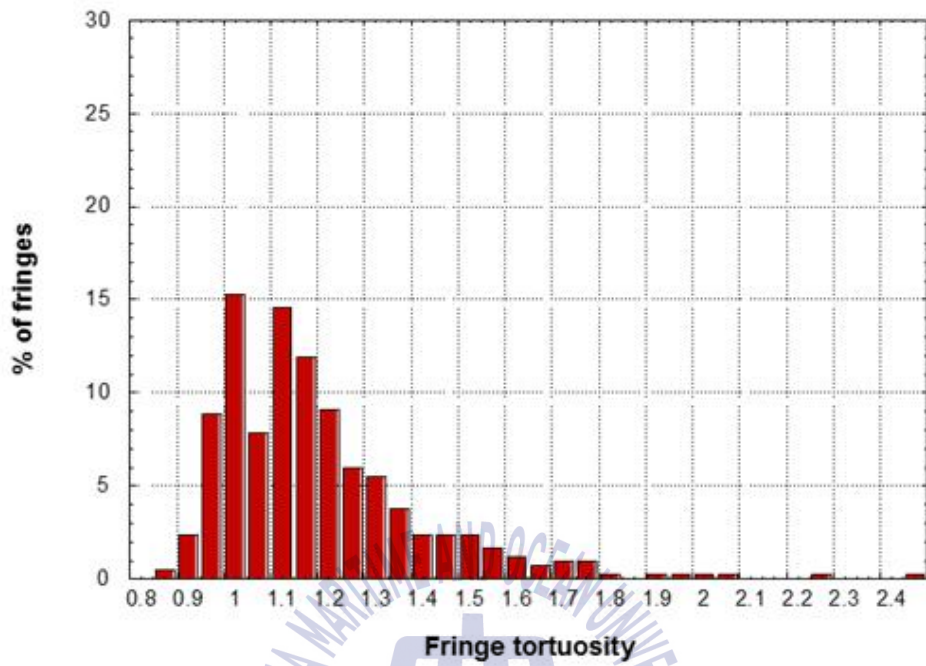
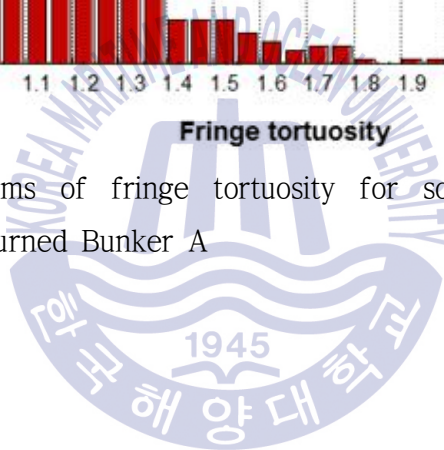


Fig. 4-9 Histograms of fringe tortuosity for soot collected from 2-stroke engine burned Bunker A



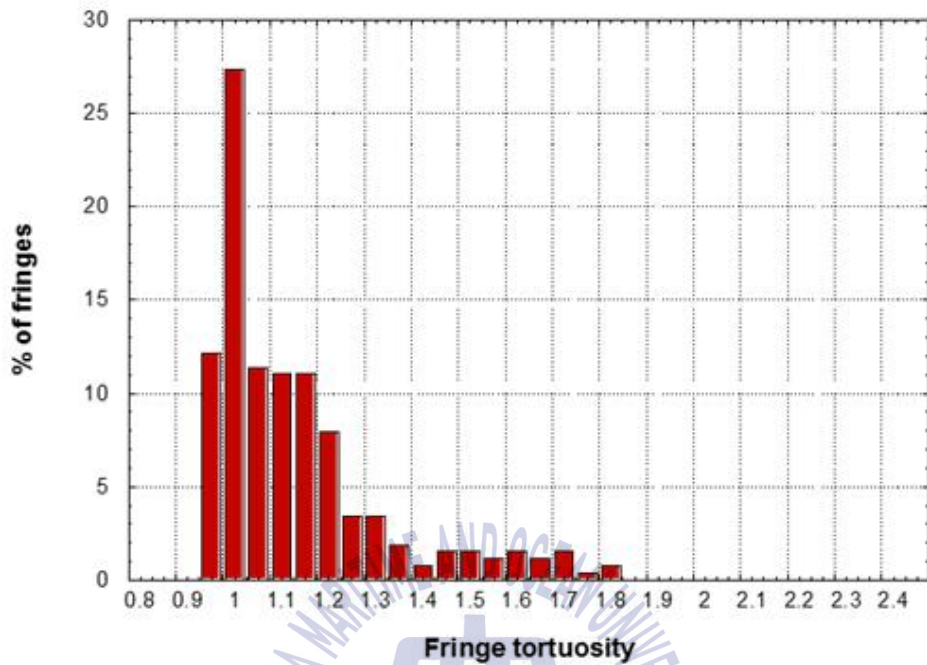
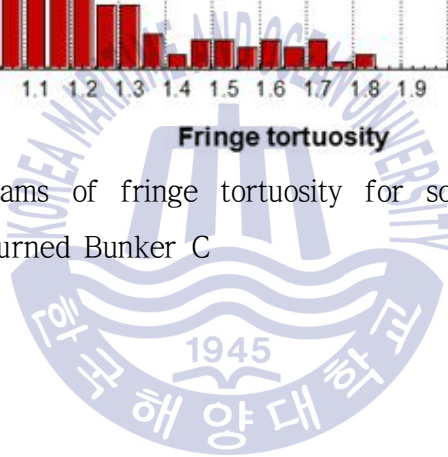


Fig. 4-10 Histograms of fringe tortuosity for soot collected from 4-stroke engine burned Bunker C



4.4 Conclusion

To investigate the influences of engine type and fuel on soot nanostructure, diesel soot particles were sampled from large bore 2-stroke engine burned Bunker A and 4-stroke engine burned Bunker C, respectively. And then, The soot particles collected were analyzed using Raman spectra and imaged using a HRTEM. Also, to quantitatively clarify the nanostructure of HRTEM images, the fringe length and tortuosity were measured using digital image process techniques. The soot nanostructures were significantly different from each other.

(1) The soot nanostructures are significantly different from each other. The HRTEM images indicate that the diesel soot from the 4-stroke engine burned Bunker C produced more small primary particles and higher degree of graphitic nanostructures than the 2-stroke engine burned Bunker A due to the increase of the exhaust gas temperature.

(2) The Raman spectroscopic analysis revealed that the G/D peak ratio of the diesel soot was increased in the 4-stroke engine burning Bunker C compared to the case of the 2-stroke engine burned Bunker A.

(3) Soot collected from the 2-stroke engine burned Bunker A (which produces lower exhaust gas temperature) was characterized by a higher degree of curvature of carbon lamellas. In contrast, the case of 4-stroke engine burned Bunker C (which produces higher exhaust gas temperature) produces the soot nanostructure that includes the extended carbon lamellas with very little observable curvature. The skeletonized fringes observed in the 4-stroke engine burned Bunker C case were largely planar, longer, and less tortuous while those observed in the 2-stroke engine burned Bunker A case are shorter and more curved.

(4) The experimental results clearly indicate that the higher temperature for the 4-stroke engine burned Bunker C case produces the graphitic nanostructures while the lower temperature for the 2-stroke engine burned Bunker A case produces the amorphous nanostructures. These experimental results highlight the importance of temperature on soot nanostructure.



Chapter 5. Application: Li-ion battery

5.1 Introduction

Maritime transport handles over 80 per cent of the volume of global trade and international shipping has been a fast growing sector of the global economy (Fuglestedt et al., 2009). Since 2000, annual growth rates in total seaborne trade have been higher than in the past and accordingly the world fleet has grown gradually over a decade (Eyring et al., 2010). With the growth of the world fleet, the fuel consumption has increased significantly during this period as the total installed power increased. Most of engines generate propulsion power from the combustion of low-quality residual fuels within the commercial shipping industry. The quantity of soot originating from the marine diesel engines is increasing due to the strong correlation between the world fleet fuel consumption and the total seaborne trade.

On the other hand, revised MARPOL (the International Convention for the Prevention of Pollution from Ships) Annex V regulations prohibit the discharge of all types of garbage including soot into the sea. However it is difficult for shipping company to dispose increasing garbage like soot and there is no clear solution to treat soot without landing with expense. The soot particles originating from the marine diesel engine (Clague et al., 1999) are emitted into the atmosphere with exhaust streams. However some of them adhere to the economizer's heat transfer surfaces, which reduce the efficiency of economizer, along with debilitating effects including increased cleaning costs, corrosion, and the risk of soot fire. It is difficult to estimate correct quantity of soot deposits adhered to the economizer because ocean going vessels are one of the largest uncontrolled sources of pollutants and the emission data from these sources are scarce (Agrawal et al., 2008). In the case of an

oceangoing Panamax container vessel, normally about 400liters/year of soot are collected by cleaning the economizer and then thrown away. Soot is mainly composed of carbon (>80wt.%) (Sadezky et al., 2005). It is generated during the high temperature pyrolysis or combustion process (Michaela et al., 2016; Sharma et al., 2016) and inherent in the operation of compression ignition engine (Tree & Svensson, 2007). None of studies, however, have yet tried to utilize the soot of which nanostructures show some degree of crystalline order (Vander & Tomasek, 2004). In this study, the attempt to recycle the waste soot as an active material for Li-ion battery was carried out for the first time, which is a quite unique way of thinking to utilize the waste rather for renewable energy. For this, the soot samples collected from a marine diesel engine of ocean going vessel were analyzed by X-ray diffraction (XRD), Raman spectroscopy and Brunauer-Emmett-Teller (BET) in order to investigate their characteristics of structure. Furthermore, Li-ion batteries were manufactured using the collected soot, and the performance test was conducted to verify the possibility of application as a Li-ion battery.

5.2 Fabrication of Li-ion battery

The smallest working unit in a battery is the electrochemical cell, consisting of a cathode and an anode separated and connected by an electrolyte. The electrolyte conducts ions but is an insulator to electrons. In a charged state, the anode contains a high concentration of intercalated lithium while the cathode is depleted of lithium. During the discharge, a lithium ion leaves the anode and migrates through the electrolyte to the cathode while its associated electron is collected by the current collector to be used to power an electric device. The reactions generated in each electrode is as followed;

Cathode; in case the active material is LiCoO_2

(charging)



(discharging)

Anode; in case the active material is graphite

(charging)



(discharging)

Total reaction

(charging)



(discharging)

A. Cathode Materials

State of the art cathode materials include lithium-metal oxides [such as LiCoO_2 , LiMn_2O_4 , and $\text{Li}(\text{NixMnyCoz})\text{O}_2$], vanadium oxides, olivines (such as LiFePO_4), and rechargeable lithium oxides. The characteristics of the materials are summarized in **Table 5-1**. Layered oxides containing cobalt and nickel are the most studied materials for lithium-ion batteries. They show a high stability in the high-voltage range but cobalt has limited availability in nature and is toxic, which is a tremendous drawback for mass manufacturing. Manganese offers a low-cost substitution with a high thermal threshold and excellent rate capabilities but limited cycling behavior. Therefore, mixtures of cobalt, nickel, and manganese are often used to combine the best properties and minimize the drawbacks. Vanadium oxides have a large capacity and excellent kinetics. However, due to lithium insertion and extraction, the material tends to become amorphous, which limits the cycling behavior. Olivines are nontoxic and have a moderate capacity with low fade due to cycling, but their conductivity is low. Methods of coating the material have been introduced that make up for the poor conductivity, but it adds some processing costs to the battery.

Table 5-1 Characteristics of the cathode materials

	LiCoO ₂	Li(Ni _{1/3} Co _{1/3} Mn _{1/3})O ₂	LiMn ₂ O ₄	LiFePO ₄
Structure	straitform	straitform	spinel	olivine
Theoretical capacity	274 mAh/g	285 mAh/g	148 mAh/g	170 mAh/g
Usable capacity	145 mAh/g	170 mAh/g	120 mAh/g	150 mAh/g
Usable voltage (Li/Li+vs.)	3.7 V	3.6 V	4.1 V	3.4 V
Advantage	<ul style="list-style-type: none"> • high electrical conductivity • easy compose 	<ul style="list-style-type: none"> • high capacity • low cost • thermal stability 	<ul style="list-style-type: none"> • low cost • non-toxic 	<ul style="list-style-type: none"> • thermal stability • low cost • non-toxic
Drawback	<ul style="list-style-type: none"> • high cost, toxic • thermal unstability 	<ul style="list-style-type: none"> • hard compose 	<ul style="list-style-type: none"> • Mn elution • low discharging capacity 	<ul style="list-style-type: none"> • low electrical conductivity • low energy density

B. Anode Materials

Anode materials are lithium, graphite, lithium-alloying materials, intermetallics, or silicon. Lithium seems to be the most straight forward material but shows problems with cycling behavior and dendritic growth, which creates short circuits. Carbonaceous anodes are the most utilized anodic

material due to their low cost and availability. However, the theoretical capacity (372 mAh/g) is poor compared with the charge density of lithium (3,862 mAh/g). Some efforts with novel graphite varieties and carbon nanotubes have tried to increase the capacity but have come with the price of high processing costs. Alloy anodes and intermetallic compounds have high capacities but also show a dramatic volume change, resulting in poor cycling behavior. Efforts have been made to overcome the volume change by using nanocrystalline materials and by having the alloy phase (with Al, Bi, Mg, Sb, Sn, Zn, and others) in a nonalloying stabilization matrix (with Co, Cu, Fe, or Ni).

C. Electrolytes

A safe and long-lasting battery needs a robust electrolyte that can withstand existing voltage and high temperatures and that has a long shelf life while offering a high mobility for lithium ions. Types include liquid, polymer, and solid-state electrolytes. The most important consideration is their flammability; the best performing solvents have low boiling points and have flash points around 30°C. Therefore, venting or explosion of the cell and subsequently the battery pose a danger. Electrolyte decomposition and highly exothermic side reactions in lithium-ion batteries can create an effect known as “thermal runaway.” Thus, selection of an electrolyte often involves a tradeoff between flammability and electrochemical performance.

D. Separators

As its name suggests, the battery separator separates the two electrodes physically from each other, thus avoiding a short circuit. In the case of a liquid electrolyte, the separator is a foam material that is soaked with the

electrolyte and holds it in place. It needs to be an electronic insulator while having minimal electrolyte resistance, maximum mechanical stability, and chemical resistance to degradation in the highly electrochemically active environment. In addition, the separator often has a safety feature, called “thermal shutdown” at elevated temperatures, it melts or closes its pores to shut down the lithium-ion transport without losing its mechanical stability. Separators are either synthesized in sheets and assembled with the electrodes or deposited onto one electrode in situ.

E. Binder

The binder settles active material powder and conducting agent powder to fix them on the current collector. The binder is insulator and keeps constructure of the electrode. Generally, polymer materials are used for binder such as polyvinylidene difluoride (PVDF). The characteristics required for the binder is as followed;

- Binding strength without being melted by electrolytes
- Appropriate viscosity and dispersibility
- High thermal resistance
- High oxidation resistance

F. Conducting agent

The conducting agent is fine carbon powder which is used for increasing the degree of the electronic conduction by developing conducting channel in the compound electrode. **Table 5-2** listed characteristics of the conducting agents. Presently, the carbon black is used for the conducting agent broadly.

Table 5-2 Characteristics of the conducting agents

	Strength	Weakness
Carbon black	- low cost - high conductivity	- process disadvantage
VGCF	- high conductivity	- high cost
Graphite fine powder	- process advantage	- quantity requirement

G. Current collector

As manufacturing the electrode plate, the slurry is pasted on the metal foil that is called as a current collector. The current collector transfers the electron to outside or accepts the electron from the active material as a role of the pathway. Aluminum is used for the cathode and copper is used for the anode as a current collector of Li-ion batteries as shown in Fig. 5-1.

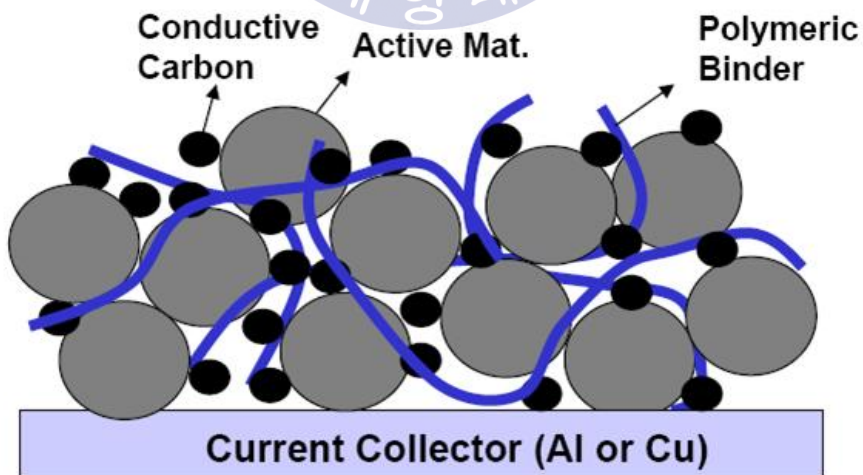


Fig. 5-1 Current collector

5.3 Performance test result

Performance test is usually carried out banks of cells using multi channel testers which can create different charge and discharge profiles as shown in Fig. 5-2.

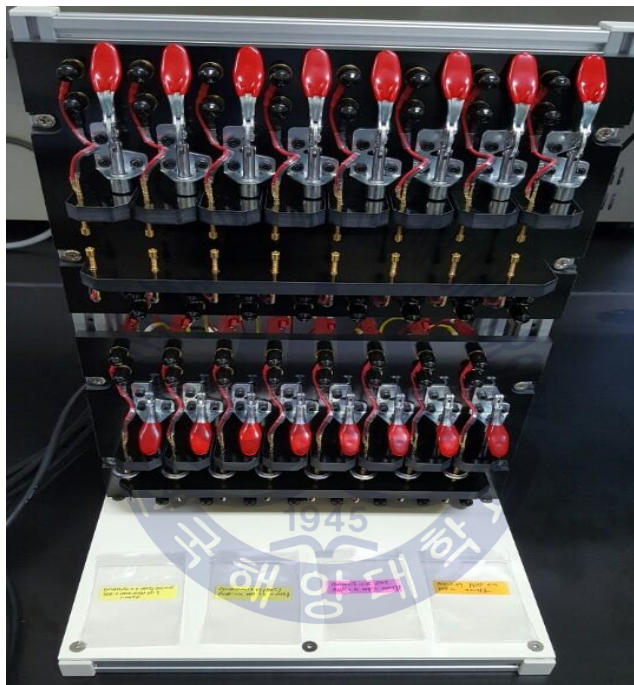


Fig. 5-2 Electrical performance test equipment

The battery cells manufactured using the soot deposits from main propulsion engine (2-stroke diesel engine burned bunker B) of T/S HANBADA were tested to investigate the electrical performance. Fig. 5-3 shows charge and discharge curves for the cycled cell at different C rates. The battery's potential is plotted versus capacity. The term C rate describes how fast a battery is charged or discharged.

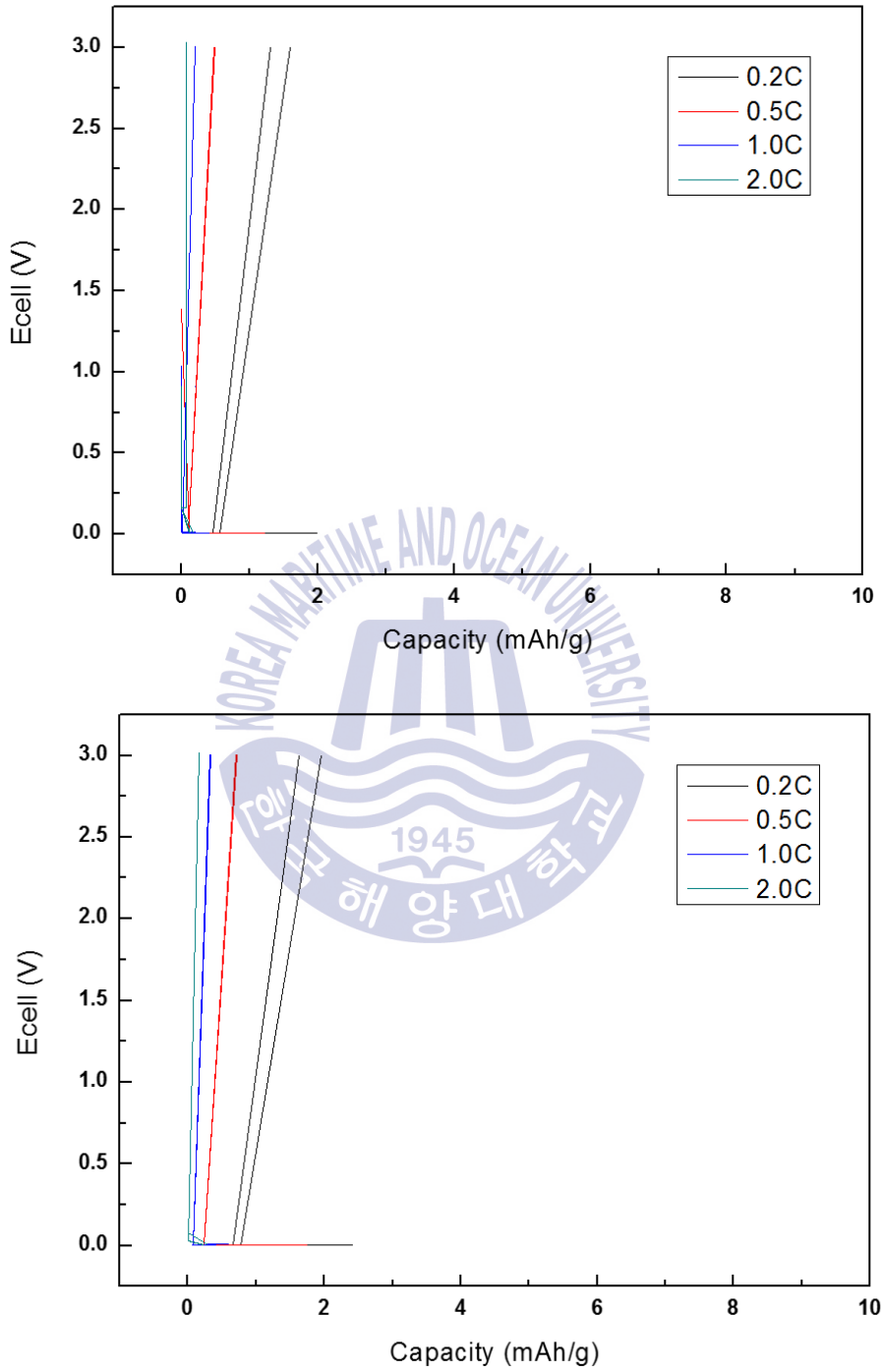


Fig. 5-3 Charge-discharge curves for the cyclized cells at different C rates

The result shows that the capacity of the cells is too low as an Li-ion battery. So, we annealed the soot deposits in the electrical furnace charged with nitrogen gas (see in Fig. 5-4) at 600°C and 900°C respectively to remove impurities in the soot. And then, the battery cells manufactured again using the annealed soot deposits were tested to investigate the electrical performance. Fig. 5-5, 5-6 show charge and discharge curves for the cycled cells using the soot deposits annealed at 600°C, 900°C. The performance curves for Li-ion cells below show that the more effective capacity of the cell is confirmed if the soot deposits are annealed at higher temperature.



Fig. 5-4 Graphitization furnace

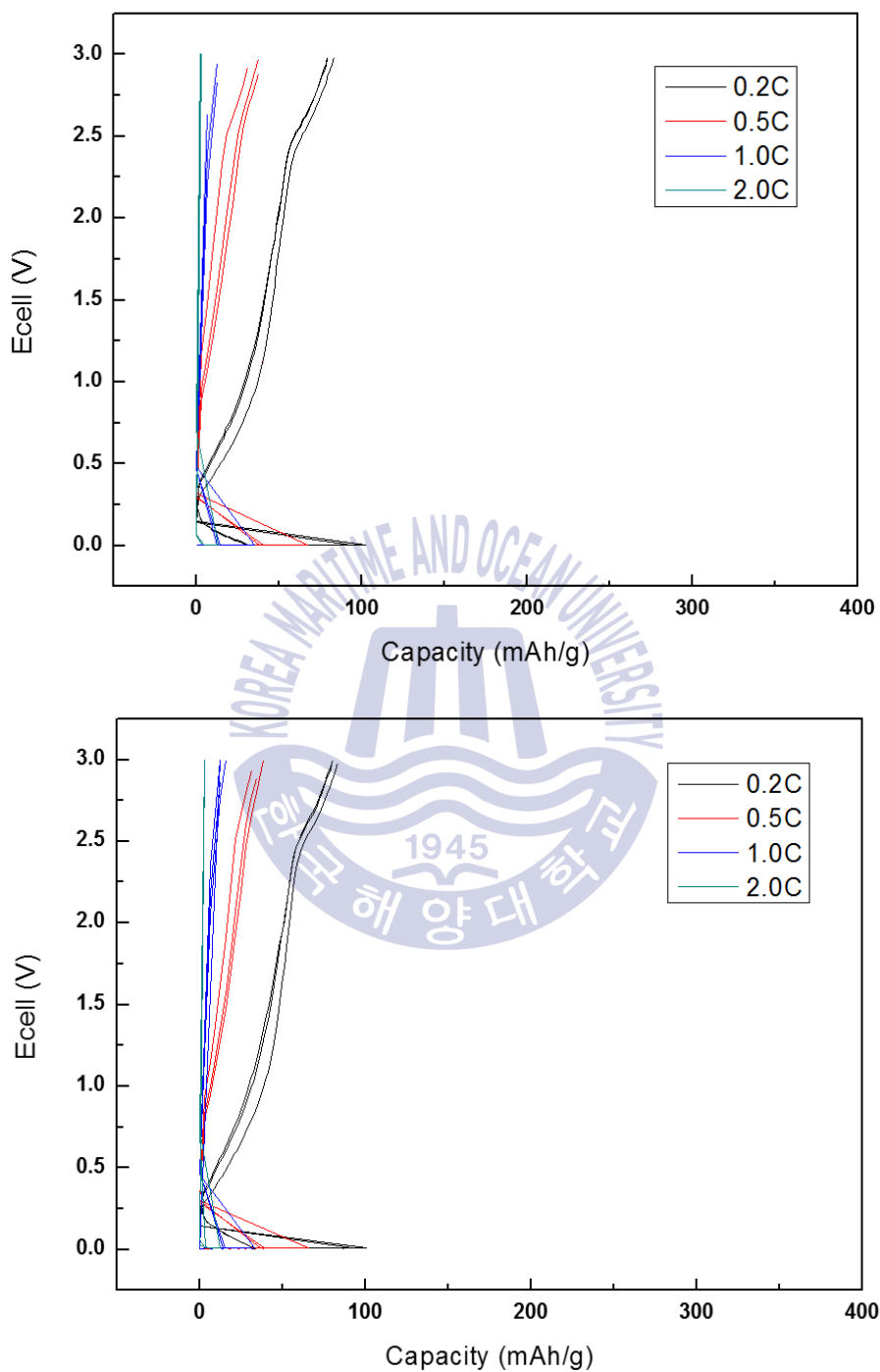


Fig. 5-5 Charge-discharge curves for the cyclized cells using soot deposits annealed at 600°C

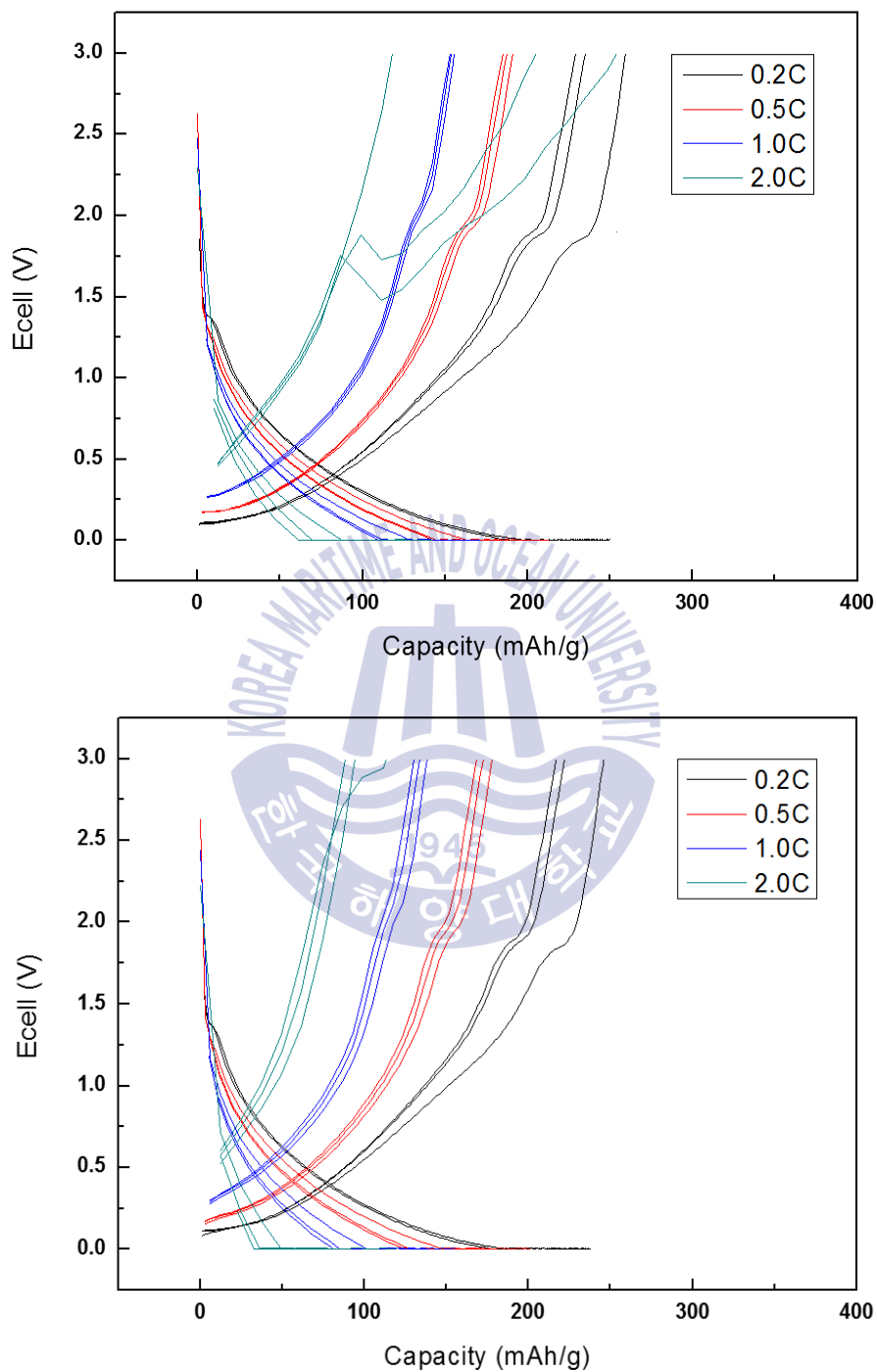


Fig. 5-6 Charge-discharge curves for the cyclized cells using soot deposits annealed at 900°C

Through the first cycle of charging and discharging of each battery cell, the coulomb efficiency by heat treatment temperature was confirmed. As a result (see in Fig. 5-7, 5-8, 5-9), the coulombic efficiency was higher as the heat treatment temperature of the soot was higher. That is, the ratio of lithium ions consumed to form the SEI layer is lower and the ratio of lithium ions used for actual charge and discharge is higher. The SEI layer grows during the initial charge and discharge cycles to stabilize at a certain thickness eventually, making the graphite surface passive to further reactions.

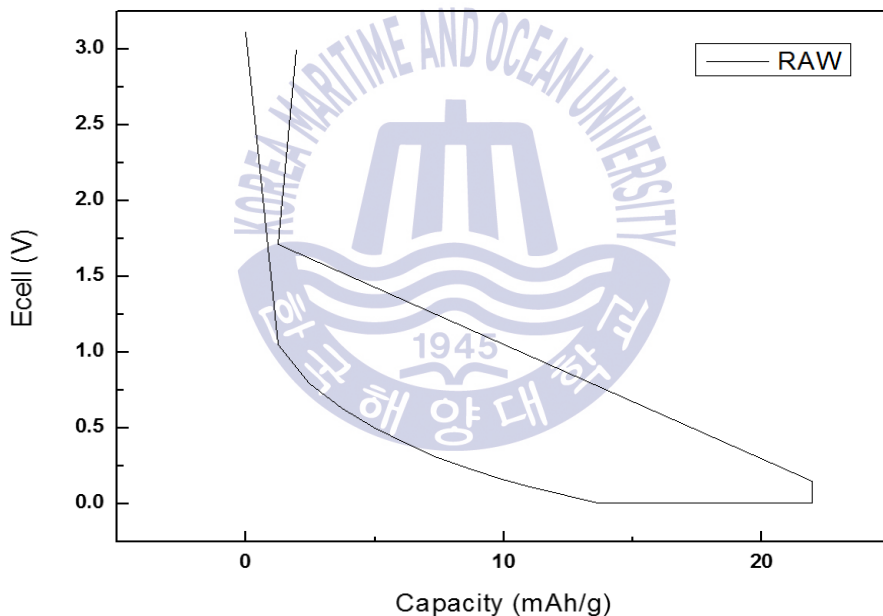


Fig. 5-7 Charge-discharge curve for the first cycle of the cell using raw soot deposits

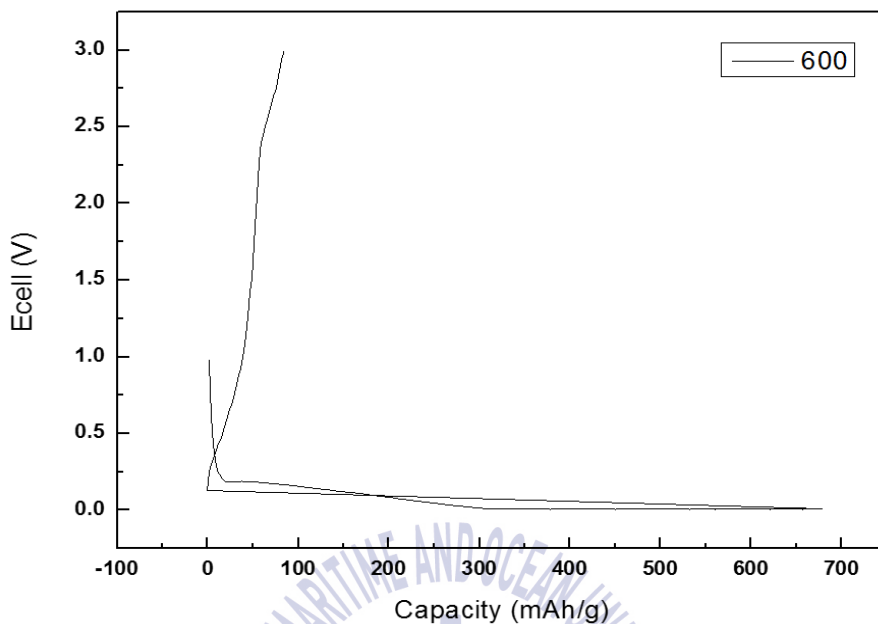


Fig. 5-8 Charge-discharge curve for the first cycle of the cell using soot deposits annealed at 600°C

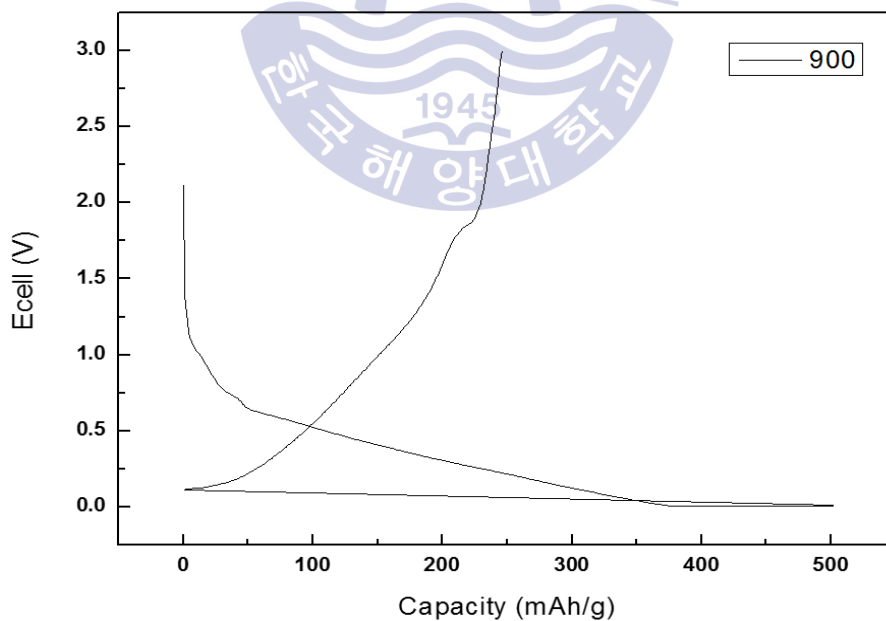


Fig. 5-9 Charge-discharge curves for the first cycle of the cell using soot deposits annealed at 900°C

5.4 Conclusion

The possibility of utilizing soot deposits as an anode active material for Li-ion batteries was verified in this study.

The most common anode active material used in Li-ion batteries is graphite. Considering the facts that the soot produced by marine diesel engines is mostly composed of carbon and has a graphite nanostructure, a lithium ion battery cell was manufactured using this soot as an anode active material.

In order to improve the performance of the battery, the batteries were manufactured by heating the soot (anode active material) until 600°C and 900°C respectively, so that the lithium ions could be inserted into the graphite layer more efficiently.

As the heat treatment temperature of the soot was increased, not only the charge-discharge capacity of the battery was increased but also the coulomb efficiency was increased. As a result, the heat treatment made the soot more graphitic so that the structure of the anode active material could be more intercalated and deintercalated.

Chapter 6. Summary

International shipping contributes significantly to emissions from the transportation sector, thereby affecting the chemical composition of the atmosphere, climate and regional air quality, and health. Key compounds emitted from ships are sulfur and nitrogen oxides and particulate matter as well as greenhouse gases such as carbon dioxide. Recent studies have shown that particulate matter from diesel engines could have a large impact on the Earth's radiation budget, particularly by altering the albedo of the polar area. However, few of the engine studies that have reported emissions data from slow-speed marine diesel engines and medium-speed marine diesel engines have been performed on actual shipboard engines.

This study presents results of the analysis of the soot from 2-stroke and 4-stroke marine diesel engines investigated at various sampling locations, engine speeds and bunker fuels. From a forensic point of view, detailed knowledge about the size, shape, and structure of diesel soot is important to understand the impact of the particles on the human body, and to enable more meaningful source assignments. From a marine engineering point of view, such information may also be useful for understanding the interaction of diesel soot particles with the engines and pollution abatement devices.

This thesis presents some results of our recent efforts not only to characterize the morphologic and molecular structure of diesel soot by means of Raman spectroscopy and high-resolution transmission electron microscopy, but also to utilize the soot as a source of renewable energy.

Chapter 3 describes the influence of sampling location and engine speed on nanostructures of diesel soot. Sampling was conducted at four points

from the turbocharger exit to the economizer exit at engine speeds of 120 rpm and 160 rpm. The experimental measurements revealed that variations in the sampling location led to a significant change in characteristics of the soot. The distinctive contrast between individual spherical particles becomes weaker, indicating that the particles tend to scatter more light. It would be conjectured that the radiative properties of collected particles tend to evolve from those of black bodies toward those of gray bodies as the sampling location moves downstream. This can be attributed to the dominance of PAH formation and condensation (relative to the decomposition of PAH) at lower temperatures leading to disordered graphitic structure, i.e., amorphous structure. The more curved graphitic structure observed in the sample collected downstream therefore indicates the abundance of amorphous structures with SP^3 bonds that formed through the cooling process in the ECO. The Raman spectra of soot samples revealed that variations in engine speeds influenced the BC/OC ratio. Two distinct (G and D) peaks are observed for both engine speeds, indicating the presence of graphitic and amorphous structures. The average G/D peak intensity ratio for the samples collected at 120 rpm is 1.49 while that for samples collected at 160 rpm increases to 1.69, indicating a higher degree of graphitization compared to the samples collected at the lower speed. A higher RPM can produce stronger combustion intensity, leading to higher combustion temperature. The HRTEM images exhibit a distinct qualitative change before and after the economizer, in that wrinkled non-planar graphitic structures are found more frequently after the economizer.

Chapter 4 describes the influence of engine type and fuel quality on nanostructures of diesel soot properties, based on experiments conducted on 2-stroke and 4-stroke engines burning different bunker fuels. The

experimental measurements showed that more small primary particles were generated from 4-stroke engines burning Bunker C than 2-stroke engines burning Bunker A with increasing exhaust gas temperature. The results clearly indicate that the higher temperature of exhaust gas for the 4-stroke engine burned Bunker C case produces more graphitic nanostructures while the lower temperature for the 2-stroke engine burned Bunker A case produces more amorphous nanostructures of primary particles. Soot nanostructure was analyzed by measuring the structural characteristics of carbon lamellae, using digital image processing techniques, the structural characteristics of a fringe are described in terms of the fringe length and tortuosity. The results showed that the 4-stroke engine burning Bunker C produced longer carbon lamellae with little degree of curvature.

Chapter 5 describes an attempt to recycle diesel soot particles as an anode active material for Li-ion battery, which is a unique use of waste to support renewable energy. Raman spectra analyses and HRTEM images were also used as part of this investigation. Samples of the soot were annealed at 600 and 900 °C, and Li-ion batteries were then manufactured using the collected and annealed samples, and performance tests conducted. The performance tests revealed that Li-ion batteries manufactured with the soot deposits have performance similar to that of conventionally manufactured batteries. Batteries manufactured with soot anodes annealed at 900 °C showed the best electric performance. Currently, the anode active material of Li-ion batteries produced in Korea depends on imports, mainly Chinese natural resources and processed materials from Japan. In addition, shipping companies pay a large amount of money to dispose of the soot generated from the economizer and the scavenging manifold of their ships' main engine. A process developing the

use of this waste as a resource to support renewable energy would be a very beneficial change.



References

- ACIA, 2004. *Impacts of a Warming Arctic: Arctic Climate Impact Assessment*, Cambridge University Press.
- Agrawal, H., Malloy, Q., Welch, W., Miller, J.D., 2008. In-use gaseous and particulate matter emissions from a modern ocean going container vessel, *Atmos. Environ*, 42, pp.5504–5510.
- American-Bureau-of-Shipping, 2001. *Notes on Heavy Fuel Oil*, <http://www.eagle.org/eagleExternalPortalWEB/ShowProperty/BEARepository/News&Events/Publications/ABSInternationalDirectory>.
- Arana, C.P., Pontoni, M., Sen, S. and Puri, I.K., 2004. Field Measurements of Soot Volume Fractions in Laminar Partially Premixed Coflow Ethylene/Air Flames. *Combust. Flame*, 138, pp.362.
- Arctic Council, 2011. *An assessment of emissions and mitigation options for black carbon for the arctic council*, Greenland: Arctic Council.
- Barone, A.C., A.D. Alessio, A.D. Anna, 2003. Morphological characterization of the early process of soot formation by atomic force microscopy, *Combust. Flame*, 132, pp.181–187.
- Bockhorn, H. and T. Schafer, 1994. *Soot formation in combustion*, Springer-Verlag: Berlin Heidelberg.
- Bockhorn, H., 1994. *A Short Introduction to the Problem - Structure of the Following Parts. Soot Formation in Combustion (Bockhorn H.(eds.))*, Springer-Verlag: Berlin Heidelberg.
- Bond, T.C., Streets, D.G., Yarber, K.F., Nelson, S.M., Woo, J.H., Klimont, Z.A., 2004. Technology-based global inventory of black and organic carbon

- emissions from combustion, *J. Geophys. Res.*, 109, pp.14203.
- Braun, A., F.E. Huggins, S. Seifert, J. Ilavsky, N. Shah, K.E. Kelly, et al., 2004. Size-range analysis of diesel soot with ultra-small angle X-ray scattering, *Combust. Flame*, 137, pp.63-72.
- Braun, A., N. Shah, F.E. Huggins, K.E. Kelly, A. Sarofim, C. Jacobsen, S. Wirick, H. Francis, J. Ilavsky, G.E. Thomas, G.P. Huffman, 2005. X-ray scattering and spectroscopy studies on diesel soot from oxygenated fuel under various engine load conditions, *Carbon*, 43, pp.2588-2599.
- Burtscher, H., 2005. Physical characterization of particulate emissions from diesel engines: a review, *Journal of Aerosol Science*, 36(7), pp.896-932.
- Charalampopoulos, T.T., and Chang, H., 1991. Agglomerate Parameters and Fractal Dimension of Soot Using Light Scattering Effects on Surface Growth *Combust. Flame.*, 87, pp.89.
- Chen, P., F. Huang, S. Yun, 2006. Optical characterization of nanocarbon phases in detonation soot and shocked graphite, *Diam. Relat. Mater*, 15, pp.1400-1404.
- Choi, J.H., Cho, I.S., Lee, J.S., Park, S.K., Lee, W.J., Kim, H., Chang, H.J., Kim, J.Y., Jeong.S., Park, S.H., 2016. Characterization of carbonaceous particulate matter emitted from marine diesel engine, *Journal of Mechanical Science and Technology*, 30(5), pp.2011-2017
- Choi, S.C., 2009. *Measurement and Analysis of the Dimensionless Extinction Constant for Diesel and Biodiesel Soot: Influence of Pressure, Wavelength and Fuel Type*. ph.D. Drexel University.
- Chow, J.C., Watson, J.G., Crow, D., Lowenthal, D.H., Merrifield, T., 2001. Comparison of IMPROVE and NIOSH carbon measurements. *Aerosol Sci Technol*, 34(1), pp.23-34.

- Ciambelli, P., Palma, V., Russo, P., Vaccaro, S., 2002. Deep filtration and catalytic oxidation: an effective way for soot removal, *Catal Today*, 73(3-4), pp.363-70.
- Clague, A.D.H., Donnet, J.B., Wang, T.K. and Peng, J.C.M., 1999. A comparison of diesel engine soot with carbon black, *Carbon*, 37, pp.1553-1565.
- Corbett, J.J., et al. 2007. Mortality from ship emissions: A global assessment, *Environ. Sci. Technol.*, 41, pp.8512-8518.
- Corbett, J.J., Fischbeck, P.S., 1997. Emissions from ships. *Science*, 278(5339), pp.823-824.
- Corbett, J.J., Lack, D.A., Winebrake, J.J., Harder, S., Silberman, J.A., and Gold, M., 2010. Arctic Shipping Emissions Inventories and Future Scenarios, *Atmos. Chem. Phys.*, 10, pp.9689-9704.
- Dalzell, W.H., and Sarofim, A.F., 1969. Optical constants of soot and their application to heat-flux calculations, *Transaction of the ASME: Journal of Heat Transfer*, 91, pp.100.
- Dobbins, R.A., and Megaridis, C.M., 1987. Morphology of Flame-Generated Soot as Determined by Thermophoretic Sampling, *Langmuir*, 3, pp.254.
- Endresen, O., Sorgard, E., Behrens, H.L., Brett, P.O. and Isaksen I.S.A., 2007. A historical reconstruction of ships' fuel consumption and emissions, *J. Geophys. Res.*, 112, D12301, doi:10.1029/2006JD007630.
- Escribano, R., J.J. Sloan, N. Siddique, N. Sze, T. Dudev, 2001. Raman spectroscopy of carbon-containing particles, *Vib. Spectrosc.* 26, pp.179-186.
- Eyring, V., Isaksen, I.S.A., Berntsen, T., Collins, W.J., Corbett, J.J., Endresen, O., Grainger, R.G., Moldanova, J., Schlager, H., Stevenson, D.S., 2010. Transport impacts on atmosphere and climate: Shipping, *Atmos. Environ.* 44, pp.4735-4771.

- Eyring, V., Kohler, H.W., Van Aardenne, J., Lauer, A., 2005. Emissions from international shipping: 1. The last 50 years. *J. Geophys.* 110, D17305. doi:10.1029/2004JD005619.
- Eyring, V., Stevenson, D.S., Lauer, A., Dentener, F.J., Butler, T., Collins, W.J., Ellingsen, K., Gauss, M., Hauglustaine, D.A., Isaksen, I.S.A., Lawrence, M.G., Richter, A., Rodriguez, J.M., Sanderson, Strahan, M.S.E., Sudo, K., Szopa, S., Van Noije, T.P.C., Wild, O., 2007. Multi-model simulations of the impact of international shipping on atmospheric chemistry and climate in 2000 and 2030. *Atmos. Chem. Phys.* 7, pp.757–780.
- Ferrari, A.C. and J. Robertson, 2004. Raman spectroscopy of amorphous, nanostructured, diamond-like carbon, and nanodiamond, *Phil. Trans. R. Soc. Lon. A.*, 362, pp.2477–2512.
- Flanner, M.G., Zender, C.S., Randerson, J.T. and Rasch, P.J., 2007. Present-day climate forcing and response from black carbon in snow, *Journal of Geophysical Research*, 112(D11202): doi:10.1029/2006JD008003.
- Frenklach, M. and Wang, H., 1991. Detailed modeling of soot particle nucleation and growth, *Proc. Combust. Inst.*, 23, pp.1559–1566.
- Frenklach, M., 2002. Reaction mechanism of soot formation in flames, *Phys. Chem. Chem. Phys.*, 4, pp.2028–2037.
- Fuglestedt, J., Bernsten, T., Eyring, V., Isaksen, I., Lee, D.S., Sausen, R., 2009. Shipping Emissions: From Cooling to Warming of Climate—and Reducing Impacts on Health, *Environ. Sci. Technol.*, 43, pp.9057–9062.
- Fung, K., Chow, J.C., Watson, J.G., 2002. Evaluation of OC/EC speciation by thermal manganese dioxide oxidation and the IMPROVE method. *J Air Waste Manage Assoc*, 52(11), pp.1333–41.
- Galvez, A., Herlin-Boime, N., Reynaud, C., Clinard, C. and Rouzaud, J., 2002.

- Carbon Nanoparticles from Laser Pyrolysis, *Carbon*, 40, pp.2775.
- Garderet, R. and Emmett, D.W., 2009. *Integrating black carbon into climate change agreements: The need, challenges and practical first steps*, Inno energy solutions group, lic.
- Goel, A., Hebgen, P., Vander, J.B. and Howard, J.B., 2002. Combustion Synthesis of Fullerenes and Fullerenic Nanostructures, *Carbon*, 40, pp.177.
- Granier, C., U. Niemeier, J.H. Jungclaus, L. Emmons, P. Hess, J.F. Lamarque, S. Walters, and G.P. Brasseur, 2006. Ozone pollution from future ship traffic in the Arctic northern passages, *Geophys. Res. Lett.*, 33, L13807, doi:10.1029/2006GL026180.
- Grieco, W.J., J.B. Howard, L.C. Rainey, J.B. Vander Sande, 2000. Fullerenic carbon in combustion-generated soot, *Carbon*, 38, pp.597-614.
- Hansen and Nazarenko, 2004. Soot Climate Forcing via Snow and Ice Albedos. *Proc. Natl. Acad. Sci*, 101, pp.423.
- Harshit, A., Quentin, G.J., Malloya, William, A., Welchb, J., Wayne, M., David, R., Cocker, 2008. In-use gaseous and particulate matter emissions from a modern ocean going container vessel, *Atmospheric Environment*, 42, pp.5504-5510.
- Haynes, B.S. and Wagner, H.G., 1981. Soot formation, *Prog Energy Combust Sci.*, 7(4), pp.229-273.
- Heywood, J.B., 1988. *Internal Combustion Engine Fundamentals*. McGraw-Hill; New York.
- International Maritime Organization (IMO), 1997. *Technical Code on Control of Emission of Nitrogen Oxides from Marine Diesel Engines (NOx Technical Code)*, London; IMO.
- International Maritime Organization (IMO), 1998. *Regulations for the prevention*

of air pollution from ships and NO_x technical code, ANNEX VI of MARPOL 73/78, London; IMO.

International Maritime Organization (IMO), 2009. *Second IMO Greenhouse Study*, http://www.imo.org/blast/blastDataHelper.asp?data_id=27795&filename=GHGStudyFINAL.pdf.

International Maritime Organization (IMO), 2010a. *Air Pollution from Ships Cut with Entry Into Force of MARPOL Amendments*, http://www.imo.org/newsroom/mainframe.asp?topic_id=1859&doc_id=13309.

International Maritime Organization (IMO), 2010b. *Emissions inventory and analysis of impacts of short-lived climate forcing aerosols from international shipping activity in the Arctic, 15th Session of the Bulk Liquids and Gases Sub-Committee of the International Maritime Organisation*, London, UK,

International Maritime Organization (IMO), 2011a. *Amendments to the Annex of the Protocol of 1997 to Amend the International Convention for the Prevention of Pollution from Ships, 1973, as Modified by the Protocol of 1978 Relating Thereto (Inclusion of regulations on energy efficiency for ships in MARPOL Annex VI)*. Resolution MEPC.203(62). [http://www.imo.org/MediaCentre/HotTopics/GHG/Documents/eediamendments RESOLUTION MEPC203 62.pdf](http://www.imo.org/MediaCentre/HotTopics/GHG/Documents/eediamendments%20RESOLUTION%20MEPC203%2062.pdf)

International Maritime Organization (IMO), 2011b. *Report of the Marine Environment Protection Committee on its Sixty-Second Session, MEPC 62/24*, <http://docs.imo.org/Shared/Download.aspx?did=68320>.

IPCC, 2007. *Climate Change 2007: The Physical Science Basis. Contribution of Working group 1 to the Fourth Assessment Report. Report of the Intergovernmental Panel on Climate Change*, S. Solomon, D. Qin, M. Manning et al., Cambridge, United Kingdom and New York, NY USA; Cambridge University Press.

- Ishiguro, T., Y. Takatori, K. Akihama, 1997. Microstructure of diesel soot particles probed by electron microscopy: first observation of inner core and outer shell, *Combust. Flame*, 108, pp.231-234.
- Jacobson, M.Z., 2001. Strong Radiative Heating due to the Mixing State of Black Carbon in Atmospheric Aerosols, *Nature*, 409, pp.695.
- Jensen, K.A., Suo-Anttila, J.M., Blevins, L.G., 2007. Measurement of Soot Morphology, Chemistry, and Optical Properties in the Visible and Near-Infrared Spectrum in the Flame Zone and Overfire Region of Large JP-8 Pool Fires, *Comust. Sci. and Tech*, 179, pp.2453.
- Kasper, A., S. Aufdenblatten, A. Forss, M. Mohr, and H. Burtscher, 2007. Particulate Emissions from a Low-Speed Marine Diesel Engine, *Aerosol Science and Technology*, 41(1), pp.24-32.
- Kennedy, I.M., 1997. Model of Soot Formation and Oxidation, *Prog. Energy Combust. Sci.*, 23, pp.95.
- Kittelson D.B., 1998. Engines and particles: a review, *J Aerosol Sci*, 29(5-6), pp.575-88.
- Kondo, Y., Matsui, H., Moteki, N., Sahu, L., Takegawa, N., Kajino, M., Zhao, Y., Cubison, M.J., Jimenez, J.L., Vay, S., Diskin, G.S., Anderson, B., Wisthaler, A., Mikoviny, T., Fuelberg, H.E., Blake, D.R., Huey, G., Weinheimer, A.J., Knapp, D.J. and Brune, W.H., 2011. Emissions of black carbon, organic, and inorganic aerosols from biomass burning in North America and Asia in 2008, *J. Geophys. Res*, 116(D8): D08204 10.1029/2010jd015152.
- Koylu, U.O., and Faeth, G.M., 1992. Structure of overfire soot in Buoyant Turbulent diffusion flames at long residence times, *Combust. Flame.*, 89, pp.140.
- Koylu, U.O., Faeth, G.M., Farias, T.L., Carvalho, M.G., 1995. Fractal and

- projected structure properties of soot aggregates, *Combust. Flame.*, 100, pp.621.
- Lack, D. A. and J. J. Corbett., 2012. Black carbon from ships: a review of the effects of ship speed, fuel quality and exhaust gas scrubbing, *Atmos. Chem. Phys.*, 12, pp.3985-4000.
- Lack, D.A., Cappa, C.D., Langridge, J., Bahreini, R., Buffaloe, G., Brock, C., Cerully, K., Coffman, D., Hayden, K., Holloway, J., et al., 2011. Impact of Fuel Quality Regulation and Speed Reductions on Shipping Emissions: Implications for Climate and Air Quality, *Environ. Sci. Technol.*, 45, pp.9052-9060.
- Lack, D.A., Corbett, J.J., Onasch, T.B., Lerner, B., Massoli, P., Quinn, P.K., Bates, T.S., Covert, D., Coffman, D.J., Sierau, B., et al., 2009. Particulate Emissions from Commercial Shipping. Chemical, Physical and Optical Properties, *J. Geophys. Res.*, 114, D00F04, doi:10.1029/2008/JD011300.
- Law, K. and Stohl, A., 2007. Arctic Air Pollution: Origins and Impacts, *Science*, 315, pp.1537.
- Lighty, J.S., Veranth, J.M., Sarofim, A.F., 2000. Introduction to the air and waste management associations 30th annual critical review. *J Air Waste Manage Assoc*, 50(9), pp.1565-618.
- Lloyd, A.C., Cackette, T.A., 2001. Diesel engines: environmental impact and control, *J Air Waste Manage Assoc*, 51(6), pp.809-47.
- MAN B&W Diesel, 2004. *Emission Control: MAN B&W Two-Stroke Diesel Engines*, Copenhagen; MAN B&W Diesel.
- McConnell, J.R., et al., 2007. 20th-century industrial black carbon emissions altered Arctic climate forcing, *Science*, 317, pp.1381- 1384.

- Michaela, N.E., Henrike, B., Wolfgang, M., Simone, I.S., Christian, Z., Sebastian, L., Dieter, B., Ulrich, N., Natalia, P.I. and Reinhard, N., 2016. Reactivity and structure of soot generated at varying biofuel content and engine operating parameter, *Combustion and Flame*, 163, pp.157-169.
- Mochizuki, M. and Forster, R.E., 1962. Diffusion of Carbon Monoxide through Thin Layers of Hemoglobin Solution, *Science*, 23, pp.897.
- Moss, J. B., Stewart, C.D., and Syed, K.J., 1988. Flowfield modelling of soot formation at elevated pressure, *Proc. Combust. Inst.*, 22, pp.413.
- Mulholland, G.W., and Choi, M.Y., 1998. Measurement of the Mass Specific Extinction Coefficient for Acetylene and Ethene Smoke Using the Large Agglomerate Optics Facility, *Proc. Combust. Inst.*, 27, pp.1515.
- Muller, J., 1984. Atmospheric residence time of carbonaceous particles and particulate PAH-compounds, *Sci. Total Environ.*, 36, pp.339-346.
- Mun, P., Nikolas, K., Honore, W., Jesper, S., 2016. Numerical investigation of soot formation and oxidation processes under large two-stroke marine diesel engine-like conditions using integrated CFD-chemical kinetics, *Applied Energy*, 169, pp.874-887.
- Ogren, J.A., P.J. Groblicki, and R.J. Charlson, 1984. Measurement of the removal rate of elemental carbon from the atmosphere, *Sci. Total Environ.*, 36, pp.329- 338.
- Ossler, F., J. Larsson, 2004. Exploring the formation of carbon-based molecules, clusters and particles in situ detection of scattered X-ray radiation, *Chem. Phys. Lett*, 387, pp.367-371.
- Palmer, H.B., and Cullis, C.F., 1965. The formation of carbon from gases. In Chemistry and physics of carbon, *Marcel Dekker; London (ed. Walker, P. L.)*, 1, pp.265.

- Palotas, A.B., Rainey, L.C., Feldermann, C.J., Sarofim, A.F., and Vander Sande, J.B., 1996. Soot Morphology: An Application of Image Analysis in High-resolution Transmission Electron Microscopy, *Microsc. Res. Tech*, 33, pp.266.
- Park, R.J., D.J. Jacob, M.Chin, and R.V. Martin, 2003. Sources of carbonaceous aerosols over the United States and implications for natural visibility, *J. Geophys. Res.*, 108(D12), pp.4355.
- Park, S. H., 2007. *Investigation of Sooting Behavior and Soot Nanostructures of Ethanol Droplet Flames in Microgravity*. ph.D. Drexel University.
- Park, S.H., M.Y. Choi, and A. Yozgatligil, 2009. Nanostructure of soot collected from ethanol droplet flames in microgravity, *Combust. Sci. Technol.*, 181(9), pp.1164-1186.
- Parungo, F., C. Nagamoto, M.-Y. Zhou, A. D. A. Hansen, and J. Harris (1994), Aeolian transport of aerosol black carbon from China to the ocean, *Atmos. Environ.*, 27, 3251- 3260.
- Peters, A., Dockery, D.W., Muller, J.E., and Mittleman, M.A., 2001. Increased Particulate Air Pollution and the Triggering of Myocardial Infarction, *Circulation*, 103, pp.2810.
- Pope, C.A. III, Burnett, R.T., Thun, M.J.,Calle, E.E., Krewski, D., and Ito, K., and Thurston, G.D., 2002. Lung Cancer, Cardiopulmonary Mortality, and Long-term Exposure to Fine Particulate Air Pollution, *JAMA*, 287, pp.1132.
- Popovitcheva, O. B., Persiantseva, N. M., Trukhin, M. E., Rulev, G. B., Shonija, N. K., Buriko, Y.Y., Starik, A.M., Demirdjian, B., Ferry, D. and Suzanne J., 2000. Experimental Characterization of Aircraft Combustor Soot : Microstructure, Surface Area, Porosity and Water Adsorption, *Phys. Chem. Chem. Phys*, 2, pp.4421.

- Poschl, U., 2003. Aerosol particle analysis: challenges and progress, *Anal Bioanal Chem*, 375(1), pp.30-2.
- Prado, G., J. Jagoda, K. Neoh, and J. Lahaye, 1981. A Study of Soot Formation in Premixed Propane/Oxygen Flames by In Situ Optical Techniques and Sampling Probes, *Proc. Combust. Inst.* 18, pp.1127.
- Quinn, P. K., Bates, T.S., Baum, E., Doubleday, N., Fiore, A.M., Flanner, M., Fridlind, A., Garrett, T.J., Koch, D., Menon, S., Shindell, D., Stohl, A., and Warren, S.G., 2008. Short-lived pollutants in the Arctic: their climate impact and possible mitigation strategies, *Atmos. Chem. Phys.*, 8, pp.1723-1735.
- Ramanathan, V. and Carmichael, G., 2008. Global and regional climate changes due to black carbon, *Nature Geoscience*, 1, pp.221-227.
- Rubio, M.A., Oyolab, P., Gramsch, E., Lissia, E., Pizarrod, J., and Villena, G., 2004. Ozone and Peroxyacetylnitrate in Downtown Santiago, Chile, *Atmospheric Environment*, 38, pp.4931.
- Sadezky, A., H. Muckenhuber, H. Grothe, R. Niessner, U. Poschl, 2005. Raman microspectroscopy of soot and related carbonaceous materials: spectral analysis and structural information, *Carbon*, 43, pp.1731-1742.
- Schlager, H., Pacyna, J., 2004. *International conventions on aviation, shipping and coastal pollution*; Chapter 4 of the GMES-GATO Strategy Report, European Commission Air Pollution Series No. 82, EUR 21154, ISBN: 92-894-4734-6.
- Schwarz, J.P., Gao, R.S., Spackman, J.R., Watts, L.A., Thomson, D.S., Fahey, D.W., Ryerson, T.B., Peischl, J., Holloway, J.S., Trainer, M., Frost, G.J., Baynard, T., Lack, D.A., de Gouw, J.A., Warneke, C. and Del Negro, L. A., 2008. Measurement of the Mixing State, Mass, and Optical Size of Individual Black Carbon Particles in Urban and Biomass Burning Emissions, *Geophys.*

Res. Lett, 35, 10.1029/2008gl033968.

Sedlacek, A.J., III, Lewis, E.R., Kleinman, L., Xu, J. and Zhang, Q., 2012. Determination of and evidence for non-core-shell structure of particles containing black carbon using the Single-Particle Soot Photometer (SP2), *Geophys. Res. Lett*, 39(6): L06802 10.1029/2012gl050905.

Serreze, M.C., Holland, M.M. and Stroeve, J., 2007. Perspectives on the Arctic's Shrinking Sea-Ice Cover, *Science*, 315(5818), pp.1533-1536.

Shaddix, C., Palotas, A., Megaridis, C., Choi, M.Y., Yang, N.Y., 2005. Soot graphitic order in laminar diffusion flames and a large-scale JP-8 pool fire, *International Journal of Heat and Mass Transfer*, 48, pp.3604-3614.

Sharma, H.N., Pahalagedara, L., Joshi, A., Suib, S.L., Mhadeshwar, A.B., 2012. Experimental Study of Carbon Black and Diesel Engine Soot Oxidation Kinetics Using Thermogravimetric Analysis, *Energy and Fuels*, 26(9-10), pp.5613-5625.

Sharma, V., Dairene, U., Arup, G., Ann, O., William, A.P., Alex, S., Monica, A.F., Pranesh, B.A., 2016. Structure and chemistry of crankcase and exhaust soot extracted from diesel engines, *Carbon*, 103, 327-338.

Shim, H.S., Hurt, R.H., and Yang, N.C., 2000. A Methodology for Analysis of 002 Lattice Fringe Images and Its Application to Combustion-derived Carbons, *Carbon*, 38, pp.29.

Shindell, D. and Faluvegi, G., 2009. Climate response to regional radiative forcing during the twentieth century, *Nature Geosci*, 2(4), pp.294-300.

Stasio, S.D., 2001. Electron microscopy evidence of aggregation under three different size scales for soot nanoparticles in flame, *Carbon*, 39, pp.109-118.

Stroeve, J., M.M. Holland, W. Meier, T. Scambos, and M. Serreze, 2007. Arctic sea ice decline: Faster than forecast, *Geophys. Res. Lett.*, 34, L09501,

doi:10.1029/2007GL029703.

Su, D.S., Jentoft, D.E., Muller, J.O., Jacob, E., Simpson, C.D., Tomovic, Z., et al., 2004. Microstructure and oxidation behaviour of Euro IV diesel engine soot: a comparative study with synthetic model soot substances, *Catalysis Today*, 90, pp.127-132.

Syed, K.J., Stewart, C.D., and Moss, J.B., 1990. Modeling soot formation and thermal radiation in buoyant turbulent diffusion flames, *Proc. Combust. Inst.*, 23, pp.1533.

The International Council on Combustion Engines (CIMAC), 2012. *Background information on black carbon emissions from large marine and stationary diesel engines – definition, measurement methods, emission factors and abatement technologies*, CIMAC.

Tree, D.R. and Svensson, K.I., 2007. Soot process in compression ignition engines, *Prog Energy Combust Sci.*, 33, pp.272-309.

United States Environmental Protection Agency (USEPA), 2012. *Report to congress on black carbon: Department of the interior, environment, and related agencies appropriations act*, USEPA.

Vander Wal, R.L. and A.J. Tomasek, 2004. Soot nanostructure: Dependence upon synthesis conditions, *Combust. Flame*, 136, pp.129-140.

Vander Wal, R.L. and Mueller, C.J., 2006. Initial Investigation of Effects of Fuel Oxygenation on Nanostructure of Soot from a Direct-Injection Diesel Engine, *Energy & Fuels*, 20, pp.2364.

Vander Wal, R.L., Tomasek, A.J., Street, K.H., David R. and Thompson, W.K., 2004. Carbon Nanostructure Examined by Lattice Fringe Analysis of High-Resolution Transmission Electron Microscopy Images, *Applied Spectroscopy*, 58, pp.230.

- Watson, J.G., J.C. Chow, and L.W. Antony Chen, 2005. Summary of organic and elemental carbon/black carbon analysis methods and intercomparisons, *Aerosol and Air Quality*, 5(1), pp.65–102.
- Wentzel, M., H. Gorzawski, K.H. Naumann, H. Saathoff, S. Weinbruch, 2003. Transmission electron microscopical and aerosol dynamical characterization of soot aerosols, *Aerosol Sci*, 34, pp.1347–1370.
- Williams, T.C., Shaddix, C.R., Jensen, K.A., Suo-Anttila, J.M., 2007. Measurement of the dimensionless extinction coefficient of soot within laminar diffusion flames, *Int. J. Heat Mass Transfer*, 50, pp.1616.
- Woodyard, D., 2004. *Pounder's Marine Diesel Engines and Gas Turbines*. 8th Ed. Elsevier: Burlington.
- Ying, Q., Fraser, M.P., Griffin, R.J., Chen, J., and Kleeman, M.J., 2007. Verification of a Source-Oriented Experimentally Mixed Air Quality Model During a Severe Photochemical Smog Episode, *Atmospheric Environment*, 41, pp.1521.
- Zhu, J.Y., 2002. *An Experimental Investigation of Soot Optical Properties in the Visible and Infrared Spectrums*, Ph.D. Chicago: University of Illinois.
- Zhu, J.Y., Choi, M.Y., Mulholland, G.W., Gritzo, L.A., 2000. Accurate Measurement of Soot Extinction in the Near-Infrared Spectrum, *Int. J. Heat Mass Transfer*, 43, pp.3299.
- Zhu, J.Y., Choi, M.Y., Mulholland, G.W., Manzello, S.L., Gritzo, L.A., Suo-Antilla, J.M., 2002. Measurement of visible and near-IR optical properties of soot produced from laminar flames, *Proc. Combust. Inst.*, 29, pp.2367.
- Zhu, W., D.E. Miser, W.G. Chan, M.R. Hajaligol, 2004. Characterization of combustion fullerene soot, C₆₀, and mixed fullerene, *Carbon*, 42, pp.1463–1471.

감사의 글

지난 학위 과정을 돌아보면 일과 학업, 두 마리 토끼를 놓치지 않으려고 무던히도 발버둥 쳤던 제 모습과 그 모습에 지지와 격려를 아끼지 않으시고 정말 많은 도움을 주신 분들이 주마등처럼 떠오릅니다. 그 분들의 도움을 받았기 때문에 지금 이 결실의 기쁨을 느낄 수 있는 것이라는 생각하며, 박사 논문을 마무리하면서 연구자로서의 걸음에 도움을 주신 여러분들께 감사의 마음을 전합니다.

먼저 부족한 저를 제자로 받아주시고 본 논문의 연구계획에서부터 완성에 이르기까지 학문적 기틀을 잡아주시고 소중한 가르침과 조언을 주신 존경하는 최재혁 교수님께 깊은 감사를 드립니다. 연구뿐만이 아니라 제 일상의 소소한 어려움부터 큰 무게의 걱정까지 함께 고민해주시고 지친 저에게 항상 긍정의 에너지를 불어 넣어주신 덕분에 학업과 연구를 이어나갈 수 있었다고 생각합니다.

또한 본 논문이 완성되기까지 많은 지도와 격려를 해주시고 논문의 심사위원장을 맡아주신 윤석훈 교수님께 진심으로 감사드립니다. 아울러 바쁘신 와중에도 세심하게 논문을 심사해 주시고 논문의 완성도를 높이기 위해 아낌없는 조언을 해주신 박상균 교수님, 정석호 교수님, 천강우 박사님께도 마음속 깊은 감사의 말씀을 드립니다.

저에게 학문의 기회를 열어 주시고 지속적인 연구의 길을 안내해주신 조권희 교수님께 진심으로 존경과 감사의 마음을 올립니다. 저의 사소한 학문적 호기심에도 열과 성의를 다해 고민해주시고 가르침을 주신 점 잊지 않고 내리사랑으로 보답하겠습니다.

대학입학 시절부터 저에게 바른 길을 인도해주시고 언제나 따뜻한 격려를 해주시는 정병건 교수님, 먼 곳에 계시면서도 제 연구를 끊임없이 지원을 해주시

고 삶의 지혜도 나눠주시는 박설현 교수님, 물심양면 지원을 아끼지 않으시고 앞으로의 연구에 대해서도 함께 고민해주시는 강준 교수님께도 깊은 감사의 말씀을 드립니다.

배움에 대한 노력하는 자세와 자긍심을 일깨워 주신 한원희 교수님, 연구 활동에 있어 여러모로 도움을 주시고 따뜻한 격려를 아끼지 않으신 김종수 교수님, 이영찬 교수님, 최정식 교수님께도 깊은 감사를 드립니다.

박사과정을 시작하는 시기에 실습선에서 늘 격려와 배려를 아끼지 않으신 선 박운항과 배병덕 교수님, 이상일 교수님, 정은석 교수님, 이진욱 교수님, 이윤석 교수님, 김종성 교수님, 이상득 교수님, 정진아 교수님, 오세진 교수님, 조익순 교수님, 윤귀호 교수님, 전해동 교수님께도 깊은 감사를 드립니다. 본 연구의 실험에 큰 도움을 주시고 함께 일하며 많은 배려를 해주신 정균식 선배님, 박준모 선생님, 이상우 선생님을 비롯한 한국해양대학교 실습선 사관님들과 모든 승조원분들께도 깊은 감사를 드립니다. 또한 논문 자료수집에 도움을 주시고 함께 고민해주신 강무경 연구원님, 김종립 연구원님, 천정민 연구원님께도 감사의 말씀을 드립니다.

그리고 박사과정의 마무리를 잘 할 수 있도록 좋은 여건을 만들어주시고 많은 배려를 해주신 연수원 원장님 이하 모든 교수님들과 실습선 동료 교원분들께도 진심으로 감사를 드립니다.

논문과 실험을 위해 많은 조언과 지원을 해주시고 즐거운 연구실 생활을 하게 도와준 이경우 대표님, 한상구 팀장님, 장세현 대표님, 신우중 후배님을 비롯한 모든 연구실 분들에게도 감사의 마음을 전합니다.

더불어 학업을 이어가는데 있어 든든한 동반자이자 지원군인 이지웅 교수님을 비롯한 EG55 동기들과 제가 힘들고 지칠 때마다 큰 버팀목이 되어주는 나의 오랜 벗들에게도 심심한 감사를 드립니다.

언제나 아낌없는 사랑을 베풀어주시고 제 마음속 든든한 버팀목이 되어주시는 아버지·어머니, 저를 믿어주시고 묵묵히 응원해주시는 장인·장모님 늘 감사드립니다. 더 많이 성장하는 모습으로 그 은혜에 보답하겠습니다. 부디 건강

하십시오.

그리고 힘든 육아 중에도 남편을 위해 항상 응원해주는 고맙고 사랑하는 나의 아내 가영, 애교 넘치는 사랑스러운 우리 딸 서안, 눈에 넣어도 안 아플 것 같은 귀요미 아들 서준과 함께 이 기쁨을 나누고 싶습니다.

마지막으로 한정된 지면을 통해서 일일이 언급을 하지 못했지만 그동안 저를 응원해주시고 사랑해주신 모든 분들께 다시 한 번 진심으로 감사드립니다. 모두 건강하시고 가정과 직장에 행복만이 가득하시길 기원합니다.

2016년 12월 이원주 드림.

